

https://dspace.org/

Thermo-mechanical behaviour of rocks from the Busveld Igneous Complex with relevance to deeper mining

Oniyide, Gafar

2016
http://hdl.handle.net/10539/20030

Downloaded from a DSpace repository. https://dspace.org/

CHAPTER FOUR

4.0 MICROSCOPIC ANALYSES OF ROCK SAMPLES

This chapter presents the microscopic image analyses of rock specimens from the Bushveld Igneous Complex after being subjected to heat treatment. The aim of the microscopic analyses is to examine the effect of heat on rock texture and composition, in terms of initiation or extension of micro-cracks and changes in their chemical composition. In the mining context, it was attempted to understand the effect of temperature drop on the surfaces of underground openings due to ventilation by the help of microscopic analysis. The growth of planar cracks, which are perpendicular to the grain boundary, have been reported to be formed during the cooling of igneous rocks. These cracks were attributed to mismatch of physical properties across grain boundaries during cooling (Richter and Simmons, 1974; Fonseka *et al*, 1985). The micro-cracks contained in rocks affect their behaviour (compressive and tensile), sonic velocity and thermal conductivity. The results of the temperature tests reported in chapter three will be correlated with the findings from microscopic study.

4.1 Microscopes used for image capturing

Image capturing was achieved by means of two types of microscopes, namely:

- Optical Microscope (OM): The OM used is Olympus BX61, (Figure 4.1). The advantage of the OM is that the colour of the minerals that make up the rock texture can be seen since the surface coating of specimens is not required. The OM uses visible light and a system of lenses to magnify images of small size samples. Using the Olympus BX61, the images were captured in both bright field (sample contrast comes from absorbance of light in the sample) and dark

field illumination (sample contrast comes from light scattered by the sample) (Tsukahara *et al*, 2014).

- Scanning Electron Microscope (SEM): The SEM used is FEI Nova 600 Nanolab, (Figure 4.2). The SEM has edge over the OM because of its higher resolution, however, the specimens were gold-palladium coated to allow for good quality image. The SEM produces image by scanning with a focused beam of electrons. The interaction of the electrons from the beam and the atoms in the samples produces signals that contain information about the surface topography and composition (Dunlap and Adaskaveg, 1997). The changes in the elemental composition of the rock samples were also determined using Energy-dispersive X-ray Spectrometry (EDS) equipment known as INCA, attached to the SEM. Progressive scanning of parallel lines of the specimen through electron beam forms the image.



Figure 4.1: Olympus BX 61 optical microscope.



Figure 4.2: FEI Nova 600 Nanolab scanning electron microscope.

4.2 Specimen preparation

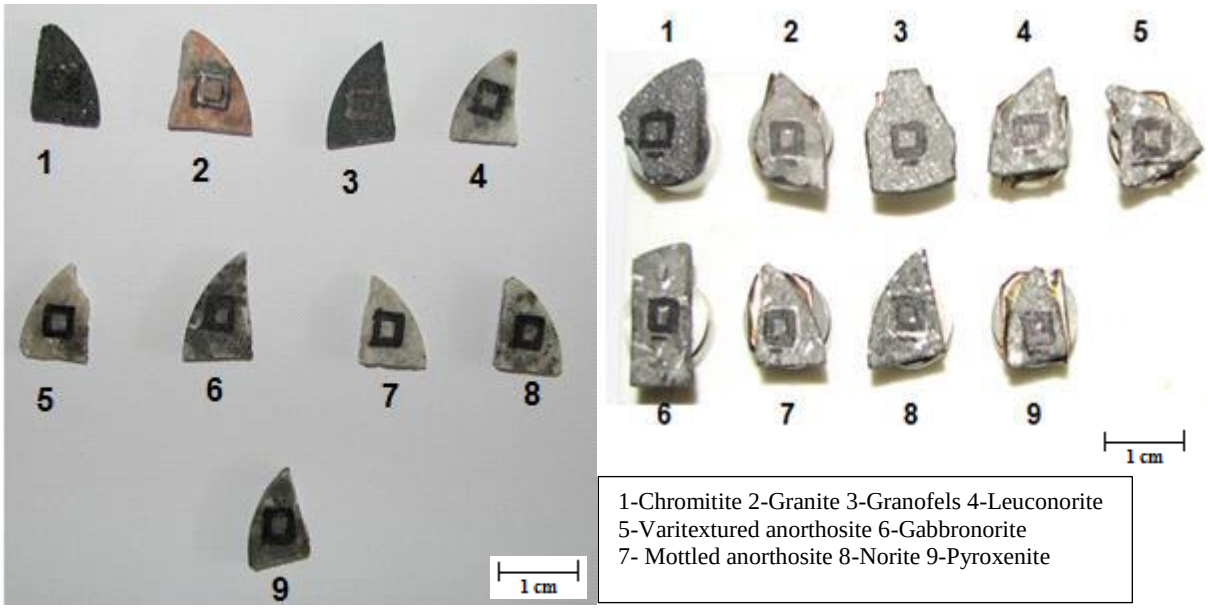
The specimens for microscopic analysis were prepared from the rock cores obtained from mines in the western and northern BIC. The rocks used were chromitite (UG2), pyroxenite, norite, leuconorite, gabbronorite, mottled anorthosite, varitextured anorthosite, granite and granofels.

The first step in specimen preparation is cutting, grinding and polishing. This is followed by sputter coating. Dunlap and Adaskaveg (1997) defined sputter coating as the method of applying a thin layer of conductive metals (such as gold, gold/palladium, platinum, silver) on a sample using a sputter coater. In SEM, electrically non-conducting specimens, such as rock, can absorb electrons, which cause accumulation of negative charge. The accumulated charge repels electron beam

and results in degrading of the image. Sputter coating reduces sample charging and microscope beam damage (Mukhapadhyay, 2003).

Grinding and polishing of the surfaces to be examined were done with the aid of a lapping machine and then the rock specimens were cut to a thickness of 2.5 mm. The surfaces of SEM specimens were coated with a thin layer of Au/Pd alloy. The layer deposited is typically 10 to 20 nano meters thick.

Figures 4.3 (a) and (b) show the samples prepared for OM and SEM image capturing respectively. The thick square marks on the surface of the OM and SEM samples show the area to be analysed under the microscopes. The dash (-) below the square marks in the SEM samples (Figure 4.3 (b)) is for easy identification of the base of the specimen in terms of orientation. Without this mark, it is difficult to pick the same spot that have been previously captured.



(a) (b)

Figure 4.3: (a) OM and (b) SEM samples for image capturing.

4.3 Heat treatment of specimens

The thermal treatment of the rock specimens were done in heat-regulated oven. The specimens were heated up to 50ºC, 100ºC and 140ºC at the rate of 2ºC/minute and the temperatures were kept constant for five consecutive days. These temperatures are the approximate virgin rock temperatures of the BIC mines at 1073 m, 3276 m and 5038 m below surface respectively. Samples were then allowed to cool to ambient temperature before image capturing. Micrographs of specimens were taken before and after heat treatment. For SEM analyses, a single specimen from each rock type is subjected the specified temperature range, while different specimens were heat-treated for OM analyses. All the SEM samples were also subjected to heating and cooling cycle on alternative days for ten days in order to observe the effect of repeated heating and cooling on the rock structure. The samples were re-coated with gold/Palladium alloy after repeated heating and cooling.

4.4 Results of optical image capturing

The aim of the optical image capturing is to examine whether heat treatment of the rocks will have significant effect on the physical outlook of the sample surfaces, by looking at the changes in the colour of the rock minerals. The sample images were captured using OM under bright field illumination. Although the samples were also captured under dark field illumination, the dark field images were excluded in the report due to the insignificant differences in the images of dark and bright fields. Figures 4.4 to 4.6 show the microscopic images of chromitite before and after heat treatment up to 140ºC, while the images of the other samples are presented in Appendix A7.

Voordouw (2009) reported the average modal mineral abundance in volumetric percentage of plagioclase feldspar, orthopyroxene, chromite and other minerals (such as phlogopite, biotite, ilmenite, rutile, magnetite, quartz, serpentine and talc) for UG1

and UG2 seams (Table 4.1). Schouwstra *et al* (2000) also stated that UG2 consists predominantly of chromite (60 to 90% vol.), with lesser silicate minerals (5 to 30% pyroxene and 1 to 10% plagioclase) while other minerals are present in minor concentrations.

The colour of plagioclase ranges from white, colorless, cream, gray, yellow, orange and pink, chromite is mostly black while pyroxene ranges from dark green to black. Plagioclase is silicates of sodium, calcium and aluminium, pyroxene is silicate of magnesium and iron, while chromite is oxide of chromium, iron and magnesium (Schouwstra *et al*, 2000).

Table 4.1: Average modal mineral abundance of UG1 and UG2 seam (Voordouw *et al*, 2009)

lithology	**pl (Vol.%)**	**px (Vol.%)**	**chr (Vol.%)**	**Other minerals (Vol.%)**	**Total (Vol.%)**
UG1 chromitite	31	15	53	1	100
UG2 chromitite	10	8	62	19	99

The major chromitite minerals are indicated in Figures 4.4 to 4.6 in red colour. Figures 4.4 (a) and (b) show the micrographs of chromitite before being subjected to heat treatment up to 50ºC and when cooled to ambient temperature after heat treatment. The physical changes observed (red circles) are in the chromite-rich areas. In Figure 4.4 (b), heat treatment exposed yellow-looking minerals (plagioclase, rutile or serpentine) and whitish minerals (quartz, talc or plagioclase) - the upper two circles. The lower circle shows disappearance of whitish mineral, which may be talc or plagioclase that flaked off from its original position due to heating and cooling of the specimen.

Figure 4.5 shows that the heat treatment does not cause any significant physical change in the specimen. It is observed that some spots of white mineral surfaced after the specimen was heat treated to 100ºC (red circles in Figure 4.5 (b)). A major difference is observed in Figure 4.6 (b) after the specimen was heated to 140ºC and cooled. Some of the dark minerals, such as chromite and pyroxene, were displaced by quartz or plagioclase. In general, the heating and cooling of rocks is seen to cause changes in the physical characteristics of the minerals.

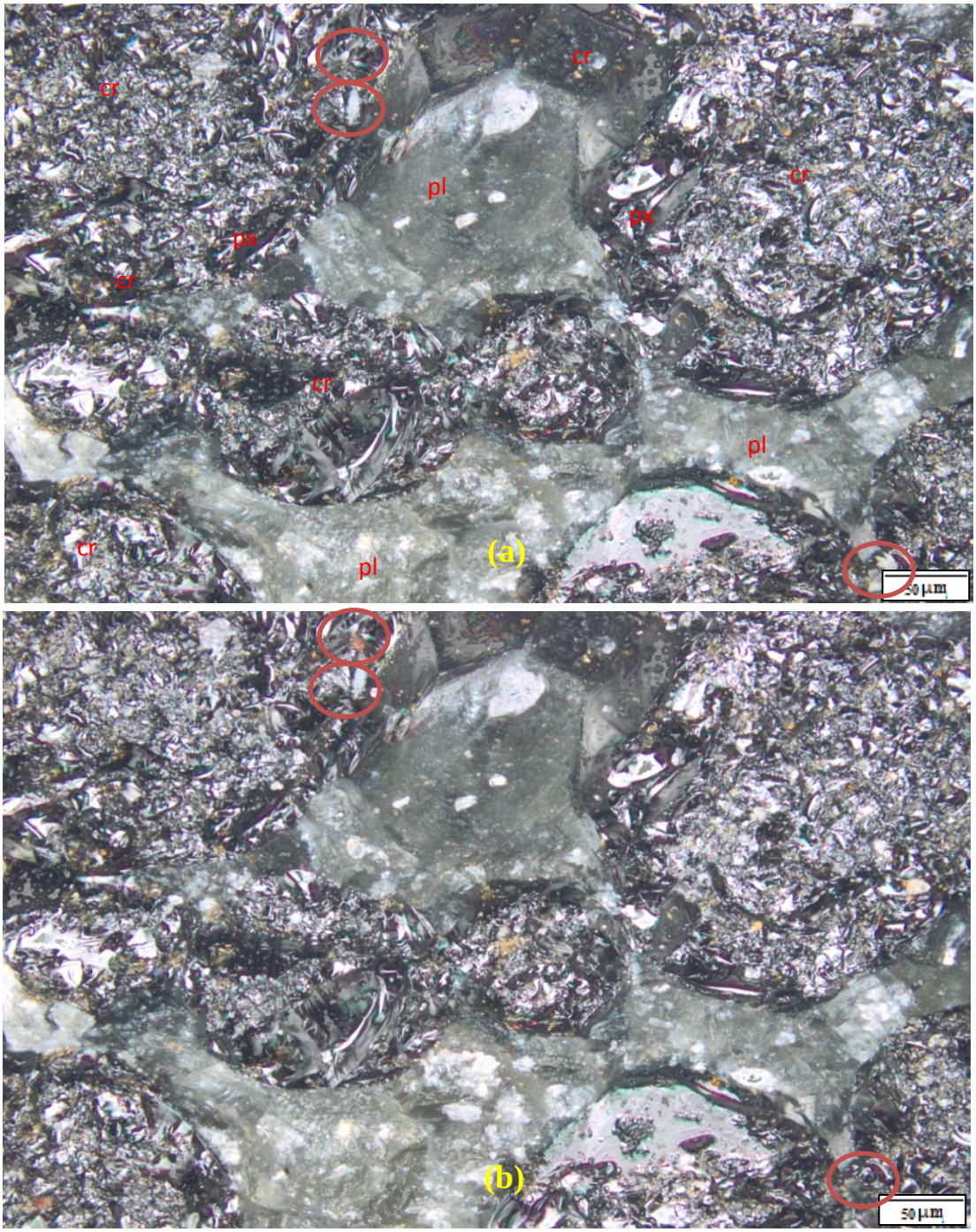


Figure 4.4: Micrograph of CR (a) before and (b) after heat treatment to 50ºC

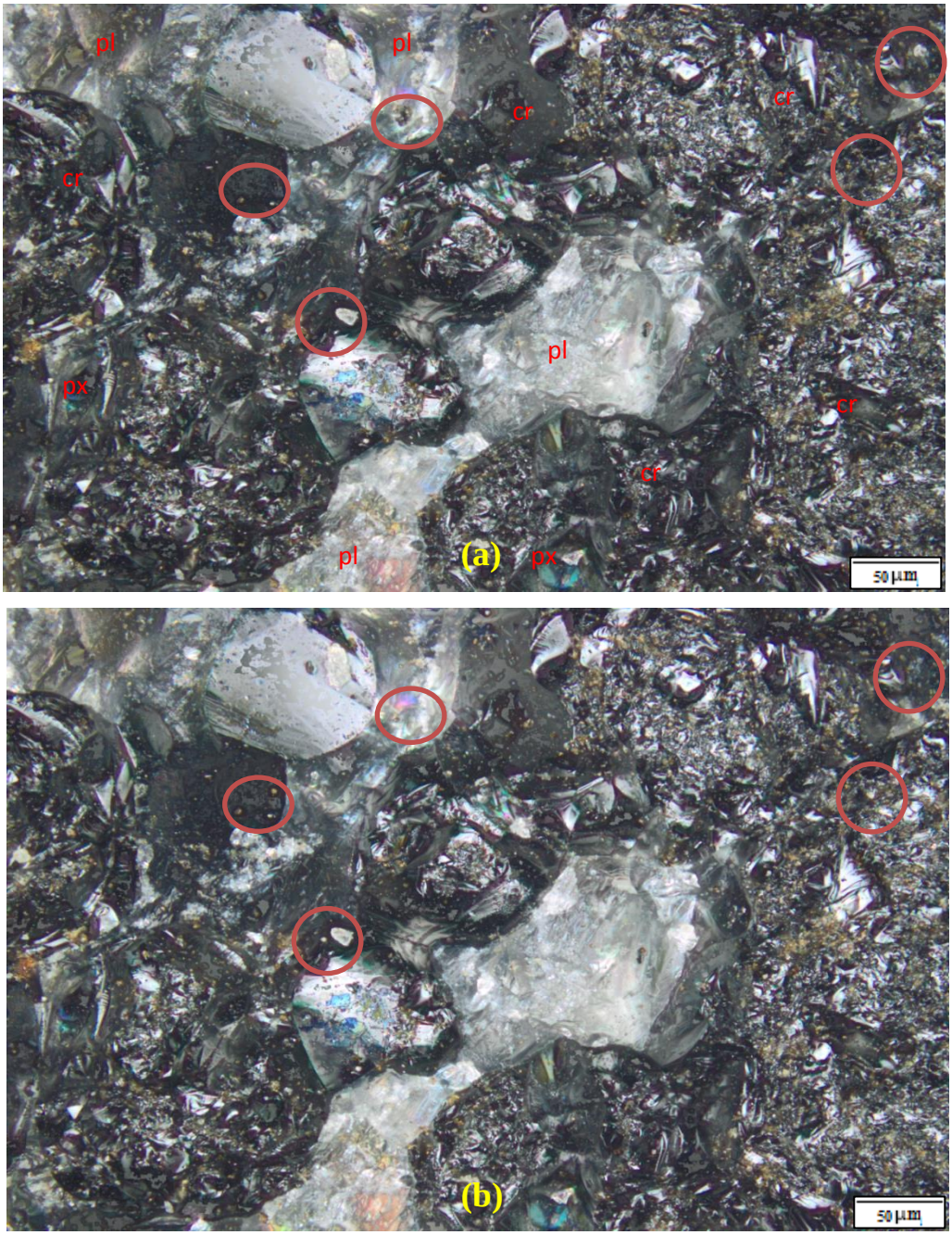


Figure 4.5: Micrograph of CR (a) before and (b) after heat treatment to 100ºC

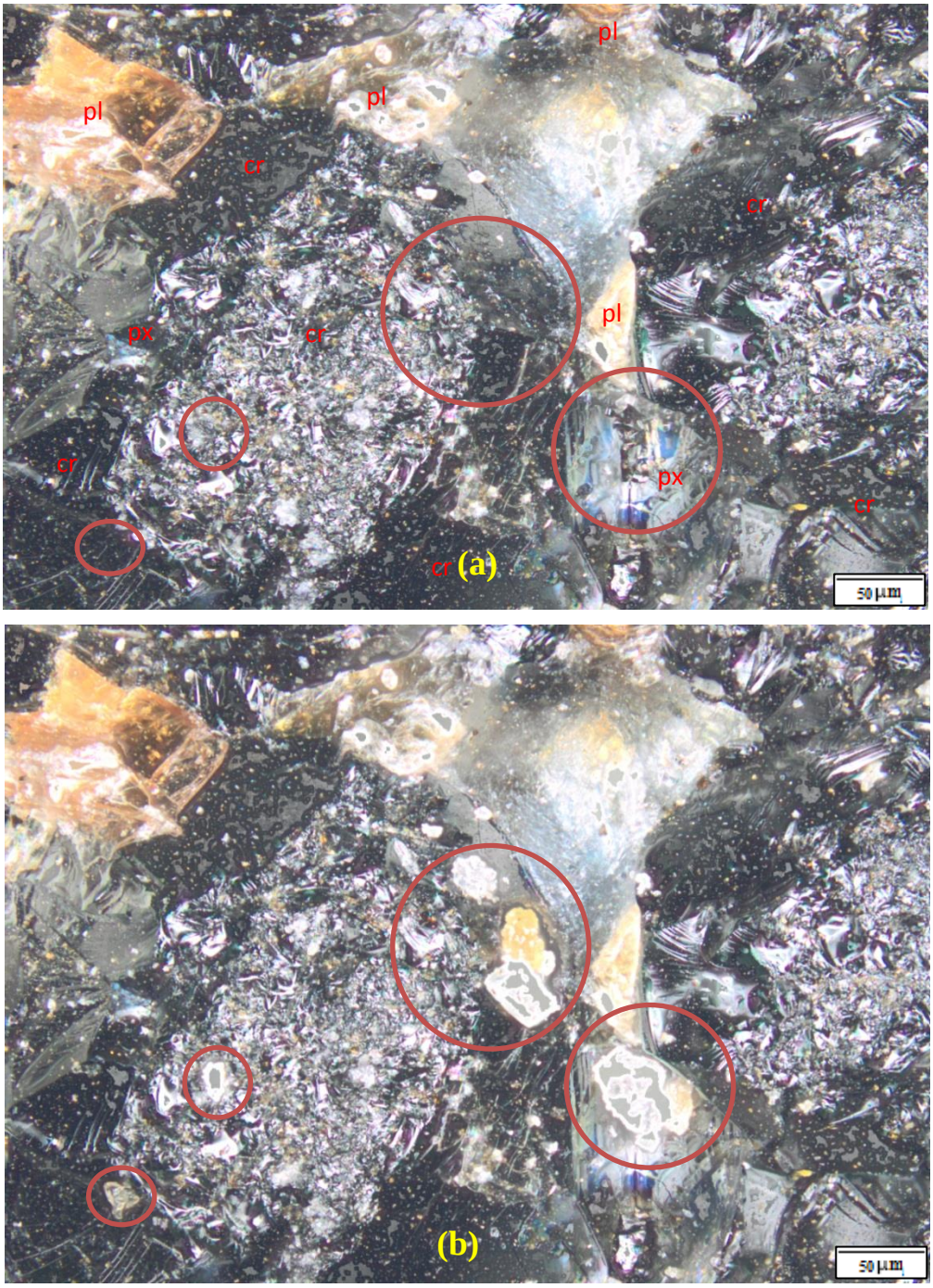


Figure 4.6: Micrograph of CR (a) before and (b) after heat treatment to 140ºC

4.5 Results of the scanning electron microscope (SEM) analysis

The SEM was used to examine the reaction of rock samples to heat treatment in terms of crack extension/widening. Figures 4.7 to 4.9 show the microscopic images of chromitite before and after they were subjected to heat treatment, while the images of the other samples are presented in Appendix A7.

Figures 4.7 (a) and (b) are the micrographs of chromitite before and after heat treatment to 50ºC and cooled to ambient temperature. Figure 4.7 (a) shows that the specimen has a few micro-cracks prior to heat treatment. After heat treatment (Figures 4.7 (b)), the existing cracks were seen to extend and widen. Some of the invisible cracks became visible close to the edge of the specimen. When subjected to further heating to 100ºC (Figures 4.8 (a)), more crack extensions and widening were noticed especially close to the boundaries of the square-marks. The middle of the specimen remains intact. This suggests that temperature range used is not high enough to induce cracks within the specimen except at the boundaries.

When the heat treatment was done at 140ºC, (Figures 4.8 (b)), crack widening was more than extension. This was a result of coalescence of the cracks as a result of tensile failure of specimens due to expansion. Some weakly bonded fragments of the specimen were detaching as low as 50ºC and the detachment continued with further increase in temperatures. When the specimen was subjected to repeated heating and cooling (Figures 4.9), there was further crack widening and detachment of fragments from the specimen.

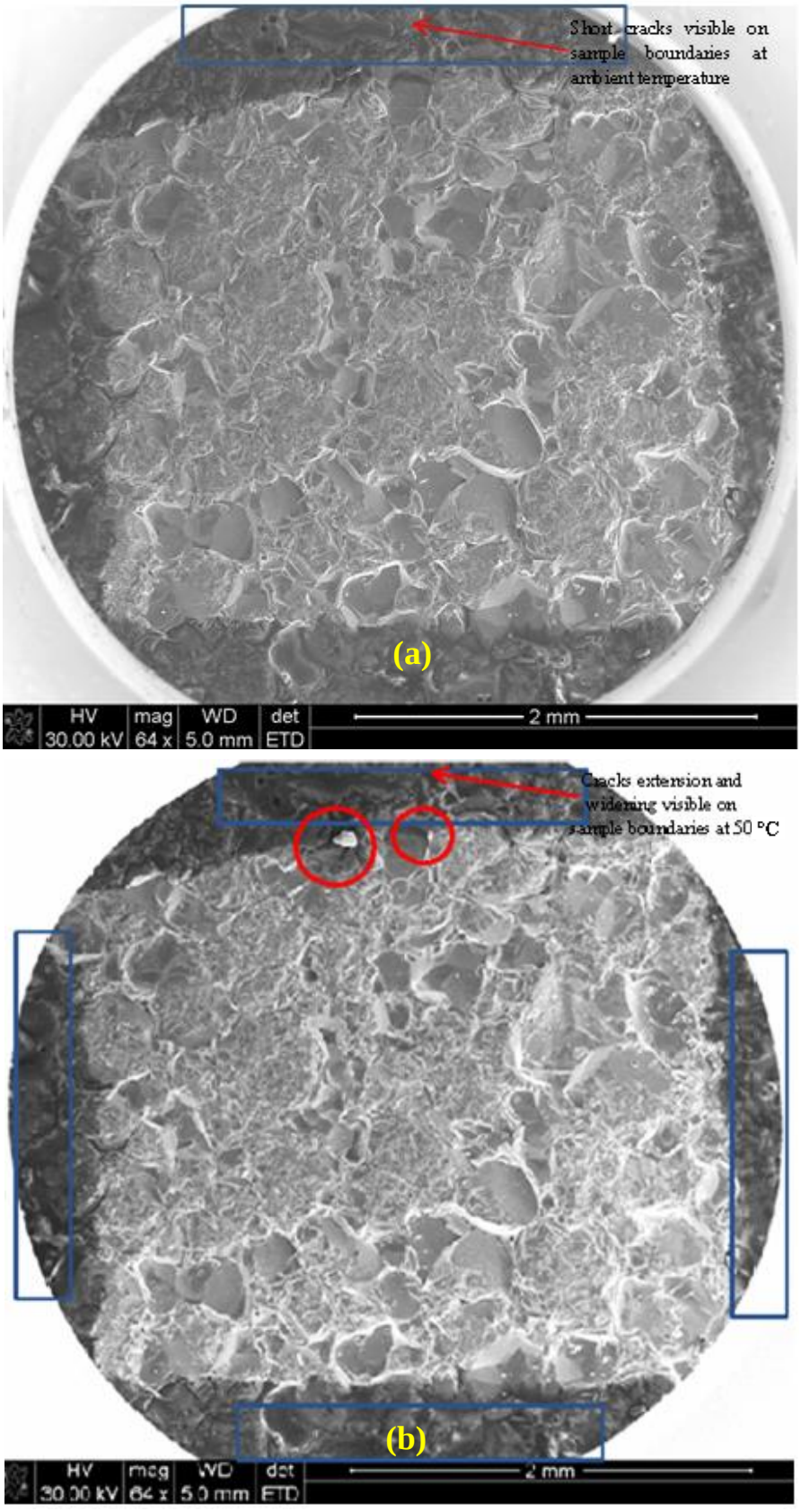


Figure 4.7: Chromitite (a) before and (b) after heat treatment to 50ºC

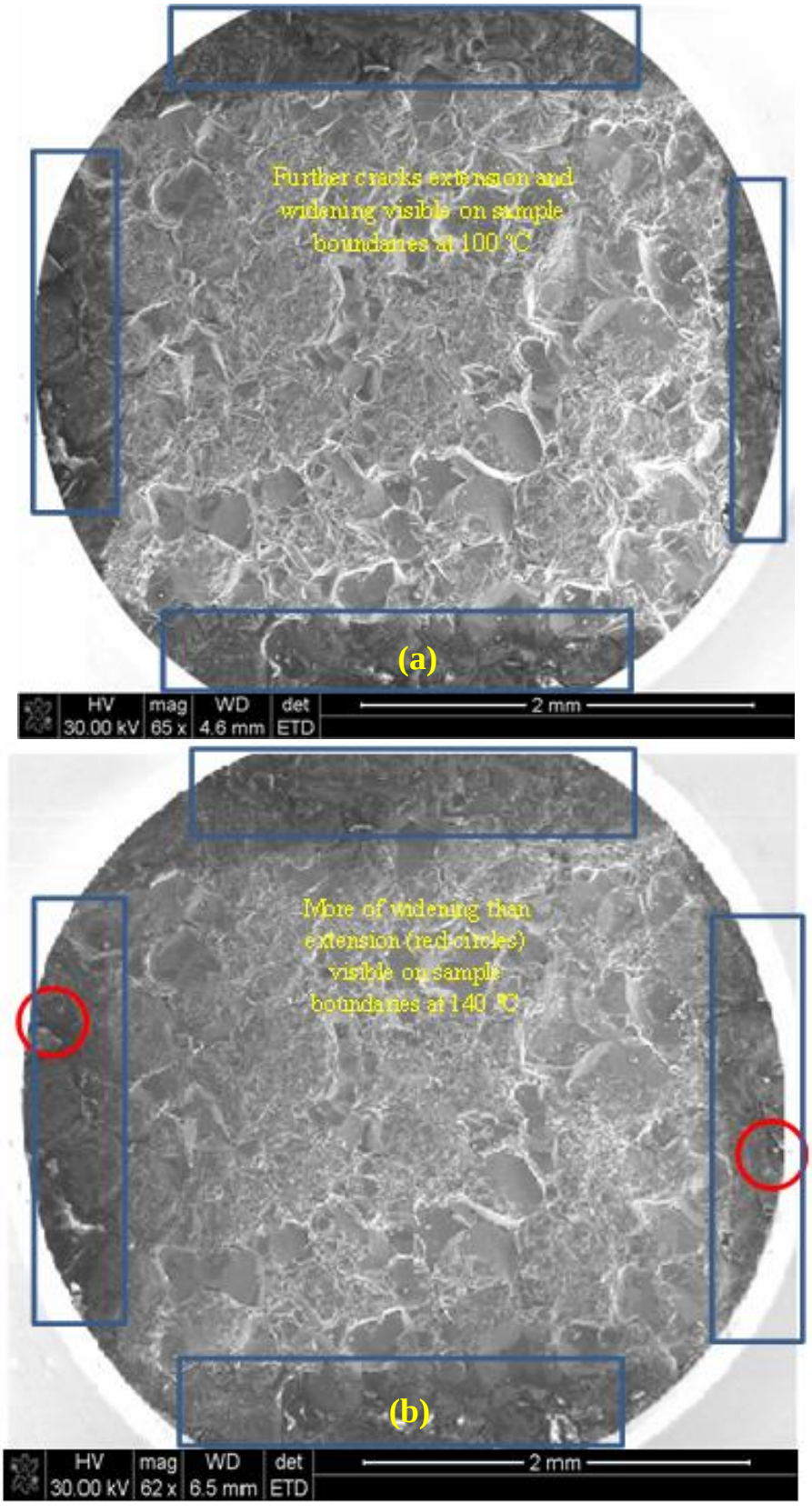


Figure 4.8: Chromitite after heat treatment to (a) 100ºC (b) 140ºC

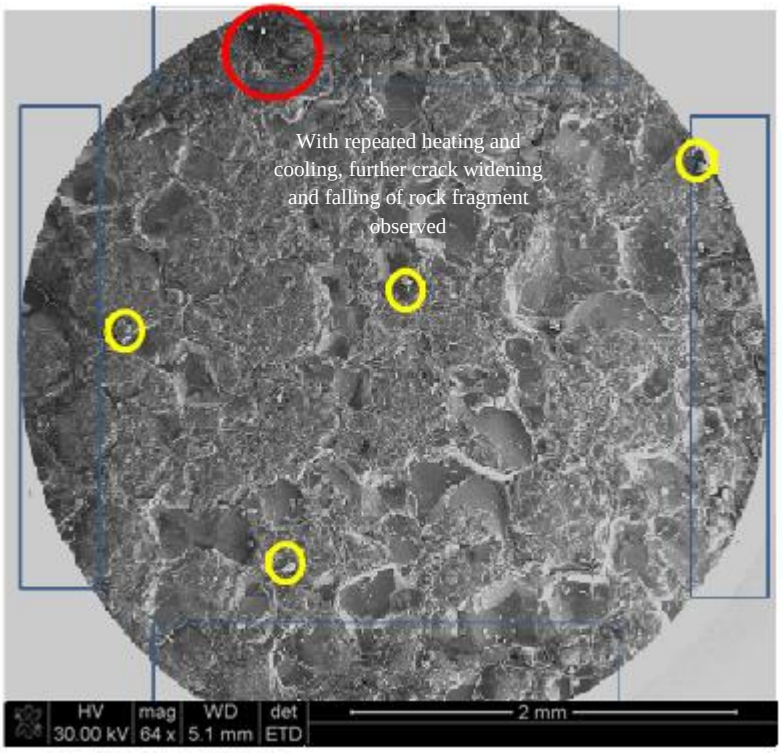


Figure 4.9: Chromitite after heat treatment to 140ºC with repeated heating and cooling.

Table 4.2 shows the maximum visible micro-crack length that develops between 50ºC and 140ºC on all the specimens using SEM micro-measurement technique. This technique involves enlargement of SEM micrograph followed by physical measurement, then conversion to the original size using the micrograph scales.

Table 4.2: Maximum visible crack lengths of specimens

Specimen	CR	MA	LN	N	GN	GF	VTA	G	PX
Max. crack length (mm)	0.65	0.14	0.05	0.00	0.00	0.00	0.10	0.27	0.36

Table 4.2 shows that no visible cracks were observed in norite, gabbronorite and granofel. The table also shows that of all the samples heat-treated, chromitite was the

mostly affected one by heat followed by pyroxenite, while the effects observed in leuconorite and varitextured anorthosite were insignificant. In the case of granite, few micro-cracks were observed when heated from ambient temperature to 140ºC. However, when subjected to repeated heating and cooling, a clearly visible macro-crack extended from the lower to the upper end of the sample as shown in Figures 4.10 and 4.11. This observation shows that granite is sensitive to heating and cooling cycles. It is noteworthy that when specimens were made to pass through heating and cooling cycles, the sputtered gold/palladium alloy faded and caused image distortion (white patches in Figure 4.11(b)). However, when the granite specimen was re-coated, the visibility of the macro-crack was reduced Figure 4.11(a)).

The laboratory experiments reported in chapter three on the measurement of CLTE and ultrasonic velocity revealed that when rock specimens are heated, thermal stress caused breaking of the bond between rock minerals. The bond breakage results in generation, propagation and coalescence of cracks. The microscopic study detailed here contributes to the understanding of what happens pictorially, when rock is heated and cooled. The microscopic analysis shows that not all the cracks generated during the heating stage are "healed" upon cooling. The analysis also shows that repeated heating and cooling, even at lower temperatures could lead to the development of macro-fractures, as it is the case with thermal weathering of rocks. The implication is that, when ventilation cools the excavation surfaces, the inner part of the rock (far field) remains hot and continuously radiates heat towards the exposed surface, while the surface is continuously cooled by ventilation. Such heating-cooling cycles could contribute to degradation of rock quality.

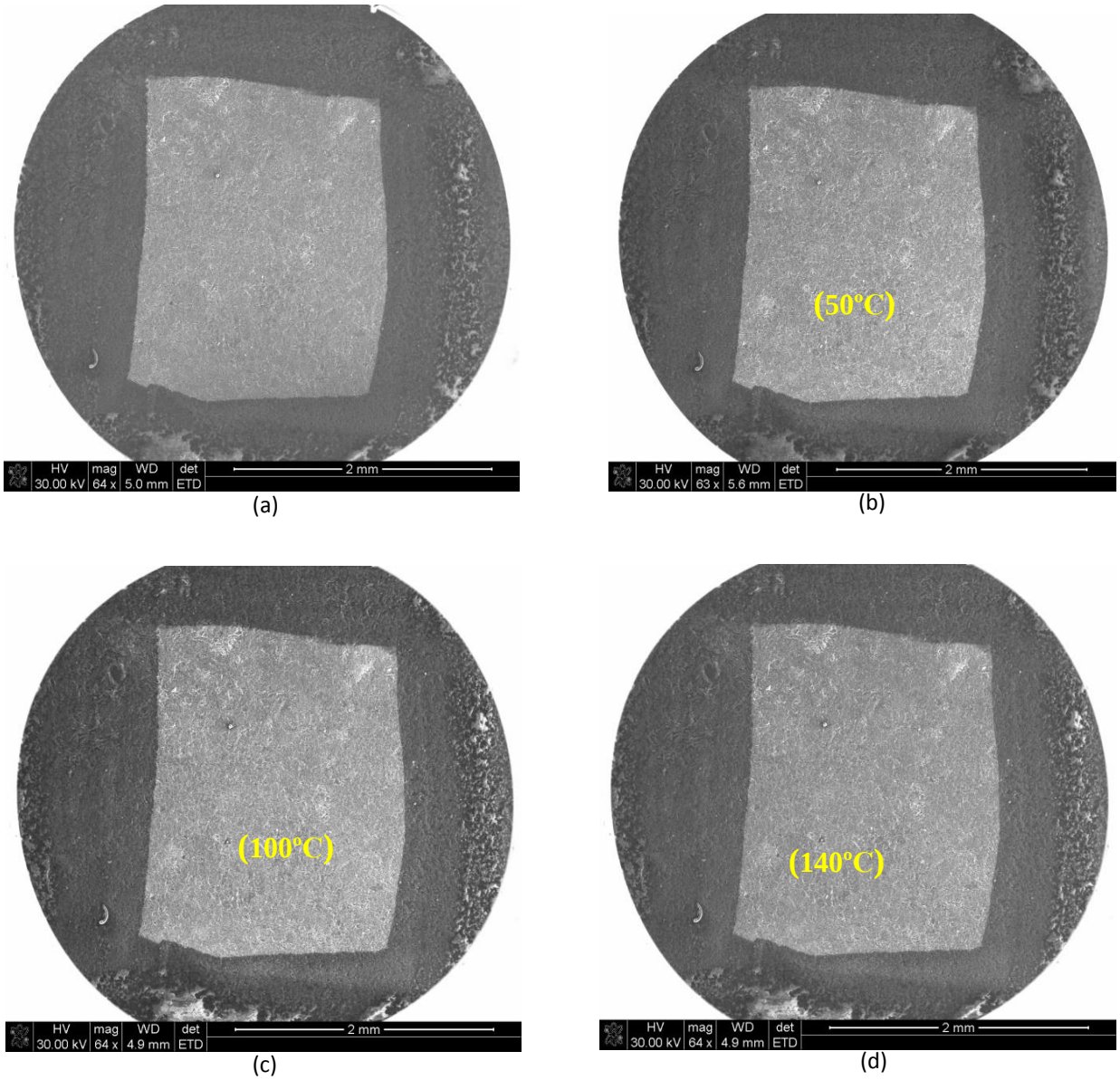


Figure 4.10: Granite (a) before heating, after heating (b) 50°C (c) 100°C (d) 140°C

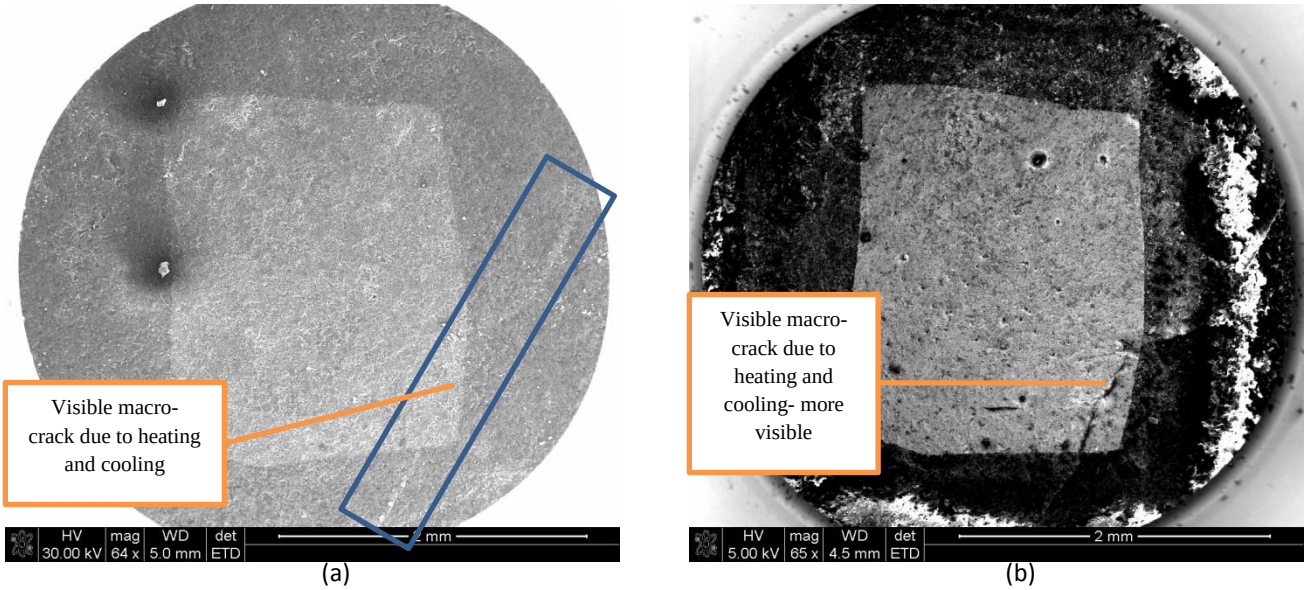
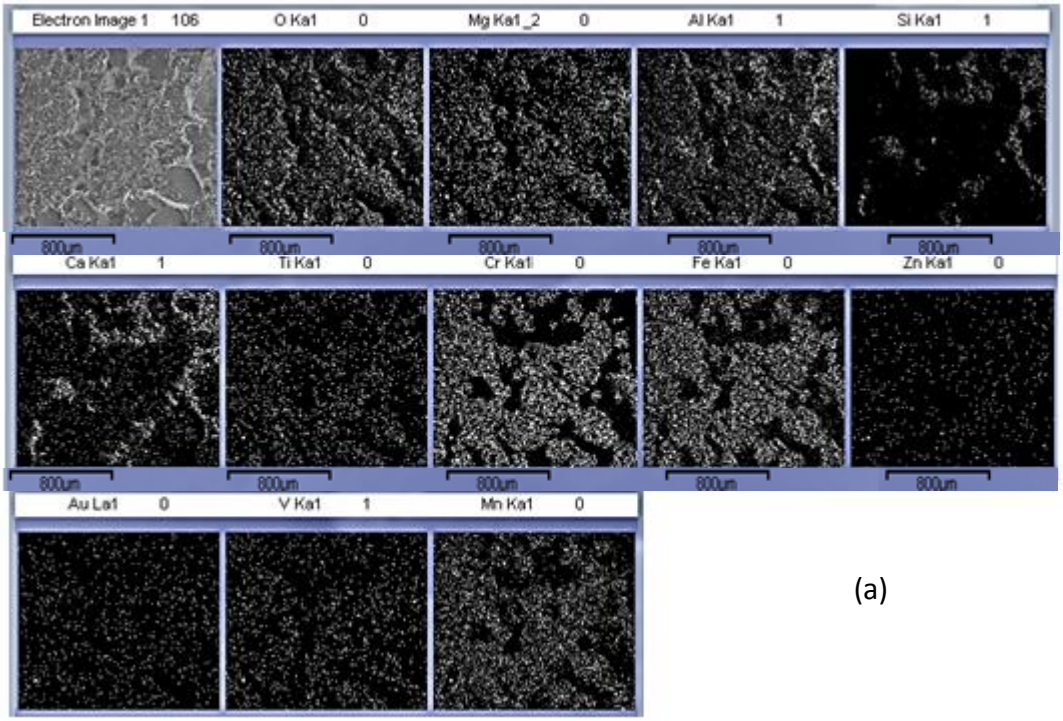


Figure 4.11: Granite subjected to repeated heating and cooling (a) after sputter coating, (b) before sputter coating

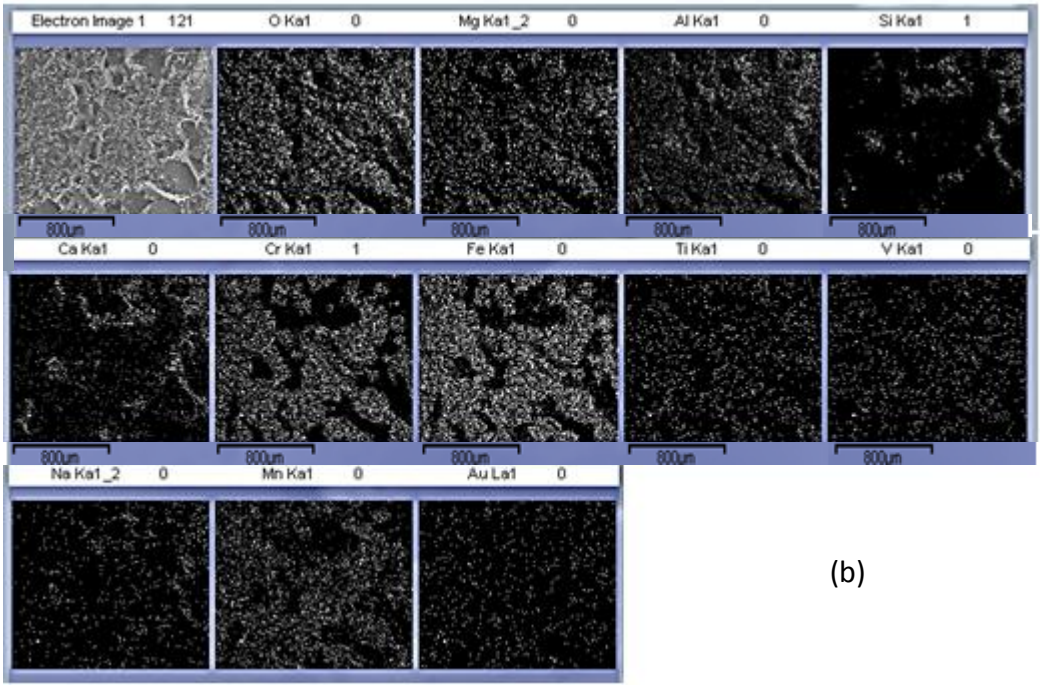
4.6 Result of Energy-dispersive X-ray Spectrometry

The elemental composition of samples were determined for each temperature range. The results of the chemical characterisation, which reveals the chemical composition and composition variation of the elements in chromitite, are presented in Figures 4.12 and 4.13 in the form of element maps. Element map is an image showing the spatial distribution of elements in a sample. In Figures 4.12 and 4.13, the letter or letters before “K” or “L” stands for the element symbol. For example, in Figure 4.12 (a), O, Mg Al, Si, Ca, Ti, Cr, Fe, Zn, Au, V, Mn represent Oxygen, Magnesium, Aluminium, Silicon, Calcium, Titanium, Chromium, Iron, Zinc, Gold, Vanadium, and Manganese respectively. “K” and “L” stand for the first and second electron shells respectively, while “a” representa alpha x-ray. The amount of white portion in the maps is an indication of the dominance of elements in the group and the maps that look similar means that there is strong bond between the elements.

It should be noted that in Table 4.2 and Figure 4.14, oxygen has the highest value of elemental composition. The reason is that it reacts with almost all the other elements to form silicates and oxides. A careful look at the all the elemental maps in Figures 4.12 and 4.13 shows that there is not much difference in the mineral compositions of the specimen when heat treated from ambient temperature up to 140ºC. This is also confirmed in Table 4.3. However, temperature caused some elements to be displaced while others resurface. For example, the element maps and Table 4.3 reveal that zinc appears only in ambient condition. A sudden increase in the values of gold and palladium in the column for repeated heating and cooling results from sputter coating.



(a)



(b)

Figure 4.12: Element map of chromitite (a) before and (b) after heat treatment to 50ºC

Table 4.3: Summary of elemental composition (% weight) of CR for all temperatures

	Ambient	**50ºC**	**100ºC**	**140ºC**	**Repeated heating & cooling**
Mg	4.47	4.50	4.46	4.62	4.20
Al	10.70	10.86	10.59	10.76	10.22
Si	6.27	6.45	6.54	6.11	6.48
Ca	1.72	1.73	1.77	1.64	1.80
Ti	0.39	0.37	0.40	0.41	0.36
V	0.25	0.24	0.23	0.24	0.25
Cr	23.02	22.24	22.32	22.79	21.36
Fe	14.16	13.71	13.84	14.10	13.27
Au	2.66	2.53	2.49	2.55	4.60
O	35.89	36.04	35.99	35.88	35.19
Na	0.00	0.90	0.96	0.90	0.90
Mn	0.41	0.44	0.41	0.00	0.39
Zn	0.05	0.00	0.00	0.00	0.00
Pd	0.00	0.00	0.00	0.00	0.98

4.7 Chapter summary

The results of the optical microscope analyses show that there are physical changes observed on the rocks subjected to heat treatment however, the observed changes are not significant in a way to affect the behaviour of rocks. The scanning electron microscope images revealed that crack initiation starts at lower temperature and extends with increasing temperature. This is an indication that temperature would influence the texture of rocks in underground mines with high geothermal gradient. The chemical analyses of the samples subjected to different temperatures show that the temperature range considered for this research is not high enough to induce noteworthy chemical changes in the samples.

CHAPTER FIVE

5.0 NUMERICAL MODELLING

Some of the in-situ stress measurement data received from the mines are compared with those published in the literature. The in-situ stress data used in numerical modelling were derived from these two data sources. Numerical modelling input parameters, such as, the UCS, E, υ, bulk and shear moduli, cohesion, friction angle, dilation angle, coefficient of thermal expansion, were derived from the laboratory tests reported in chapter three.

This chapter examines the influence of temperature on the behaviour of rocks through numerical modelling. The analyses of the numerical modelling results are aimed at understanding the behaviour of rock in deep and hot underground excavations and on the laboratory rock specimens.

The confining pressure and temperature are varied for the laboratory modelling in order to study the influence of temperature on the behaviour of intact rock, as well as, the effect of confinement on the temperature-induced tensile in a failed specimen. In the case of underground excavation modelling, the virgin rock temperature and in-situ stresses become higher with increasing depth of mining. Continuous ventilation cools the excavation surfaces, while heat is also continuously radiated to the surface from the inner rock, thereby causing temperature variation close to the skin of the excavation. The numerical modelling, therefore, looked into the influence of the variation of both in-situ stresses and various temperatures on the response of underground excavations.

Since there are many factors that could influence the stability of underground structures, the numerical modelling provides an opportunity of keeping some of these factors fixed in order to have an understanding of the effect of varying temperature. The numerical code used for the analyses is FLAC (Fast Langrangian Analysis of Continua) 2D (Itasca Consulting Group, 2012). The FLAC thermal conduction model was coupled to the mechanical model for thermo-mechanical analyses (The model

detail is given in Appendix A8). The conduction model allows simulation of transient heat conduction in materials and the development of thermally induced displacement and stresses.

5.1 Model input parameters

The required input parameters for the thermo-mechanical modelling of laboratory size rocks and underground excavation and their sources are summarized in Table 5.1.

Table 5.1: Model input parameters and their sources

Model Input Parameters	Source
Virgin rock temperature (VRT)	Corporate Office of Anglo Platinum Limited
Rock stress (confining conditions)	Mines and published articles
Rock properties (mechanical and thermal)	Laboratory testing (Chapter three)

5.1.1 Virgin rock temperature (VRT)

VRT data (Figure 5.1) for the BIC was sourced from the Corporate Office of Anglo American Platinum Limited, Mine Ventilation and Refrigeration Engineering Unit (Erasmus, 2012). Figure 5.1 shows that Der Brochen mine has the lowest temperature gradient, while BRPM has the highest.

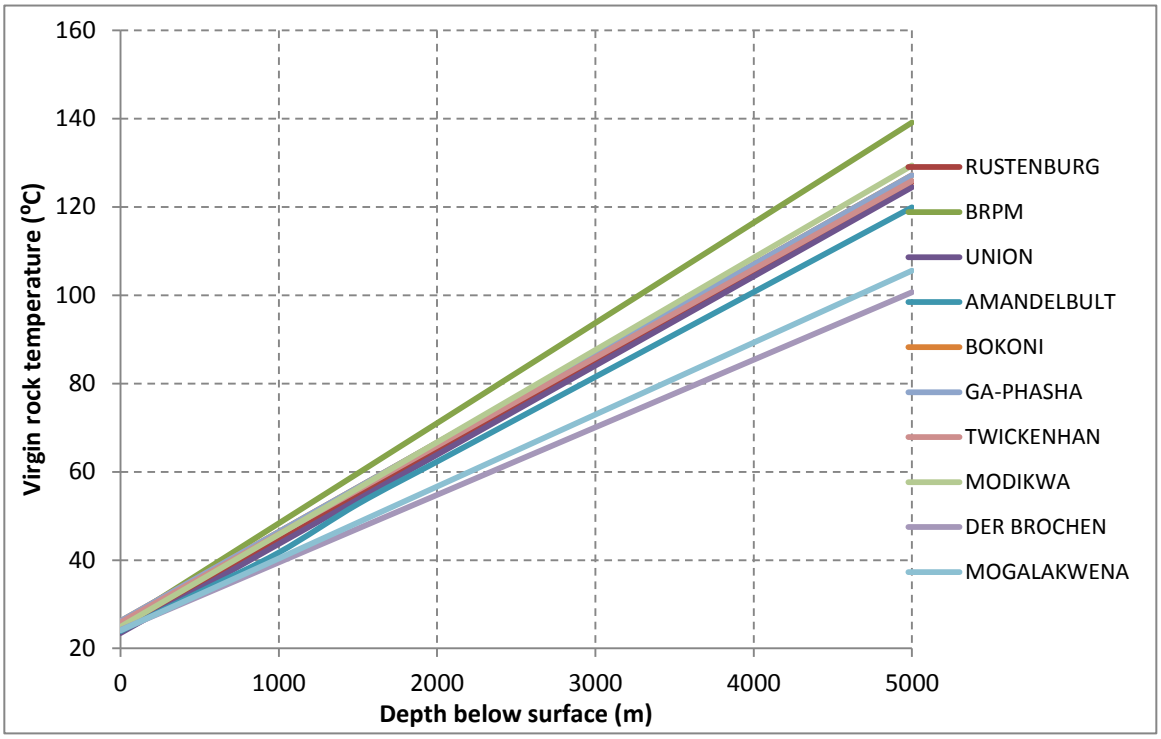


Figure 5.1: Graph of virgin rock temperature against depth for platinum mines (Erasmus, 2012)

Simpson (2011) advised that it is essential that engineering designers carefully consider the worst situation and parameter values that could be imagined based on a reasonable and well- informed engineering assessment. Therefore, in this modelling, the VRT of BRPM is used since it has the highest thermal gradient so that the influence of temperature would also be the highest.

Using the information in Figure 5.2, the VRT equation for BRPM is given as:

$$y = 0.0227x + 25.64 \quad (5.1)$$

$$and\ x = (y - 25.64)/0.0227 \quad (5.2)$$

Where y is the VRT, and

x is the depth below surface, in meters.

Table 5.2 shows the equivalent depths for the temperatures (50°C, 70°C, 90°C, 110°C and 140°C) on which the laboratory testing was based. The temperature-depth relationship (equation 5.1) was used in the numerical modelling. For instance, VRT of 50°C was assigned to the modelled excavation at depth of 1073 m.

Table 5.2: Temperatures and equivalent depths for BRPM

Temperature (°C)	Depth (m)
50	1073
70	1954
90	2835
110	3716
140	5037

5.2 FLAC 2D modelling of laboratory intact rock in triaxial testing

The input parameters required for numerical modelling of the triaxial laboratory testing are divided into mechanical and thermal types.

1. Mechanical parameters are:
   - ❖ density,
   - ❖ cohesion,
   - ❖ friction angle,
   - ❖ bulk and shear modulus,
   - ❖ dilation.
2. Thermal parameters are:
   - ❖ coefficient of linear thermal expansion (α),
   - ❖ thermal conductivity (λ) and
   - ❖ heat capacity (c).

5.2.1 Intact rock properties

The summary of the properties of intact rock samples tested in the laboratory under different confinement and thermal conditions is given in Tables 5.3 to 5.6. These parameters were determined in chapter three. Varitextured anorthosite and anorthosite

chromitite are not included in the tables because they are not considered in the numerical modelling.

Table 5.3: Average tensile strength and density of specimens

	MA	CR	N	PX	LN
Tensile Strength (MPa)	9.46	4.91	11.21	11.42	9.45
Density (kg/m^3)	2744	4049	3045	3194	2776

Table 5.4: Summary of friction angle (φ) and cohesion (c)

	MA		CR		N		PX		LN	
Temperature (°C)	φ	c	φ	c	φ	c	φ	c	φ	c
Ambient	56.0	30.1	51.5	13.6	49.5	31.0	47.5	32.7	50.8	31.0
50	55.8	29.7	50.7	13.4	49.7	30.2	46.6	32.5	49.7	30.9
90	55.6	28.7	50.2	13.3	48.9	30.1	46.3	32.0	49.6	30.0
140	55.5	28.0	49.6	13.2	48.7	30.0	44.1	31.7	48.1	29.8

Table 5.5: Post-peak and residual dilation angles for the rocks tested

	MA	CR	N	PX	LN
Temperature (°C)	**Post-peak (°)**				
Ambient	51.5	38.8	45.1	47.2	46.5
50	53.0	40.1	51.5	50.5	48.7
90	55.0	47.6	53.7	54.0	52.2
140	58.8	53.3	55.7	57.6	54.9
	Residual (°)				
Ambient	14.7	8.61	11.99	12.59	13.52
50	16.2	10.96	13.39	13.57	13.93
90	19.1	13.53	16.10	16.87	15.10
140	23.2	15.94	18.98	20.58	19.45

Table 5.6: Heat capacities, thermal conductivity and coefficient of thermal linear expansion of the rocks

	MA	CR	N	PX	LN
Temperature (°C)	**Heat capacities of the rocks (J/kg/K)**				
50	810	740	840	860	840
90	850	780	880	900	880
140	890	820	920	940	920
Thermal conductivity of the rocks (W/(m.K))					
50	2.0	2.4	2.3	3.7	2.2
90	1.9	2.3	2.2	3.6	2.1
140	1.8	2.2	2.1	3.5	2.0
The coefficient of thermal linear expansion					
x 10^{-6} m/m/°C					
50	6.8	6.5	6.6	6.8	6.5
90	7.6	7.5	7.6	7.5	7.6
140	8.8	8.5	8.4	8.8	8.7

5.2.2 FLAC 2D model set-up

A finite difference grid is generated for the numerical model (Figure 5.2). The material is composed of 36 zones in the x-direction and 95 zones in the y-direction to provide the specimen dimensions and length to diameter ratio used in the laboratory. After the grid generation, the model is configured in thermal and isotropic option and material properties were then assigned, that is, density, bulk and shear modulus, cohesion, friction angle and dilation.

Roller boundary conditions were applied to the top and bottom boundaries of the model and the model is fixed along y-direction. The right and left boundaries of the model were left free because of the applied confining stress of 10 MPa. A compressive velocity of 2.5 x 10^{-6} m/s was initialized at j=1 and 96, while the confining stress was applied as sxx, syy and szz at i=1 and 37.

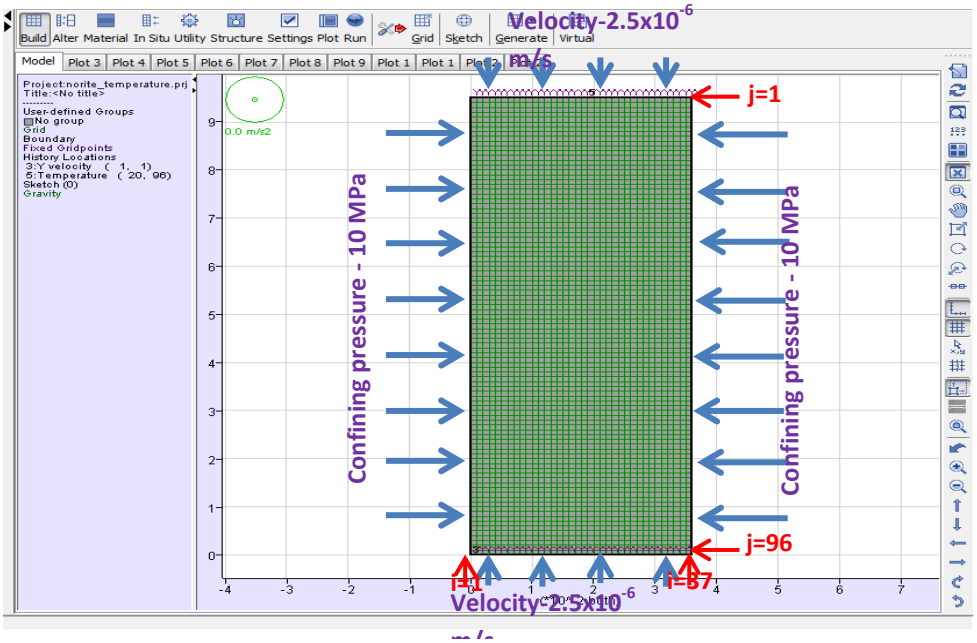


Figure 5.2: Model set up for the triaxial simulation.

A servo-control function was used to minimize the influence of inertia effects on the response of the model. The FISH file "SERVO.FIS" (appendix A9) was used to adjust the applied vertical velocities as a function of the unbalanced force. The FISH function was built into the data file to calculate the average vertical stress, *sigmav*, and average vertical strain, *ev*, in order to generate the stress-strain plots.

The numerical experiment was carried out on specimens at ambient temperature, 50ºC, 90ºC and 140ºC, in order to simulate the laboratory experiment. Rock testing in numerical modelling extended beyond the results obtained in the laboratory. The ambient condition was modelled on mechanical cycling and thermal cycle was set off. In problem solving with FLAC, static mechanical option is selected for conventional tests, which does not involve consideration of thermal, dynamic and fluid interactions (Itasca Consulting Group, 2012). For samples modelled at 50ºC, 90ºC and 140ºC, the thermal properties were included and thermal-mechanical cycling was used in order study the thermal effects.

Röchter et al. (2011) defined shear band (Figure 5.3) as thin zones of localised deformation with a discontinuity of the strain field at its boundaries. Charalampidou et al. (2011) also described shear band as a zone of cracked and shear grains, a few grains wide, in which the predominant displacement of grain pieces is parallel to the band's long axis.

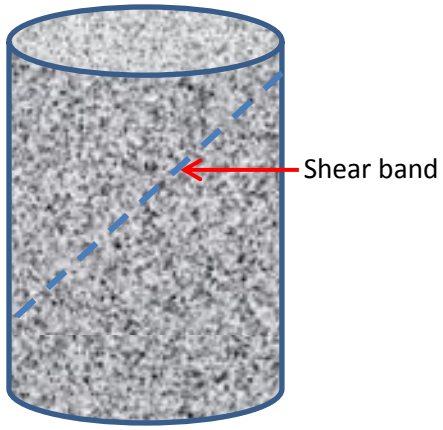


Figure 5.3: Illustration of shear band on a failed triaxial test specimen.

Figures 5.4 to 5.11 show the results of FLAC and laboratory tests for norite with specimen superimposed for comparison of the shear bands. In the FLAC plots, the units of stress and strain are MPa and mm/mm respectively, as it is the case with the laboratory results presented in this chapter.

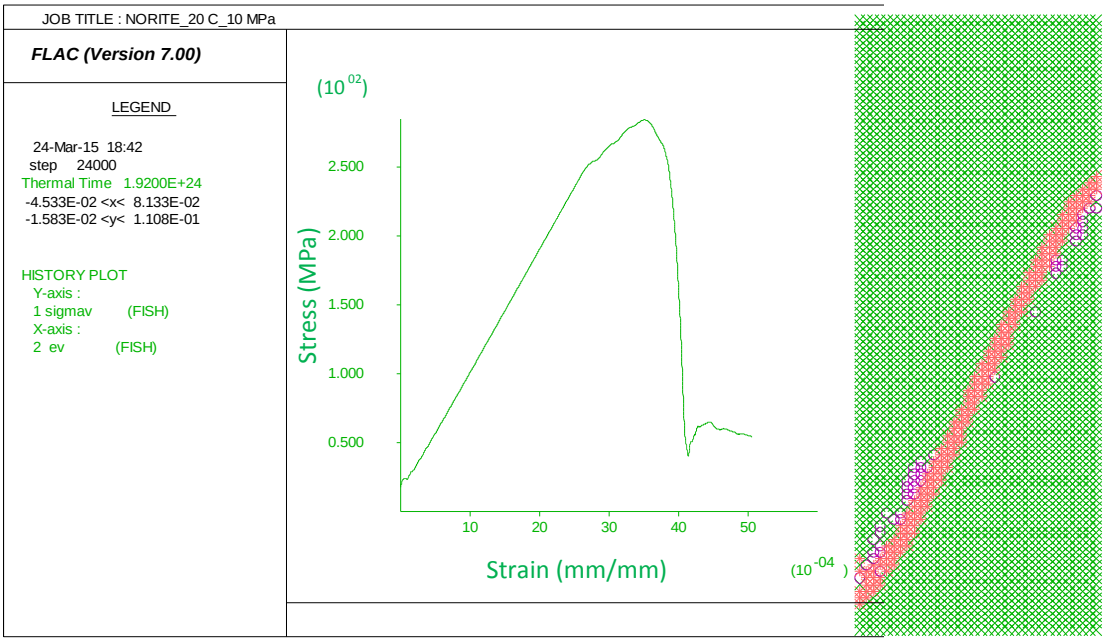


Figure 5.4: FLAC plot of norite tested at 20ºC and confining pressure of 10 MPa

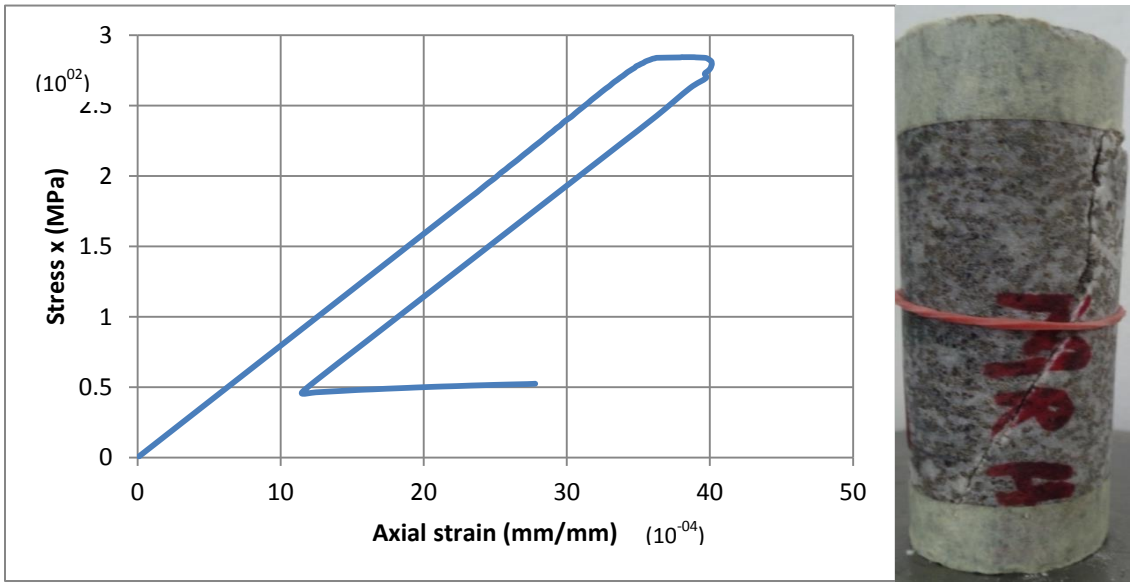


Figure 5.5: Laboratory plot of norite tested at 20°C and confining pressure of 10 MPa

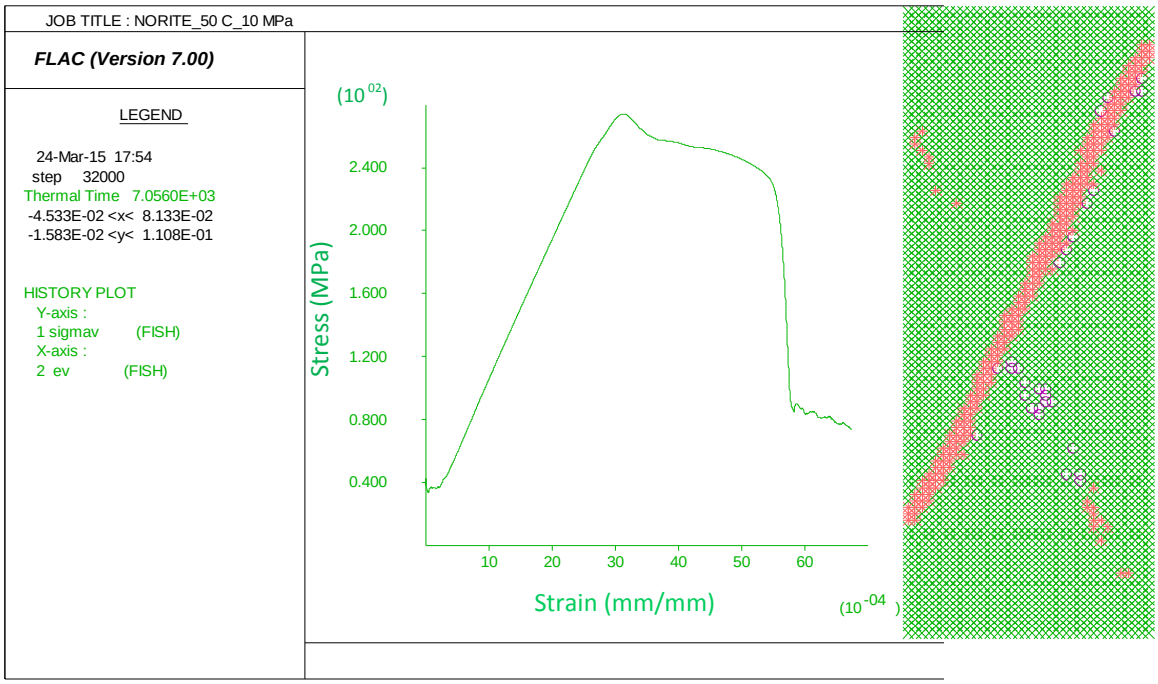


Figure 5.6: FLAC plot of norite tested at 50°C and confining pressure of 10 MPa

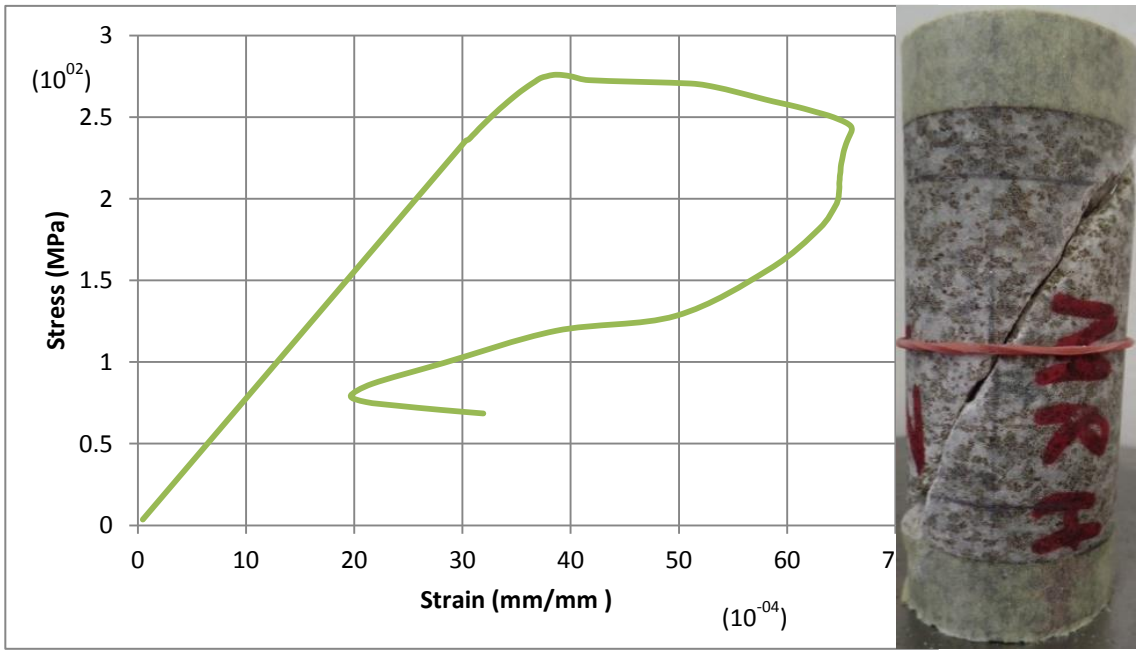


Figure 5.7: Laboratory plot of norite tested at 50°C and confining pressure of 10 MPa

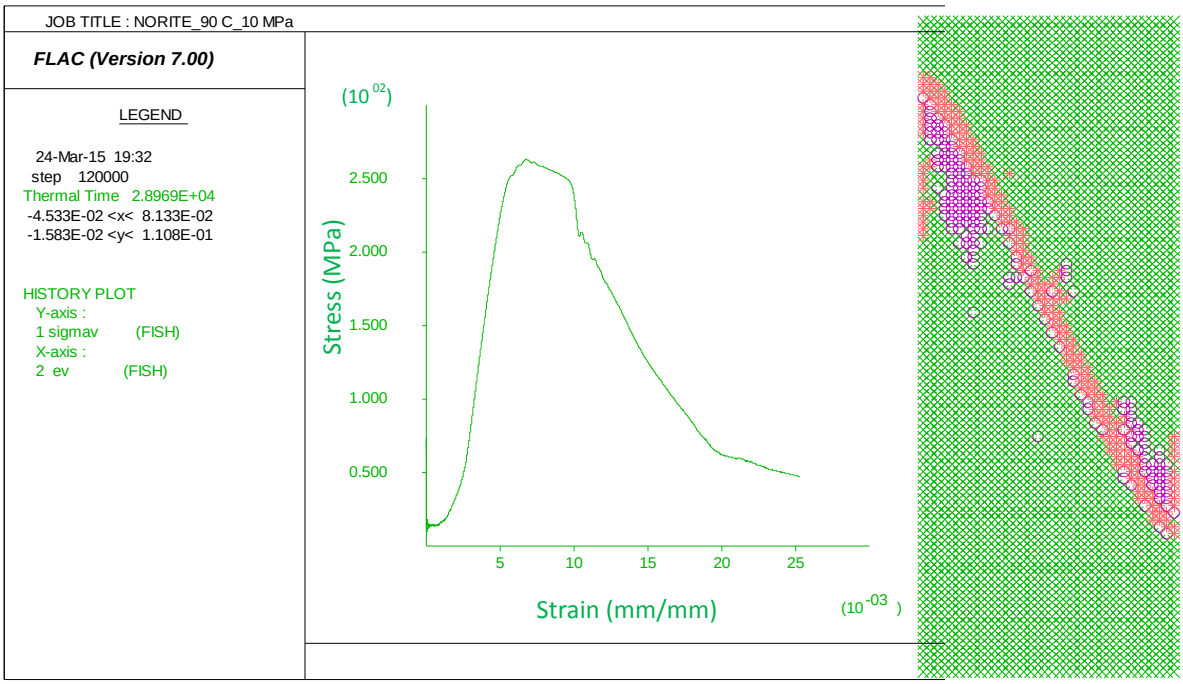


Figure 5.8: FLAC plot of norite tested at 90°C and confining pressure of 10 MPa

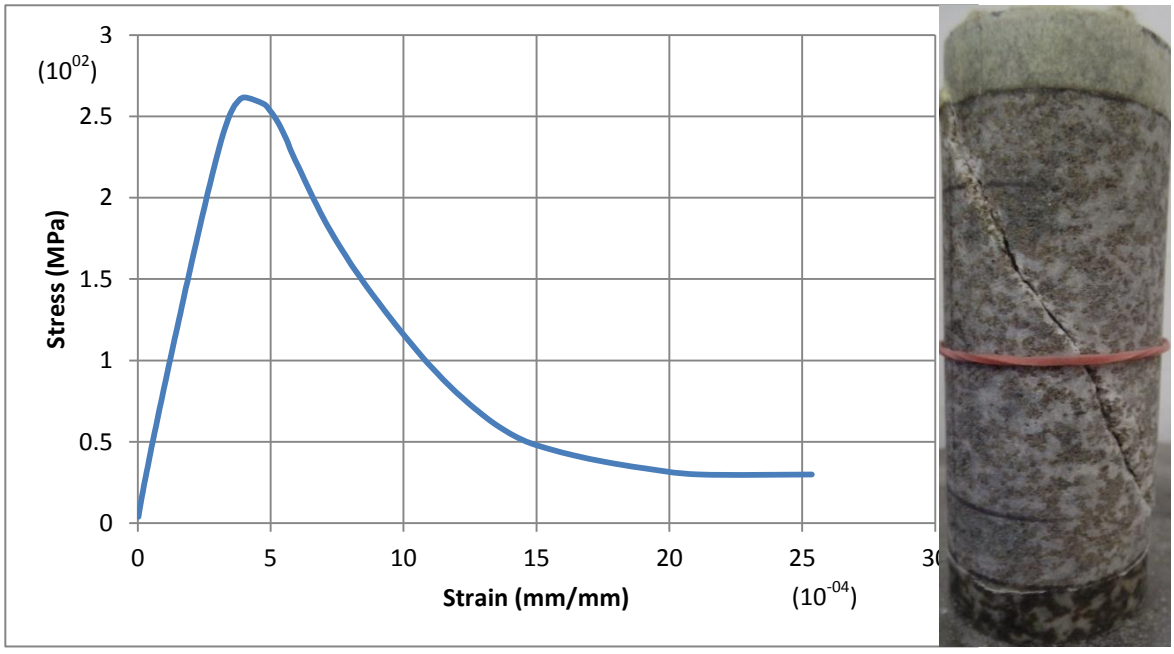


Figure 5.9: Laboratory plot of norite tested at 90°C and confining pressure of 10 MPa

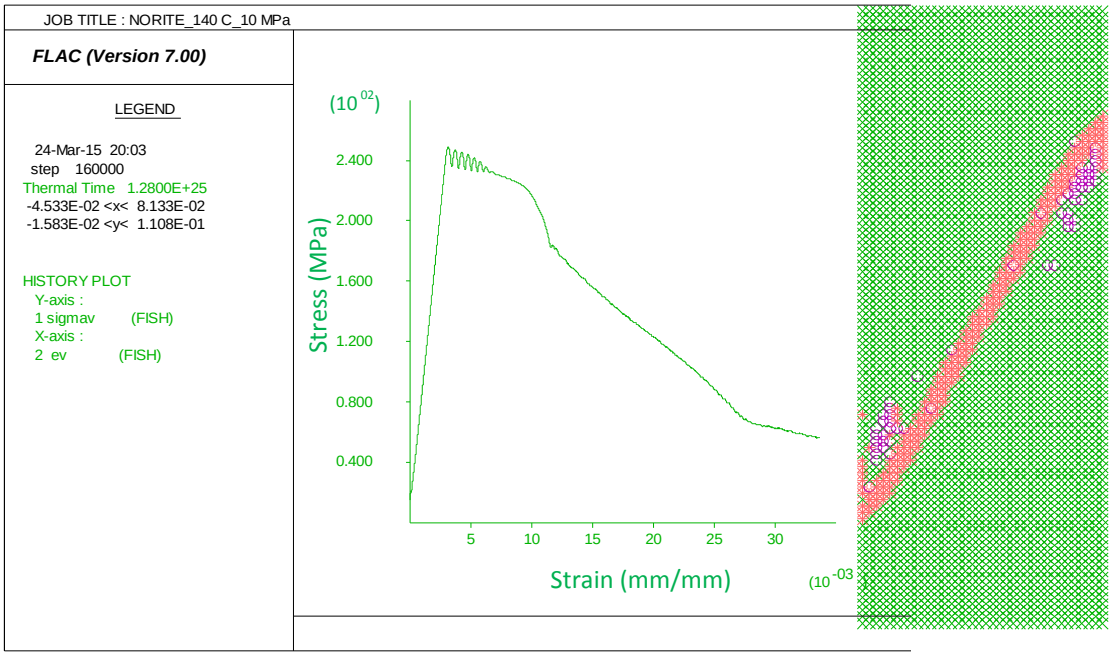


Figure 5.10: FLAC plot of norite tested at 140°C and confining pressure of 10 MPa

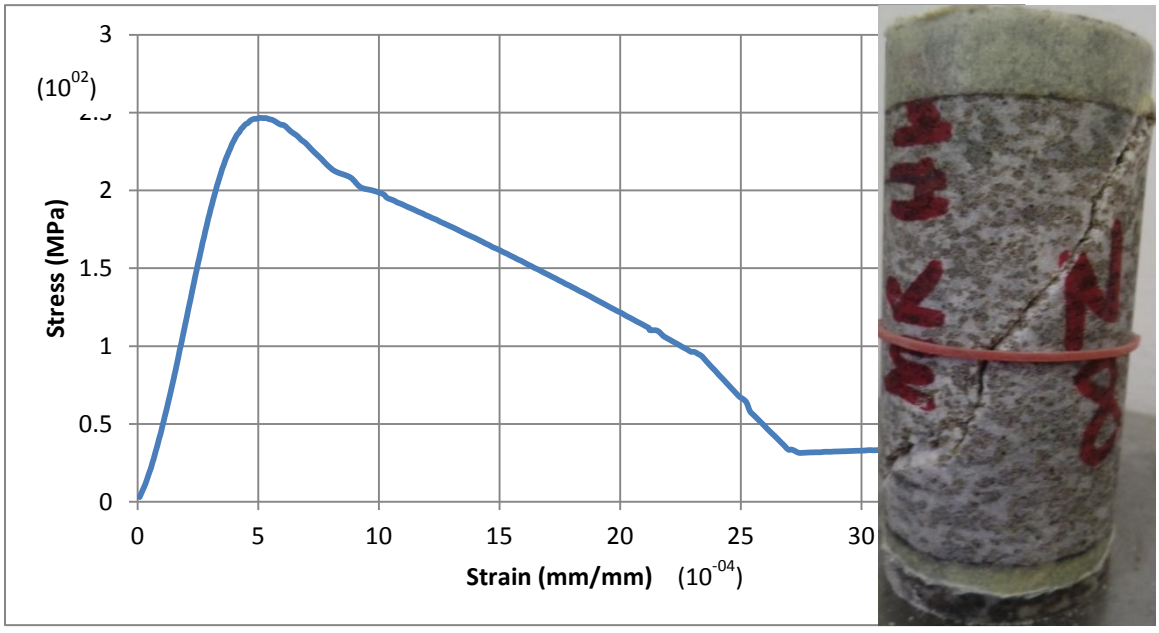


Figure 5.11: Laboratory plot of norite tested at 140°C and confining pressure of 10 MPa

As observed in the FLAC plots, the stress starts from about 20 MPa to 40 MPa while the axial strain is zero. This is due to the use of servo-control function in the model. Similar observation is seen in the example given by Itasca Consulting Group, (2012), while demonstrating the use of the servo-control function. The stresses become higher at zero strain when the thermal-mechanical coupling is used.

From Figures 5.4 to 5.11, it is observed that the numerical modelling results are similar to the laboratory results, in terms of the peak strength and the nature of shear band of the samples. The only difference is in the post-peak part of the FLAC stress-strain plots for rocks that show class II type behaviour in actual laboratory testing. Instead of positive modulus in the post-peak region, the stress-strain behaviour results in the negative modulus in FLAC modelling. The modelling of class II behaviour is difficult to achieve with FLAC code due to the servo-controlled FISH function that uses axial strain-control to obtain the post-peak curve. Efforts to use radial strain or Young's modulus in FLAC modelling as control mode, the method of control in the actual laboratory experiment, were unsuccessful.

Figure 5.12 shows the plot of peak strength for the laboratory size specimens in numerical modelling experiments, as well as the actual laboratory tests. The suffixes L and M stand for the laboratory and modelled specimens respectively. The figure shows similar peak strengths for the laboratory results and numerical modelling results. This implies that, given the accurate thermal properties, the numerical modelling could well be used to simulate the laboratory experiments.

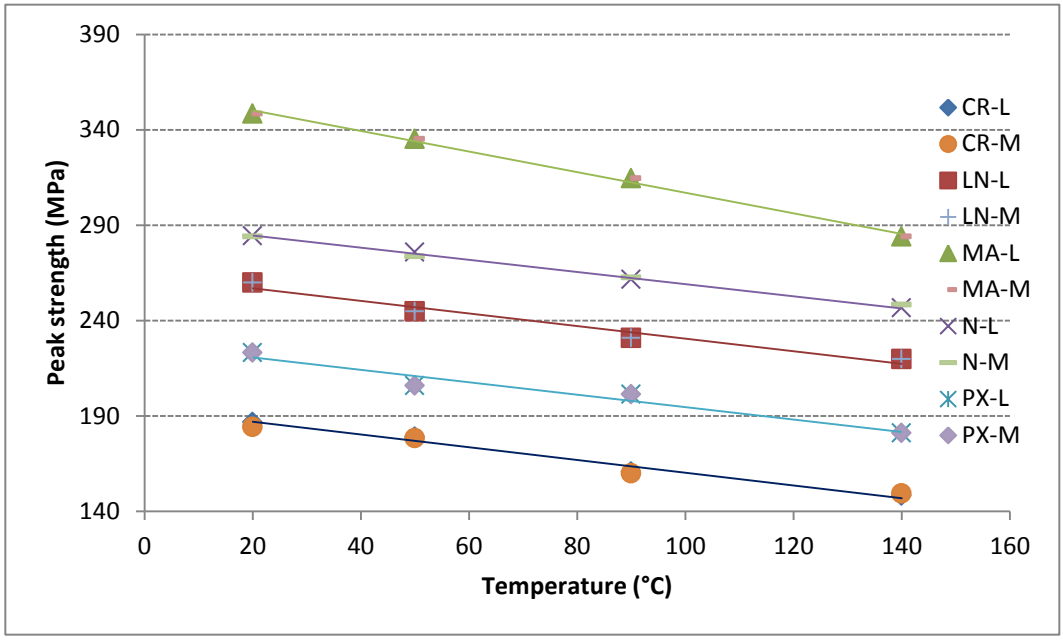


Figure 5.12: Plot of laboratory numerical modelling peak strengths

The numerical modelling stages presented above are known as model calibration and validation/verification. That is, matching the results of laboratory experiment with the numerical modelling under given experimental conditions (parameters). The next stage would be to make predictions by the alteration of critical parameters. It is intended perform sensitivity analysis by varying the confining pressure and temperature and observing the influence behaviour of the rocks, in terms of the extent of shear and tensile failure and peak strength. Figure 5.13 shows the plasticity plot for norite simulation at ambient temperature and no confinement. The orange colour represents parts of the specimen that have undergone shear failure, the parts shown as green remain elastic at the time of failure of the specimen, while the purple indicates tensile failure. Figures 5.14 and 5.15 show the results of the numerical modelling on norite and chromitite at various temperatures and confining pressures.

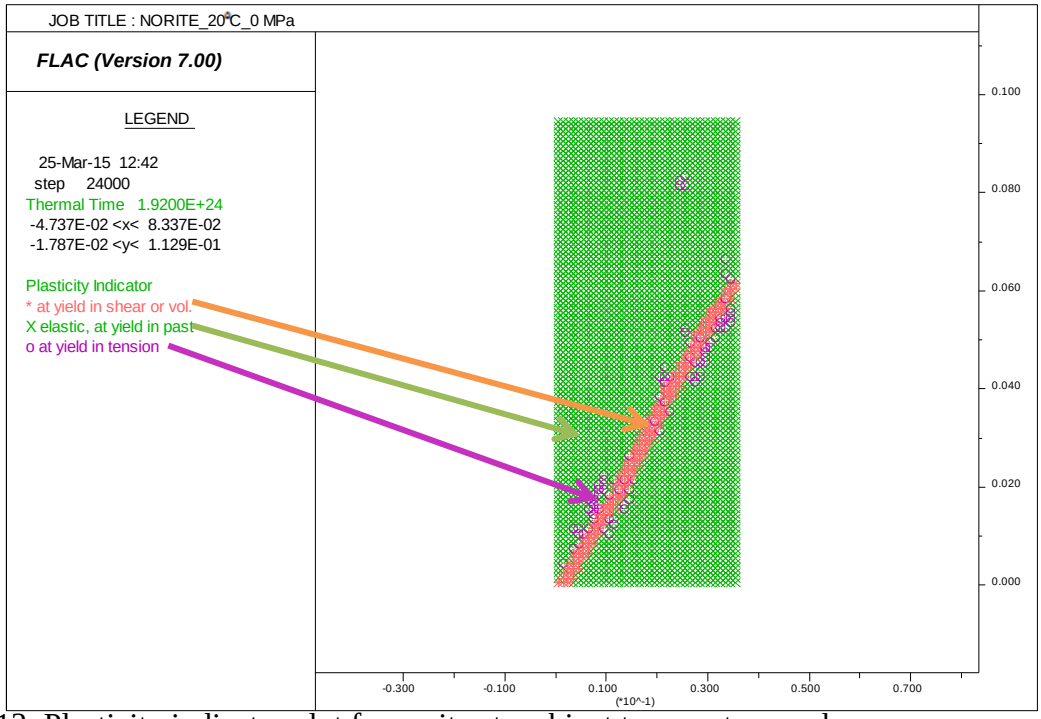


Figure 5.13: Plasticity indicator plot for norite at ambient temperature under no confinement.

A careful observation of the failed specimens (Figures 5.14 and 5.15), shows that the extent of tensile failure at the shear band increases with increasing temperature, and in contrast reduces with increasing confining pressure. In addition to this general observation, the extent of tensile failure is greater with norite than chromitite as shown in the plasticity plots. The possible reason for this is that norite has higher coefficient of thermal expansion than chromitite. This observation can be quantified by looking at Figure 5.14 and 5.15, tensile failure is noticed in norites sample tested in under uniaxial condition and at confining pressures of 10, 50 and 100 MPa for all temperature range considered. On the contrary, there are no tensile failures observed in chromitite tested at ambient temperature and 50°C, under confining pressure of 50 and 100 MPa. Once temperature increases to 90°C and 140°C, tensile failure becomes visible at confining pressures of 50 and 100 MPa.

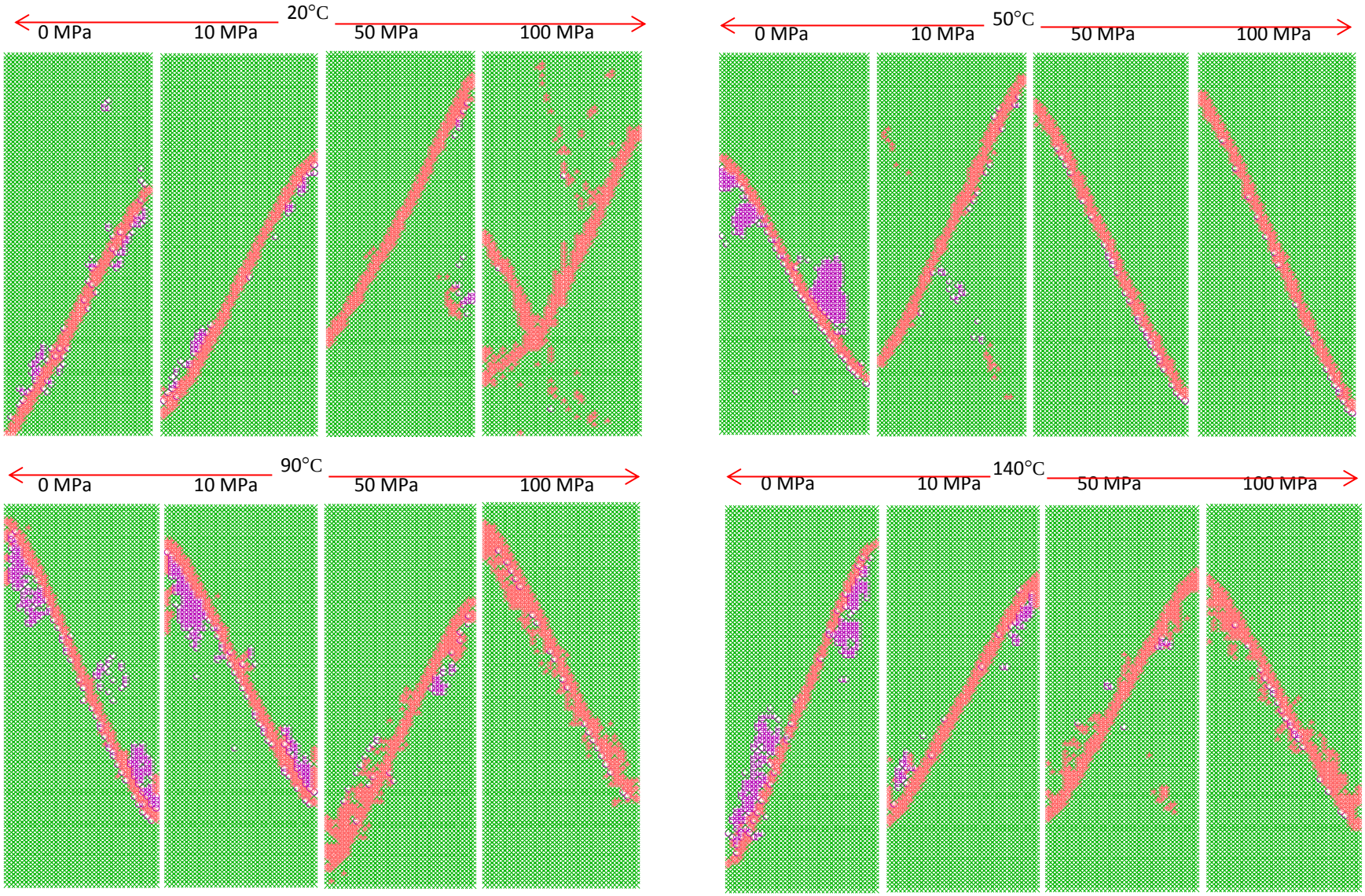


Figure 5.14: Plasticity indicator of norite sample at different temperature and confining pressure

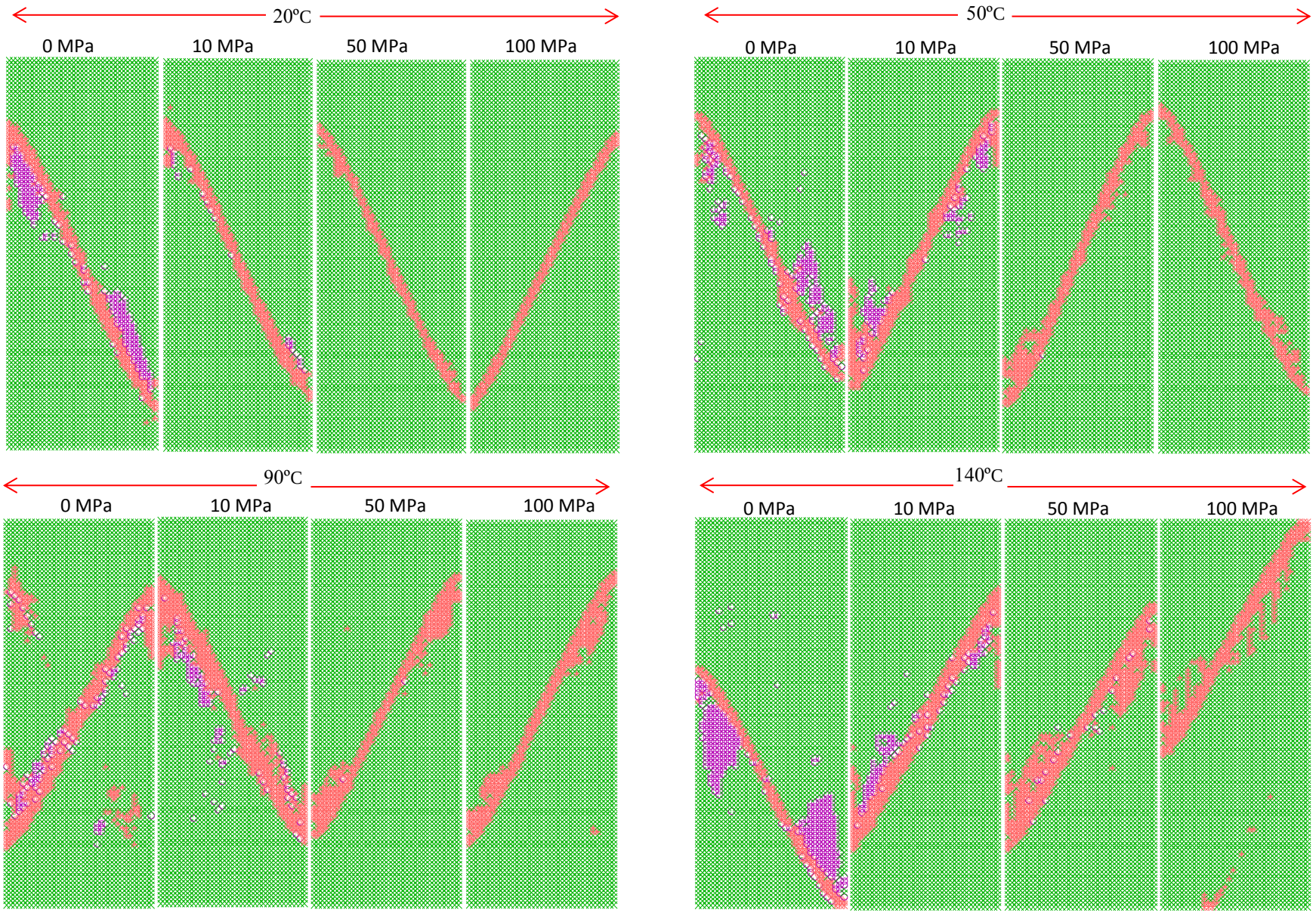


Figure 5.15: Plasticity indicator of chromitite sample at different temperature and confining pressure

Figures 5.16 and 5.17 show the plot of strength versus confining pressure at various temperatures for norite and chromitite respectively. The strength of norite and chromitite increases with increasing confinement. However, both rocks display strength reduction with increasing temperature. In the case of norite (Figure 5.16), the strength reduction is remarkable between ambient temperature, 50ºC and 140ºC, while the strength at 50ºC and 90ºC are similar. The effect of strength reduction due to temperature variation is smaller for chromitite at 50ºC as compared to 90ºC and 140ºC (Figure 5.17). In all cases, nevertheless, it is obvious that temperature plays an important role in the reduction of the strength of test specimens.

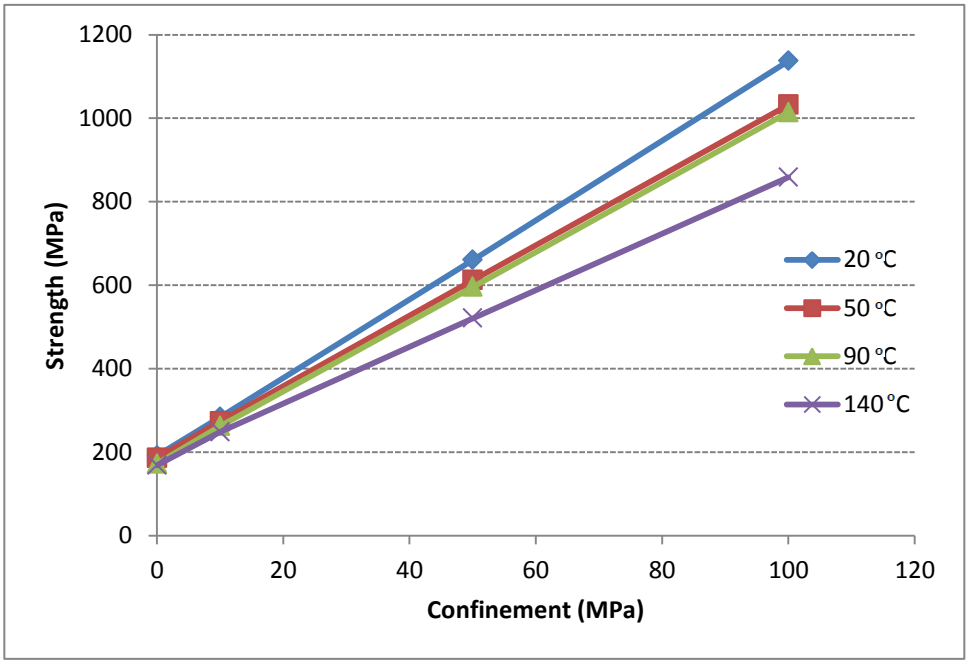


Figure 5.16: Peak strength of norite at various temperatures and confining pressure

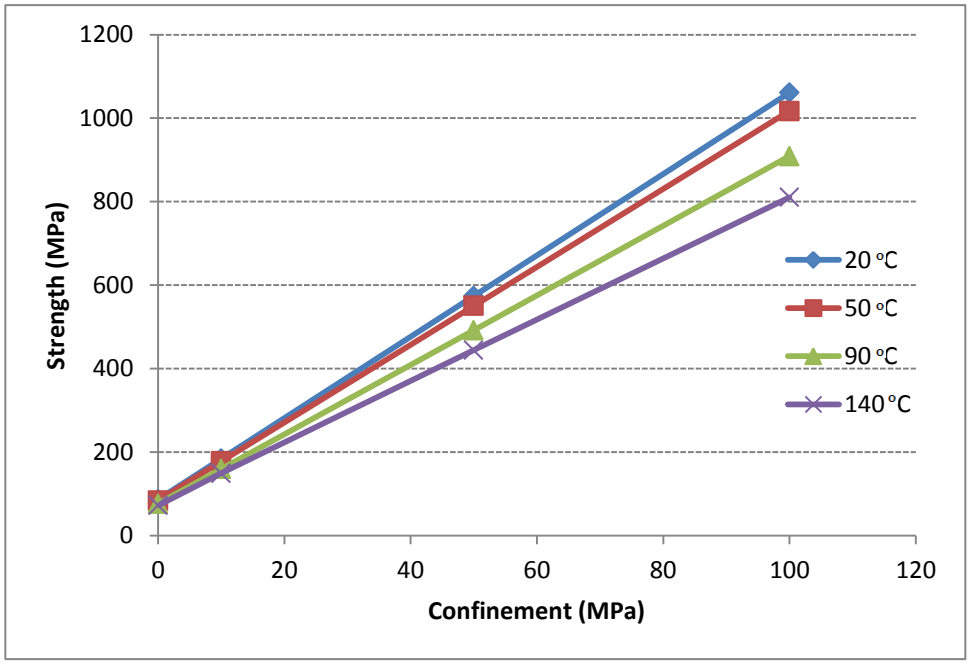


Figure 5.17: Peak strength of chromitite at various temperatures and confining pressure

Combining the observations from plasticity plots (Figures 5.14 and 5.15) and the strength plots (Figures 5.16 and 5.17), it is clear that increasing temperature has influence on the failure process and on the crack generation and extent that relates to the reduction in the strength of rocks. On the contrary, confinement increases strengths and reduces the extent of tensile failure. The reduction in tensile failure with increasing confinement can be observed in Figures 5.14 and 5.15 with reduction in the purple indicator.

5.3 FLAC 2D modelling of rock mass

The parameters for the modelling of rock mass are similar to the ones stated under intact rock modelling. The difference is that rock mass parameters such as tensile and compressive strength, Young's modulus, cohesion and friction angle were determined from intact rock parameters and Geological Strength Index (GSI) as described in

section 5.3.3. In addition, in-situ stresses are used as one of the input parameters in the modelling of rock mass, unlike the case of intact rock modelling, where confining pressure is used.

5.3.1 In-situ rock stresses

The in-situ stress measurement data was obtained through correspondence with the Principal Rock Engineer at Anglo American Platinum Limited (Priest, 2012). The method used for the stress measurement is overcoring technique. The primary data reported from the overcoring stress measurements are:

- magnitude and orientation (bearing and dip) of three principal stresses
- vertical major and minor horizontal stresses.

The summary of the principal stress magnitudes and their measurement dates are provided in Table 5.7. The angles shown in parenthesis are the orientations of stresses given in direction from north/dip. "k" ratios, k_1 and k_2 taking into account the major and minor horizontal stresses are also included in the table.

From Table 5.7, the average k_1 for the depth range of 297 m – 472 m and 1097 m - 1130 m are 1.57 and 1.20 respectively, while k_2 for the same depth range are 1.43 and 0.92 respectively. This is in agreement with values presented by Stacey and Wesseloo, (1998) as shown in Figures 5.18 and 5.19. The k ratios, k_1 and k_2 calculated from the data obtained from the mines are included the in Figures 5.18 and 5.19 as red squares.

Table 5.7: Principal stresses from platinum mines (Priest, 2012)

S/N	Mines	σ_1 (MPa)	σ_2 (MPa)	σ_3 (MPa)	*σ_v (MPa)	*σ_{h2} (MPa)	*σ_{h1} (MPa)	k1	k2	Date	Depth (m)	Borehole number	Borehole position
1	Lebowa	16 ($11^o/33^o$)	9 ($263^o/26^o$)	4 ($144^o/46^o$)	8.5	8.1	11.9	1.4	1.0	1999	297	6E	6 Level Haulage East
2	Lebowa	30 ($128^o/1^o$)	21 ($218^o/13^o$)	10 ($35^o/77^o$)	10	24	26	2.4	2.6	1999	472	9E	9 Level Haulage East
3	Lebowa	36 ($76^o/13^o$)	25 ($329^o/52^o$)	16 ($175^o/35^o$)	22	19	35	0.9	1.6	1999	470	9W	9 Level Haulage West
4	Rustenburg	55.1 ($227^o/29^o$)	32.7 ($124^o/21^o$)	26.1 ($3^o/53^o$)	33.6	38.4	41.9	1.1	1.2	2004	1097	1	Frank shaft- 33 level-hanging wall
5	Rustenburg	47.1 ($224^o/17^o$)	28.5 ($128^o/19^o$)	19.9 ($351^o/64^o$)	23.1	35.8	36.7	1.5	1.6	2004	1097	2	Frank shaft- 33 level-on reef
6	Rustenburg	40.3 ($119^o/45^o$)	31.5 ($318^o/44^o$)	25.8 ($219^o/9^o$)	35.8	29.2	32.7	0.8	0.9	2004	1204	6	Frank shaft- 36 level-foot wall
7	Rustenburg	63 ($-9^o/20^o$)	26 ($-174^o/20^o$)	15 ($83^o/5^o$)	30	16	58	1.9	0.5	2007	1080	1	Turffontein shaft- 32 level
8	Rustenburg	44 ($85^o/34^o$)	32 ($-67^o/53^o$)	23 ($-176^o/14^o$)	35	24	40	0.7	1.1	2007	1130	2	Turffontein shaft- 32 level

* σ_v is the vertical stress, while σ_{h1} and σ_{h2} are the major and minor horizontal principal stresses respectively.

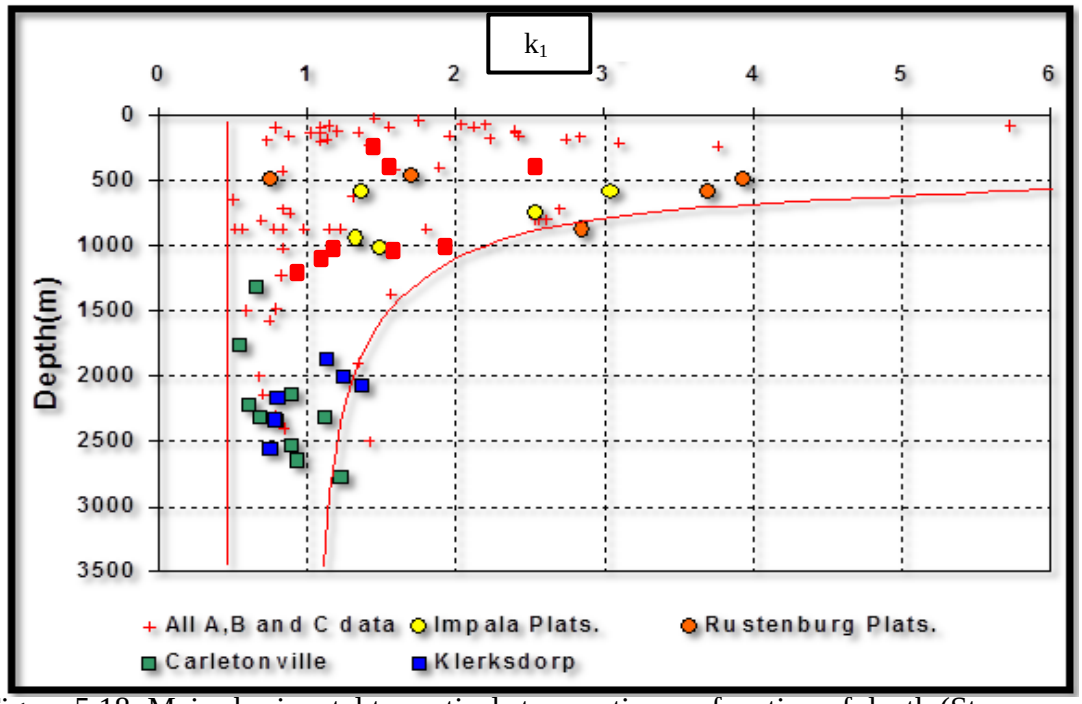


Figure 5.18: Major horizontal to vertical stress ratio as a function of depth (Stacey and Wesseloo, 1998)

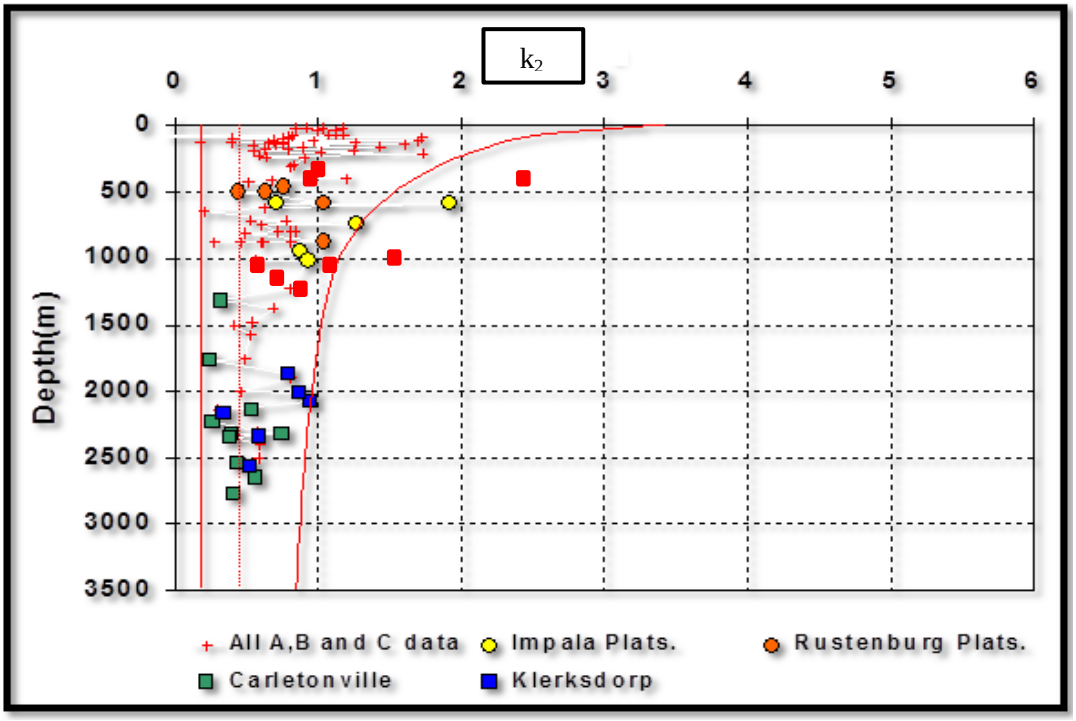


Figure 5.19: Minor horizontal to vertical stress ratio as a function of depth (Stacey and Wesseloo, 1998)

The average densities (kg/m^3) of the rocks from the Bushveld Igneous Complex is given in Table 5.8

Table 5.8: Densities (kg/m^3) of rocks from the platinum mines

ANCR	CR	LN	MA	N	PX	VTA	Average
2853	4049	2776	2744	3045	3194	2766	**3061**

The average of all rock densities is 3061 kg/m^3. This is the value used in the calculation of the vertical stress in numerical modelling.

5.3.2 Stress magnitudes used for modelling

Handley (2013) suggested a generic pre-mining linear stress model for southern Africa (equation 5.3).

$$\left.\begin{aligned} \sigma_v &= 81 + 0.027(h - 3000)MPa \\ \sigma_{h1} &= 87 + 0.026(h - 3000)MPa \\ \sigma_{h2} &= 48 + 0.015(h - 3000)MPa \end{aligned}\right\} \quad (5.3)\ \text{(Handley, 2013)}$$

Where σ_v is the vertical stress, σ_{h1} is the major horizontal stress, σ_{h2} is the minor horizontal stress, h is the depth below surface.

The model was derived from plots of 180 consistent in-situ stress measurements through a combination of the gradient and intercept of the graph (Figure 5.20).

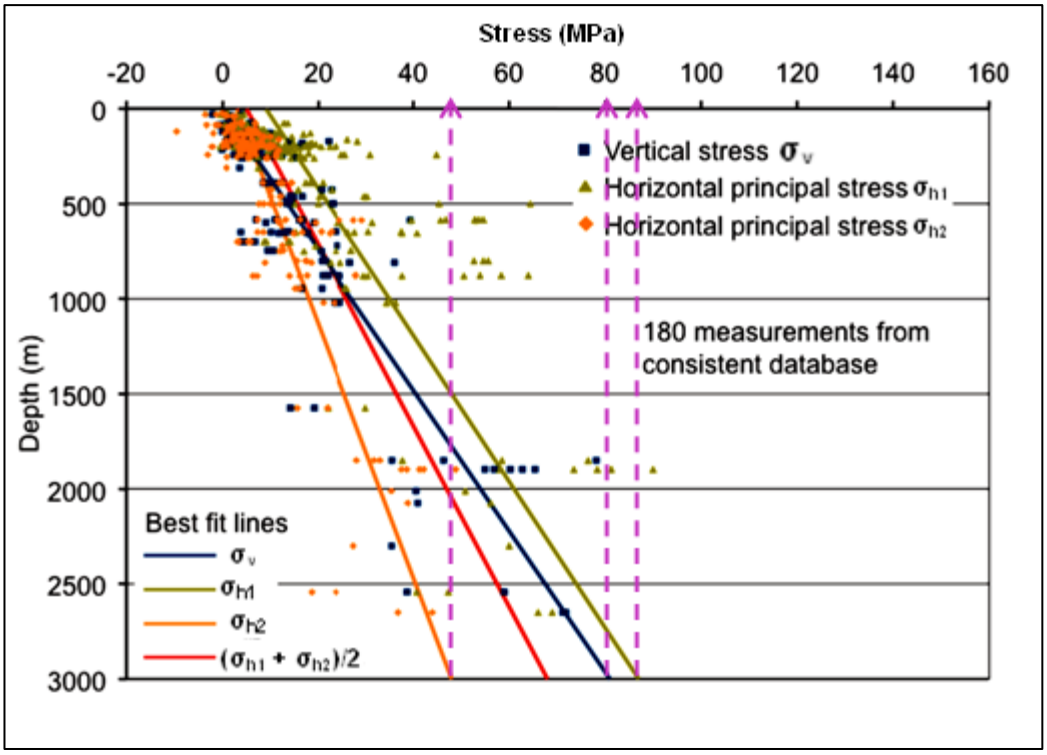


Figure 5.20: Plot of consistent stress measurement database (Handley, 2013).

Handley (2013) used a density of 2700 kg/m^3 in equation 5.3, which is derived from the Southern African stress measurement database. The average rock density in the platinum mines, however, is approximately 3061 kg/m^3, therefore, equation 5.3 is modified by replacing the gradient of the vertical stress, 0.027 with 0.03061. The ratio 0.03061/0.027, that is, 1.134 was used to adjust the intercept and gradient for the major and minor horizontal stress in equation 5.3. The modified equations, for the calculation of the stresses (Table 5.9) in FLAC 2D modelling are given in equation 5.4 as:

$$\left.\begin{aligned} \sigma_v &= 91.8 + 0.03061(h - 3000)MPa \\ \sigma_{h1} &= 98.1 + 0.0297(h - 3000)MPa \\ \sigma_{h2} &= 54 + 0.017(h - 3000)MPa \end{aligned}\right\} \quad (5.4)$$

Table 5.9: Vertical and horizontal stresses used for numerical modelling

S/N	Temperature (°C)	Depth (m)	σ_v (MPa)	σ_{h1} (MPa)	σ_{h2} (MPa)	k_1	k_2
1	50	1073.1	32.8	40.9	21.2	1.25	0.65
2	90	2835.2	86.8	93.2	51.2	1.07	0.59
3	140	5037.9	154.2	158.6	88.6	1.03	0.57

5.3.3 Determination of rock mass properties for numerical modelling

The rock mass properties were determined with the use of a rockscience software "RockLab" (Figure 5.21) by inputting the values of the Hoek-Brown parameters, σ_{ci} (intact uniaxial compressive strength), GSI (geological strength index), m_i, D (disturbance factor) and E_i (intact Young's modulus). The Hoek-Brown parameters, from triaxial strength data, were used to generate the Mohr-Coulomb fit, c (cohesion), Ø (friction angle) and rock mass parameters, σ_t (tensile strength), σ_c (uniaxial compressive strength), σ_{cm} (rock mass strength) and E_{rm} (rock mass deformation modulus).

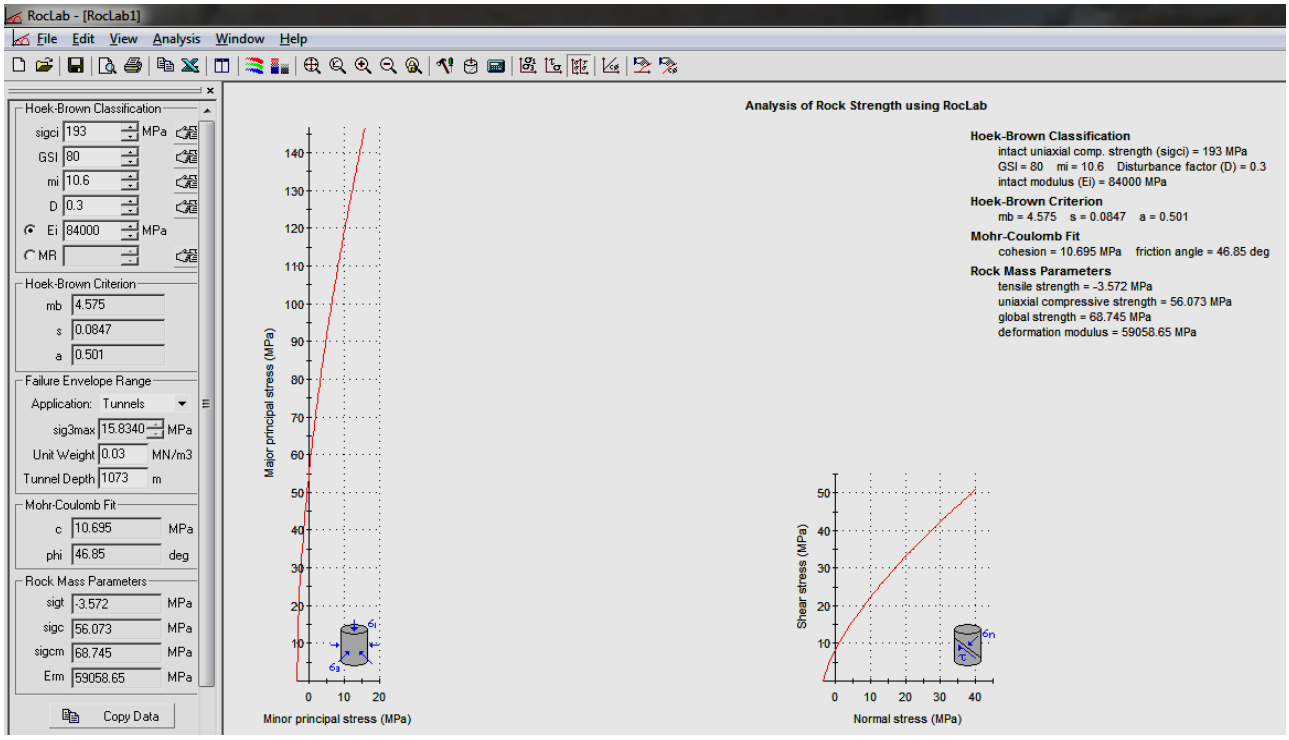


Figure 5.21: Screen shot of RocLab software used for the determination of rock mass parameters

Malan and Napier (2011) suggested the use of an RMR value of 94 and 95 for UG2 and Merensky reef respectively at Lonmin's BIC mine. Using the relation, GSI = RMR – 5, the GSI values for UG2 and Merensky reef are 89 and 90 respectively. Watson (2010) stated that the Barton-Q value for rock mass at Amandelbult (shallow depth, k-ratio = 1), Impala (intermediate depth, k-ratio = 1.3), and Union (intermediate depth, k-ratio = 0.5) mines are 18.3, 50 and 3.2 respectively. Using the relation, GSI = 9lnQ + 44, the GSI values for the respective mines are 70.2, 79 and 53. Based on the GSI values reported by Malan and Napier (2011) and Watson (2010) from the different mines, an average value of 80 is used for BIC. The disturbance factor (D) was considered to be 0.3. Hoek et al (2002) described D as a factor which depends upon the degree of disturbance to which the rock mass has been subjected by blasting damage and stress relation. It varies from 0 for undisturbed in-situ rock masses to 1 for very disturbed rock mass. They asserted that a large number of factors influence the degree of disturbance in the rock mass and that it may never be possible to quantify these factors precisely.

Hoek et al (2002) attempted to draw up a set of guidelines for estimating the factor D. When D = 0, it means excellent quality controlled blasting, excavation by tunnel boring machine or mechanical/hand excavation in poor quality rock with minimal disturbance to the surrounding rock. D value of 0.5 represents a situation where squeezing problems result in significant floor heave, while D value of 0.8 is for very poor quality blasting in hard rock tunnel which causes severe local damage. The excavations at platinum mines are assumed to have D value, which falls between 0 and 0.5. A value of 0.3 is adopted for this modelling based on the above discussions and a report from Sellers (2011) suggesting cautious blasting such as presplitting and smooth blasting are not always applied in deep level mines. Table 5.10 summarises the values of σ_{ci}, m_i, and E_i obtained from laboratory testing of rock specimens (Chapter 3), while Table 5.11 presents the rock mass cohesion, friction angle, Young's modulus and tensile strength as determined from RockLab.

Table 5.10: Intact σ_{ci} , m_i and Young's modulus.

Temperature (°C)	**MA**			**CR**			**N**			**PX**			**LN**		
	σ_{ci} (MPa)	m_i	E_i (GPa)	σ_{ci} (MPa)	m_i	E_i (GPa)	σ_{ci} (MPa)	m_i	E_i (GPa)	σ_{ci} (MPa)	m_i	E_i (GPa)	σ_{ci} (MPa)	m_i	E_i (GPa)
50	193	10.6	84	75	8.3	56	161	7.4	78	165	6.4	119	168	7.4	77
90	185	10.5	82	73	7.6	54	160	7.1	74	164	5.9	115	163	7.4	74
140	180	10.4	80	71	7.4	52	159	6.8	71	163	4.5	113	159	6.8	71

Table 5.11: Rock mass cohesion, friction angle, Young's modulus and tensile strength as determined from RockLab.

	MA				**CR**				**N**				**PX**				**LN**			
DEPTH	C (MPa)	Ø (°)	E_{rm} (GPa)	σ_t (MPa)	C (MPa)	Ø (°)	E_{rm} (GPa)	σ_t (MPa)	C (MPa)	Ø (°)	E_{rm} (GPa)	σ_t (MPa)	C (MPa)	Ø (°)	E_{rm} (GPa)	σ_t (MPa)	C (MPa)	Ø (°)	E_{rm} (GPa)	σ_t (MPa)
1073	10.7	46.9	59	-3.6	6.5	35.8	40	-1.8	9.9	42.1	55	-4.3	10.4	40.4	83	-5.0	10.0	42.9	54	-4.4
2835	14.2	40.4	58	-3.5	9.9	27.7	38	-1.9	13.3	35.0	52	-4.4	13.6	30.0	81	-5.5	13.0	36.1	52	-4.3
5038	18.1	35.8	56	-3.4	13.2	23.3	36	-1.9	16.7	30.3	50	-4.6	16.5	26.7	79	-7.1	16.1	31.0	50	-4.6

Table 5.12: Rock mass shear (G) and bulk (K) modulus and dilation angle (ψ)

	MA			**CR**			**N**			**PX**			**LN**		
DEPTH	G (GPa)	K (GPa)	ψ (º)	G (GPa)	K (GPa)	ψ (º)	G (GPa)	K (GPa)	ψ (º)	G (GPa)	K (GPa)	ψ (º)	G (GPa)	K (GPa)	ψ (º)
1073	21.9	71.7	11.9	13.9	87.8	9.0	20.7	51.5	10.5	33.6	53.9	10.1	20.1	57.0	10.7
2835	21.4	71.3	10.1	13.3	82.8	6.9	19.4	55.9	8.7	32.5	52.2	7.5	19.4	52.3	9.0
5038	20.6	67.6	8.9	12.7	93.6	5.8	18.7	49.8	7.6	31.9	51.6	6.7	18.7	47.8	7.8

The shear and bulk modulus calculated from rock mass Young's modulus and Poisson's ratio are presented in Table 5.12. Also included in the table is the rock mass dilation angle that was calculated by dividing the rock mass friction angle by 4 as suggested by Hoek and Brown (1997) for very good quality rocks.

5.3.4 Model set up

The numerical modelling analysis was done with FLAC version 7.00. Egerton (2004) reported that average thickness of UG2 reef is 70 cm to 75 cm which is normally mined at stoping width of 1 m to avoid grade dilution. Egerton (2004) made comparison between different mining methods that can be employed in the extraction of UG2 reef. Of the different methods stated, he reported a range of panel length of 8 to 30 m and concluded that a panel length of 10 m gave the best extraction rate. Based on this, a stope with dimension of 10 m by 1 m (length by height) was considered for the numerical modelling analyses.

The design is for mechanized/hybrid dip pillar mining method. The method, as described by Egerton (2004), involves stoping of panels 10 m long on either side of two roadways, both down dip and up dip at planned stoping width (1 m). The panels are drilled with hand-held rockdrills on air legs. The broken rock is throw-blasted into the dip roadways. The run-of-mine is loaded with a low profile load-haul-dump truck. In order to avoid complexities, only a single panel is modelled.

For the purpose of modelling, a block of 200 by 61 m was generated, from which a stope of 10 m by 1 m was excavated (Figure 5.22) centrally in the block. This excavation was made farther away from the modelling boundary to avoid boundary effect, which could affect stress distribution in the model. Budavari (1983) developed analytical plane strain solution of vertical stress, σ_z, along the centre of a single parallel-sided panel, which is given as:

$$\sigma_z = \frac{qz}{H} + \frac{q|z^3|}{\sqrt{(l^2+z^2)^3}} \qquad (5.5)$$

Figure 5.23 shows the plot of equation 5.5. As observed from the figure, the virgin stress level of 32 MPa at a depth of 1037 m can only be reverted back at a vertical distance of 20 m or more above the panel.

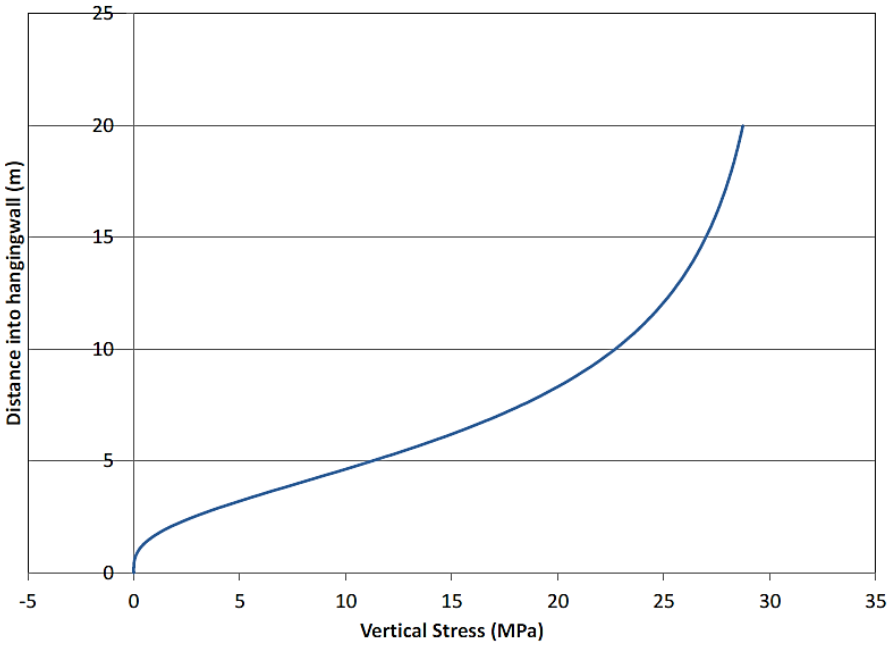


Figure 5.23: Plot of equation 5.5 (Malan (2015), personal communication.)

Based on this, a vertical boundary of 30 m above and below the panel was used, which gave a total of 61 m as the vertical extent of the model. A horizontal extent of 200 m was used.

Figure 5.24 illustrates the fixed boundaries and the excavated stope. As can be seen in the figure, the mesh close to the excavation is made finer than the mesh far away from the excavation in order to capture model histories close to the excavation in more detail. In the model, the footwall, hangingwall and reef are norite, pyroxenite and chromitite respectively. The physical, mechanical and thermal properties were assigned (Figure 5.25) accordingly for the rock types. Pinned boundary condition was assigned to the top, bottom and both sides of the model since there is no part of the model that has free surface.

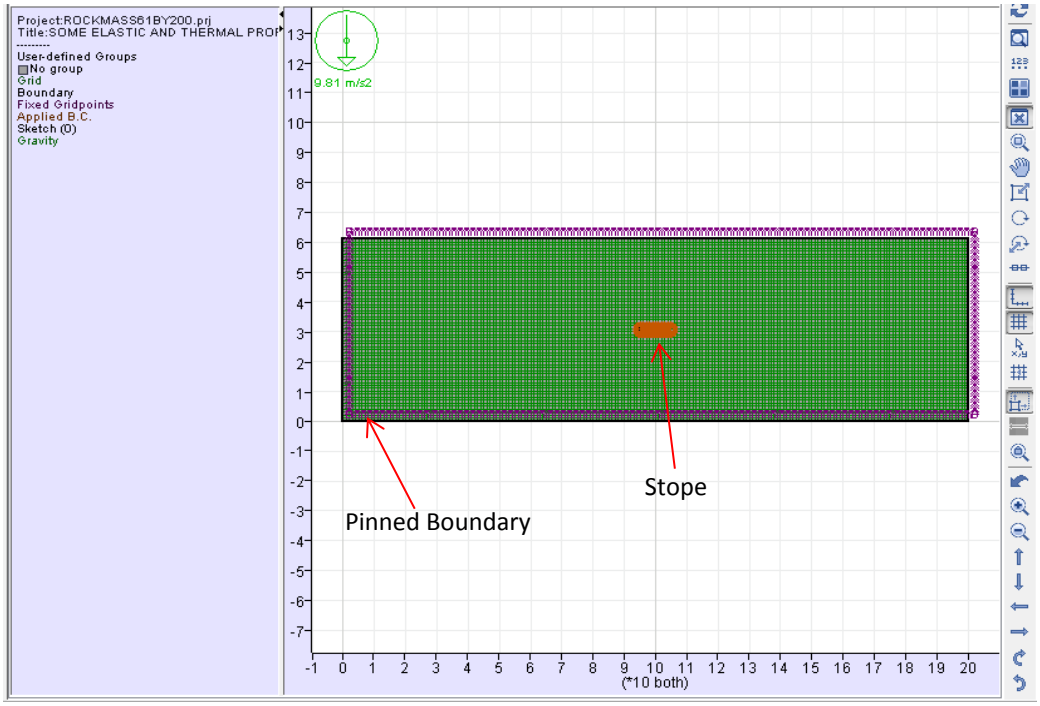


Figure 5.24: Illustration of fixed boundaries and the stope

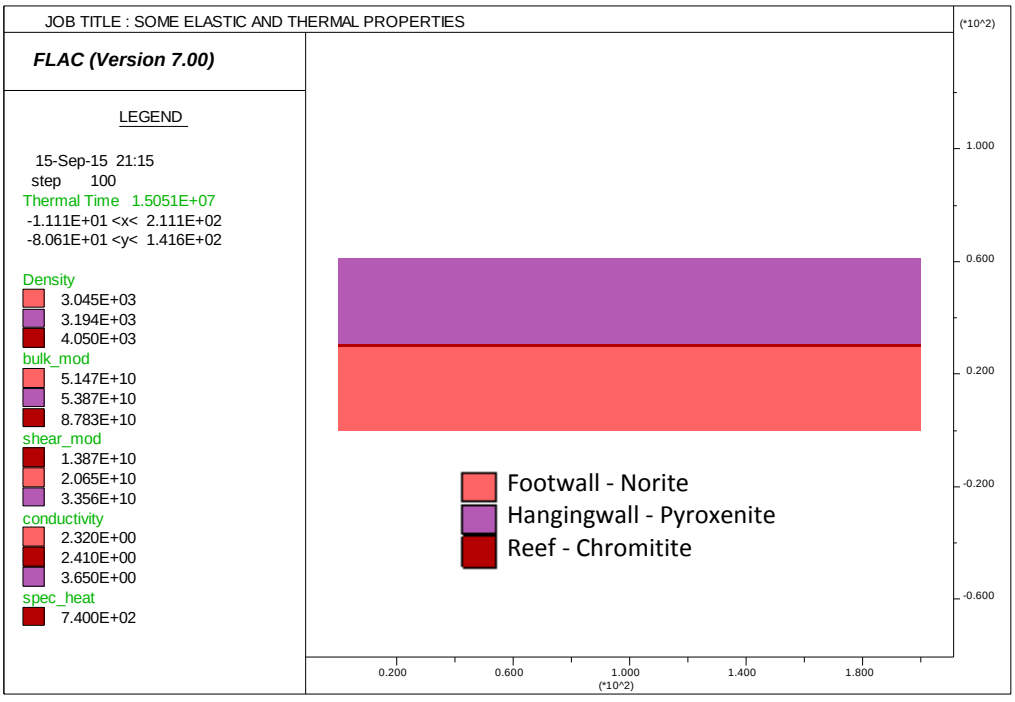


Figure 5.25: Some of the model properties for excavation at a depth of 1073 m.

Temperature corresponding to different depths were given as initial condition except that excavated part of the model is assigned a temperature of 27ºC, which represents the part that have been cooled by ventilation as shown in Figure 5.26 and in this particular case, the depth is 1073 m below surface. As observed from the figure, there is temperature variation between the immediate excavation walls and a few meters into the host rock.

In-situ stresses were then assigned to the model. For the three depths modelled, the major horizontal stress (sxx), vertical stress (syy) and the minor horizontal stress (szz) are the major, intermediate and minor principal stresses respectively. The detail of the assigned in-situ stresses and the k-ratio is given in Table 5.9. The acceleration due to gravity is set to be 9.81 m/s^2, while the model was executed in large strain mode. The model was first cycled until the desired temperature is reached, and in the meantime, the mechanical calculation is turned off to allow for only thermal cycling. Thereafter, the mechanical is turned on and thermal option is turned off, to allow for mechanical calculation to be effective. Figure 5.27 shows the xx, yy and zz – components of in-situ stresses initialized in the model before excavation. The stress gradient option in FLAC was used to reproduce the effect of increasing stress with depth along 7 m long vertical section of the model.

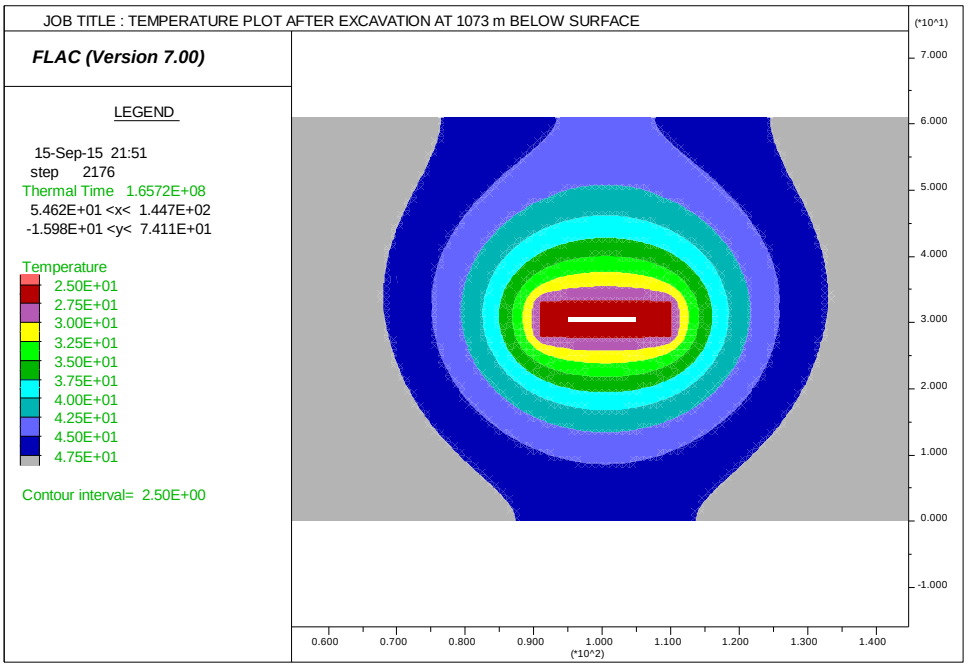


Figure 5.26: Temperature plot for the stope at 1073 m below surface.

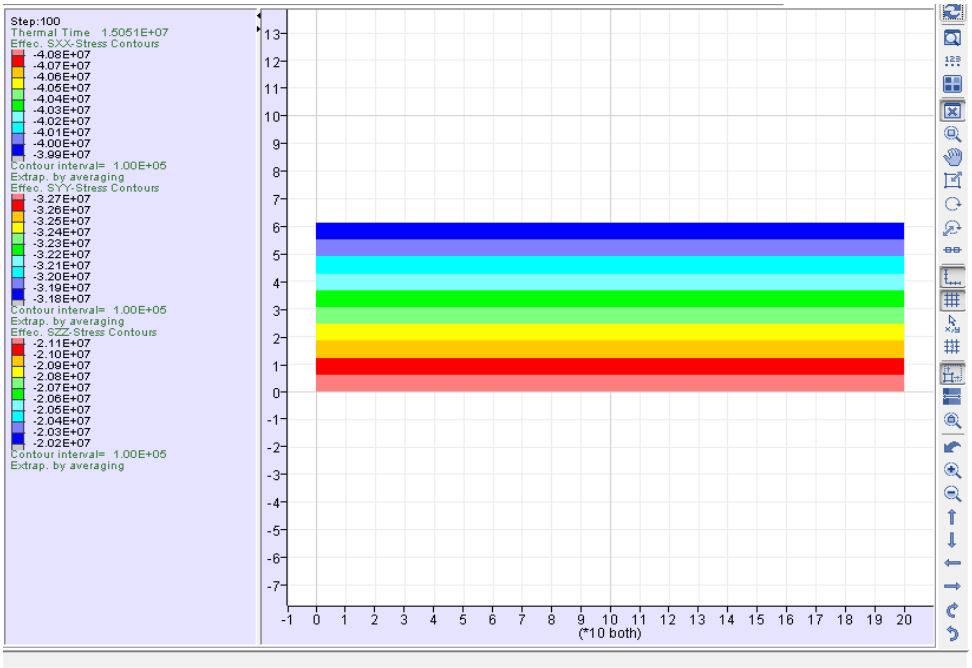


Figure 5.27: Plot of the pre-mining in-situ stresses at 1073 m below surface

It should be noted that negative stress in FLAC means compression. “ZONK” Fish function was used for the excavation. The function creates void within a model, and slowly relaxes the forces around the void region. It allows gradual extraction of the region of zones to simulate excavation by minimizing the influence of transients on material (Itasca Consulting Group, 2012).

The extent of deformations or damage on the footwall, hangingwall and sidewall in the model was determined by:

1. State plots
2. Horizontal and vertical displacements, that is, relative movement of the footwall, hangingwall and sidewalls.

5.3.5 State Plot

The plot displays the zones in which the stresses satisfy the Mohr-Coulomb yield criterion that is indicative of areas where plastic flow is occurring. It should be noted that initial plastic flow often occurs at the beginning of a simulation; however, subsequent stress redistribution unloads the yielding elements so that the stresses do not satisfy the yield criterion. In the state plots, these non-yielding parts are referred to as “yield in past”. The parts that satisfy the yield criterion indicate tensile or shear failure (Itasca Consulting Group, 2012).

The state plots of the model for excavations at 1073, 2835 and 5038 m below surface are given in Figures 5.28 to 5.30, while Figure 5.31 shows the temperature plot. The state plot for 1073 m (Figure 5.28) shows the presence of shear and tensile failures. However, the extent of these failures are smaller as compared to those of 2835 and 5038 m. Figure 5.30 reveals that there is more shear failure at 2835 m than at 1073 m and even at 5038 m, however, tensile failure at 5038 m is much greater. This could be attributed to higher in-situ stresses and virgin rock temperatures. As expected,

horizontal and vertical displacements are also increasing, as will be shown later with displacement plots, although they are not noticeable in Figure 5.29.

One of the reasons for the increase in the tensile failure at this depth could be the rapid cooling of the excavation wall from 140ºC to approximately 40ºC (Figure 5.31). The combined effect of high temperature variation and mining induced stresses result in the development of micro-cracks, which coalesce to form tensile failure. Castro et al (2012) stated that at great depth, common failure types are stress-induced failures in the form of spalling and slabbing, in addition to structurally-controlled gravity-driven failures. These failures are attributed to the reduction of radial stresses and increasing tangential stresses. Castro et al (2012) also explained that within the near-surface zones of the rock mass surrounding an opening, the failure process weakens the rock mass. This explains the nature of horizontal and vertical displacement at 5038 m.

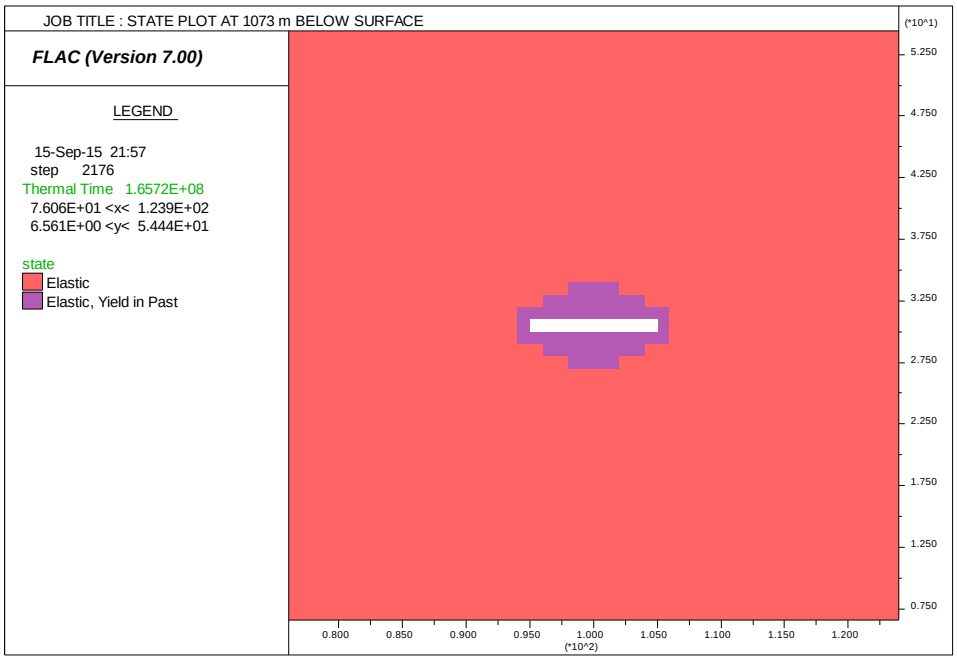


Figure 5.28: State plot at 1073 m below surface

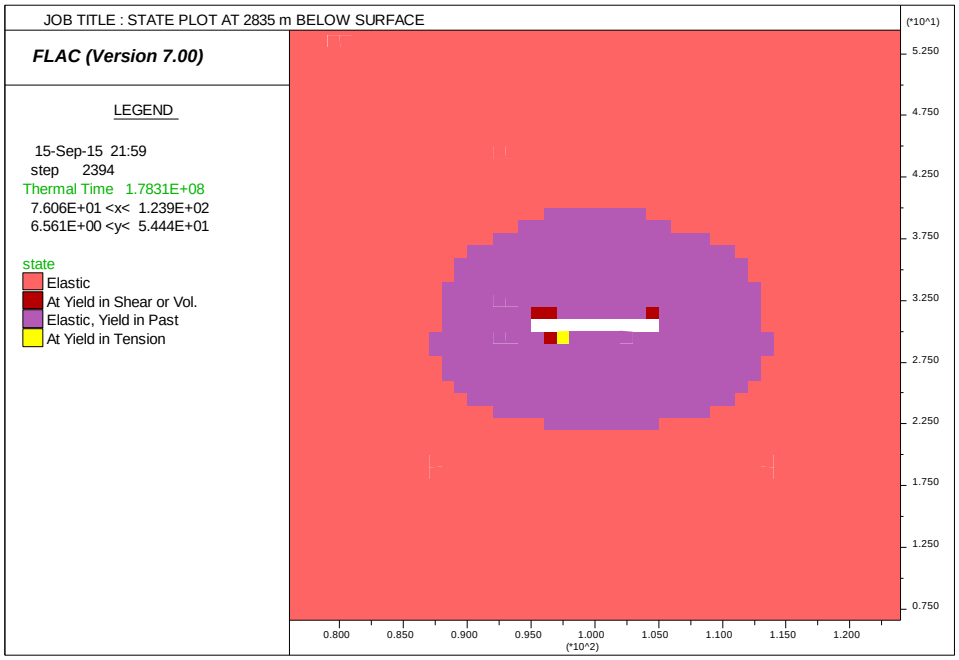


Figure 5.29: State plot at 2835 m below surface

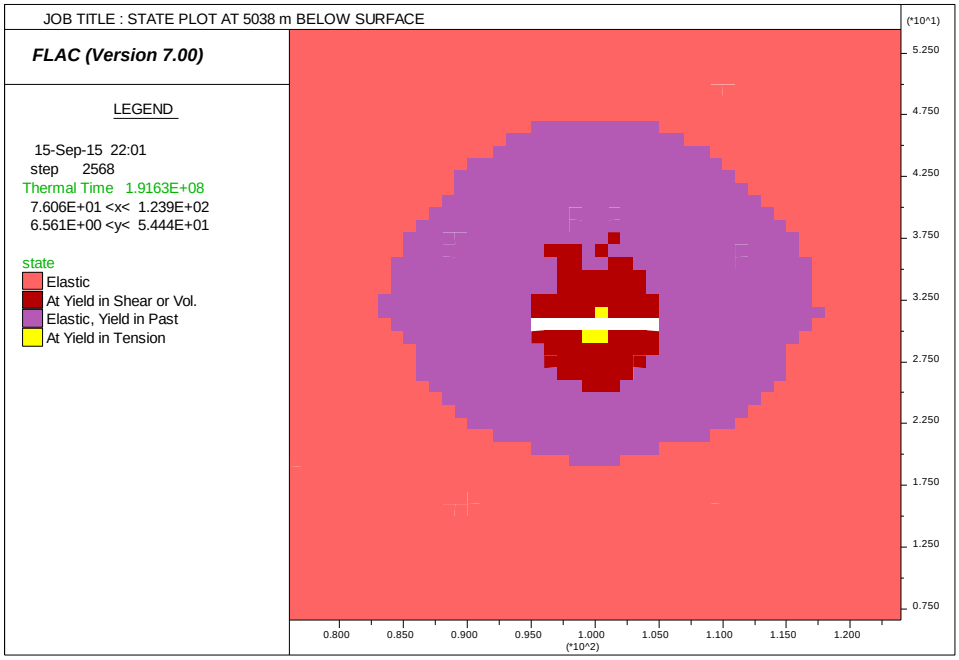


Figure 5.30: State plot at 5038 m below surface

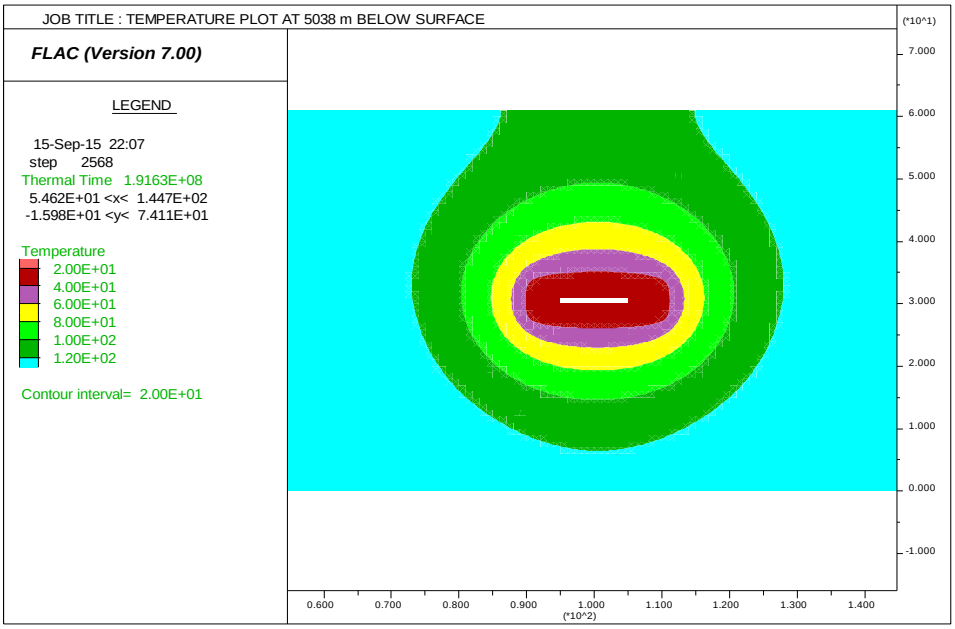


Figure 5.31: Post-excavation temperature at 5038 m below surface

5.3.6 Horizontal and vertical displacements

The aim of including the horizontal and vertical displacement plots is to examine the indications that in-situ stresses and temperature would cause at ultra-deep levels in the platinum mines. Malan and Basson (1998) noticed severe case of squeezing at Hartebeestfontein Gold Mine. Squeezing, as defined in Malan and Basson (1998) is the time-dependent large deformation which occurs around the excavation, and is essentially associated with creep caused by exceeding of limiting shear stress.

Malan and Basson (1998) presented a graph which shows a squeezing line, above which there is no squeezing (Figure 5.32). The average UCS of pyroxenite, chromitite and norite, which are the hangingwall, reef and footwall rock types respectively, are included in the graph. The graph indicates that chromitite, norite and pyroxenite will experience squeezing conditions at depths of about 1400 m, 2950 m and 3100 m respectively.

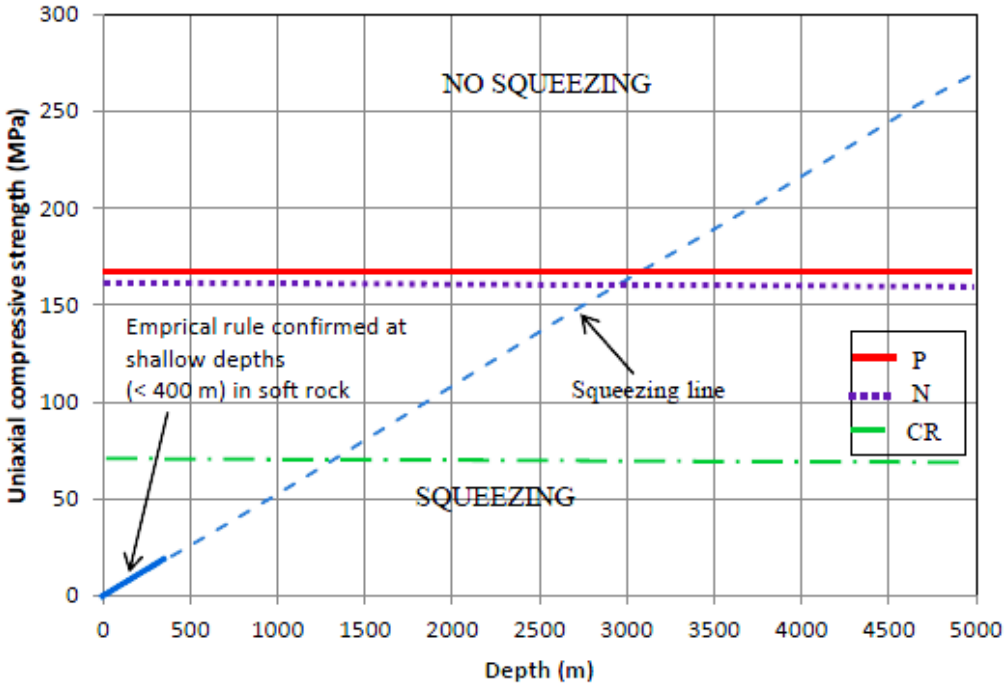


Figure 5.32: Hypothetical squeezing conditions of ultra-deep mining excavations in hard rocks (Malan and Basson, 1998)

The horizontal and vertical displacement plots were used to monitor the relative displacement of hangingwall and sidewalls in the model. Vertical displacement (or convergence), ΔV, is determined by considering the relative movement of the hangingwall and footwall, while the horizontal displacement, ΔV, is determined by taking the relative movement of the sidewalls into account (Figure 5.33). V, H and V_f, H_f are the vertical and horizontal distance before and after stope is excavated respectively. Figures 5.34 to 5.36 show the horizontal and vertical displacement plots for all depths under consideration.

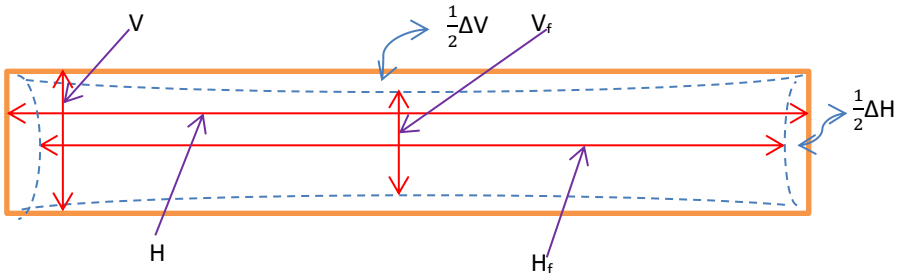


Figure 5.33: Illustration of horizontal and vertical displacements

As observed in Figures 5.34 to 5.36 and Table 5.13, both the horizontal and vertical displacements increase with increasing depth. In summary, the results show that mining at ultra-deep levels will pose challenge of increase in horizontal and vertical displacements. Sensitivity analysis was done to check the influence of temperature only on the displacements. The detail of the analysis is presented in section 5.5.

Table 5.13: Summary of horizontal and vertical displacements

Depth (m)	Horiz. Displ (mm)	Vert. Displ (mm)
1073	2.0	1.5
2835	13.6	19.6
5038	35.8	62.9

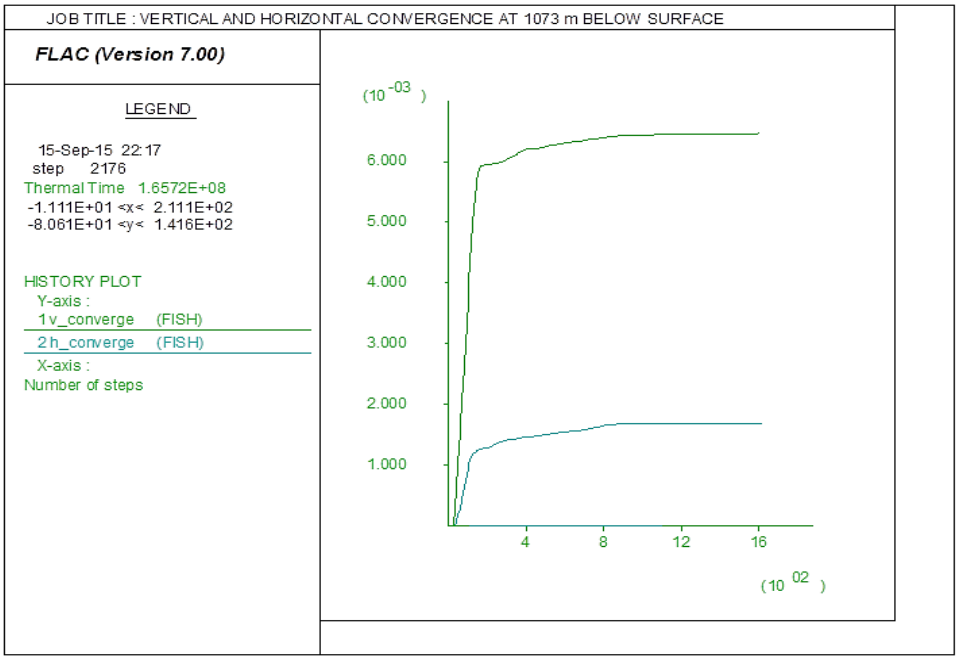


Figure 5.34: Plot of vertical and horizontal displacements at 1073 m below surface

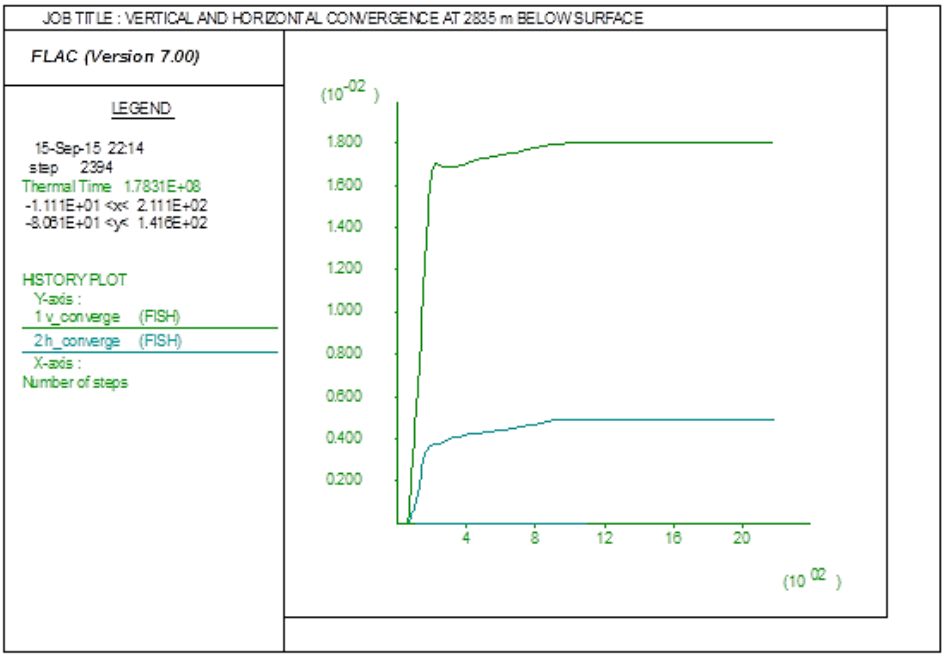


Figure 5.35: Plot of vertical and horizontal displacements at 2835 m below surface

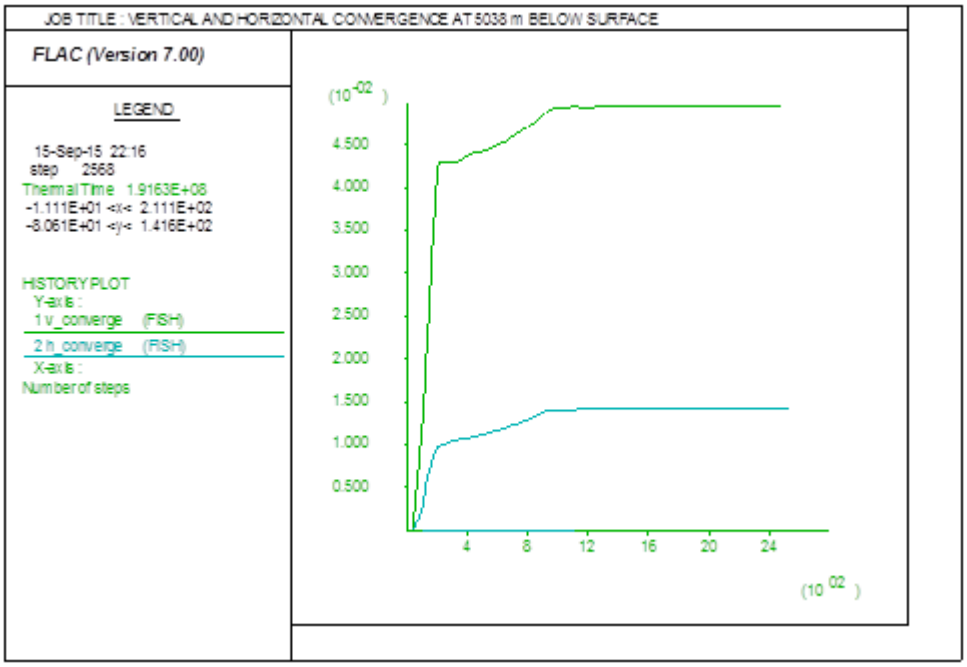


Figure 5.36: Plot of vertical and horizontal displacements at 5038 m below surface

5.3.7 Prediction of depth of failure

As stated in chapter two, equation 5.6 is the constant deviatoric stress equation proposed by Martin et al (1999) for depth of failure prediction in brittle rock mass.

$$\frac{\sigma_1-\sigma_3}{\sigma_c} = 0.33 \qquad (5.6)$$

The equation 5.6 is written as a FISH function (Appendix A9) and included in the model for the evaluation of the extent and depth of failure in the hangingwall and sidewall. The points in the sidewall are labelled as s1, s2, and s3 while that of hangingwall are represented as h1, h2, and h3. The failures were examined at intervals of 1, 2 and 3 m from the skin of the stope in both hanginwall and sidewall, as shown in Figure 5.37.

Figures 5.38 to 5.43 present the plot of the failure of the hangingwall and the sidewall against time step.

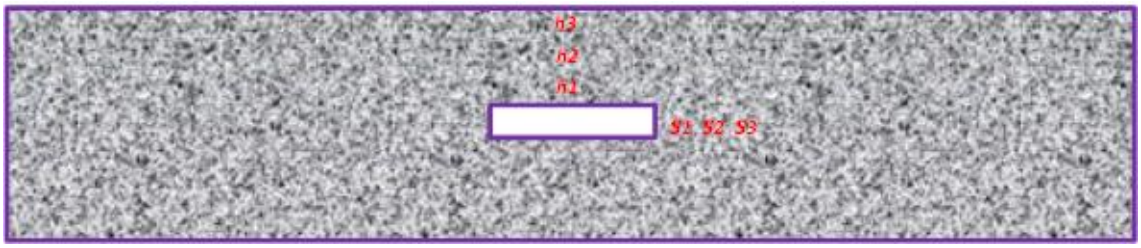


Figure 5.37: Illustration of failure measurement intervals

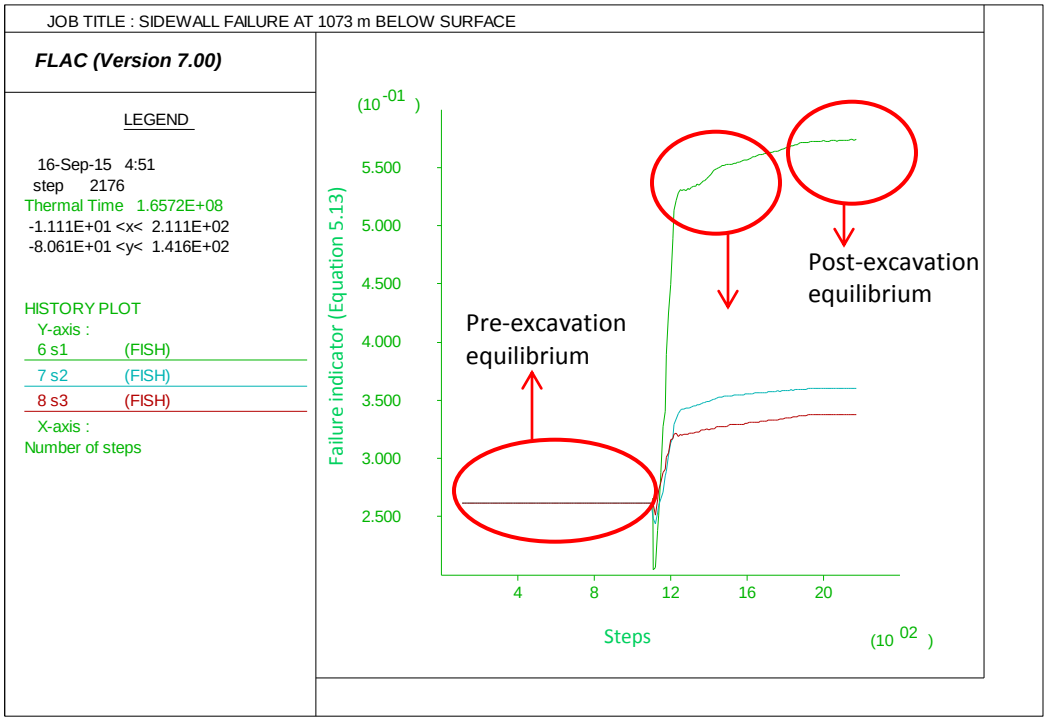


Figure 5.38: Sidewall failure indicator at 1073 m below surface

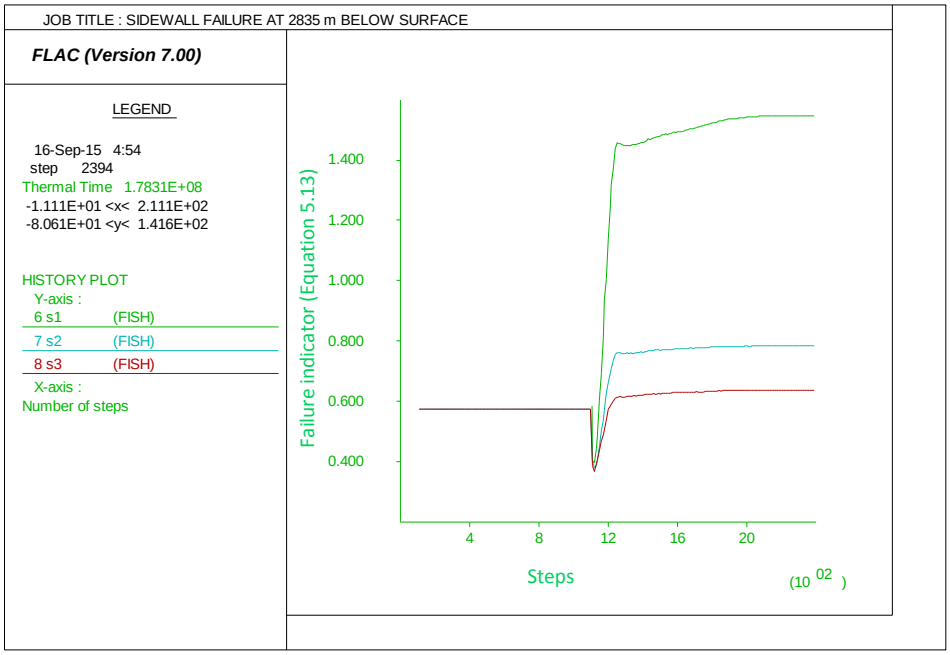


Figure 5.39: Sidewall failure indicator at 2835 m below surface

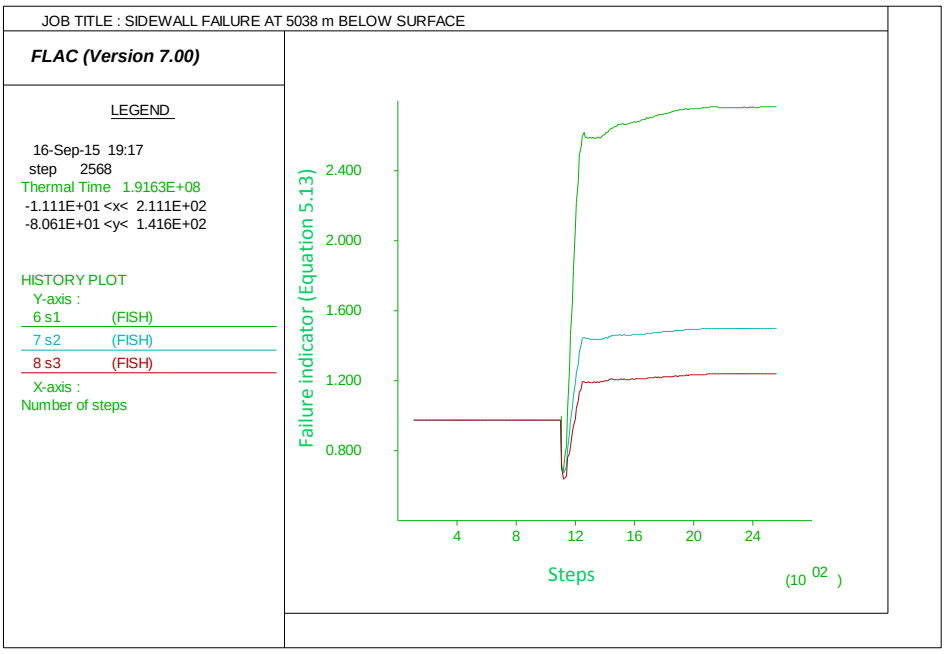


Figure 5.40: Sidewall failure indicator at 5038 m below surface

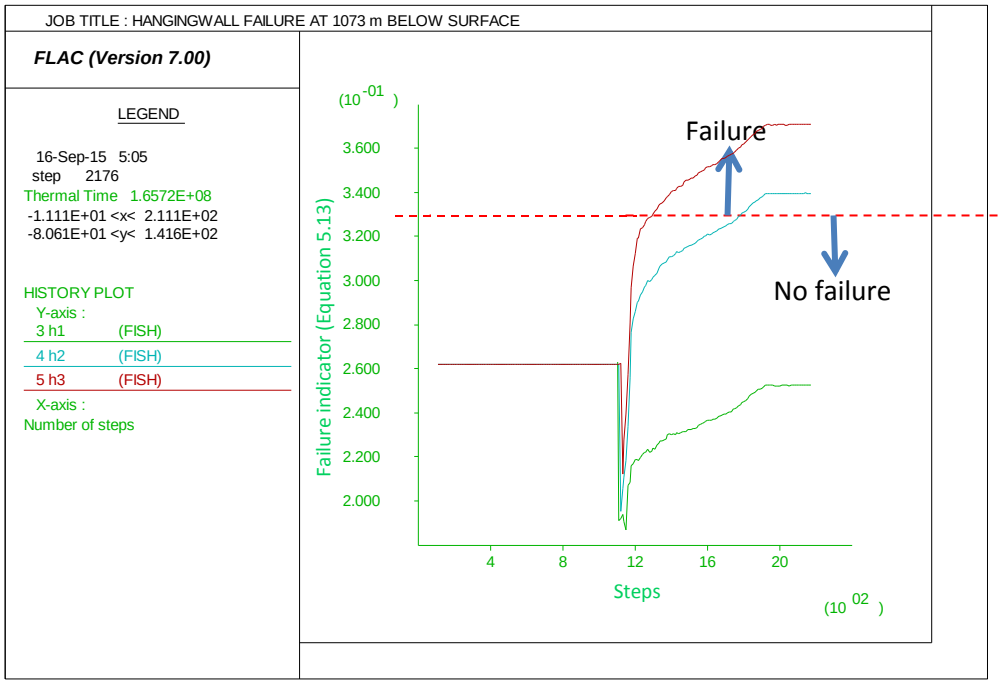


Figure 5.41: Hangingwall failure indicator at 1073 m below surface

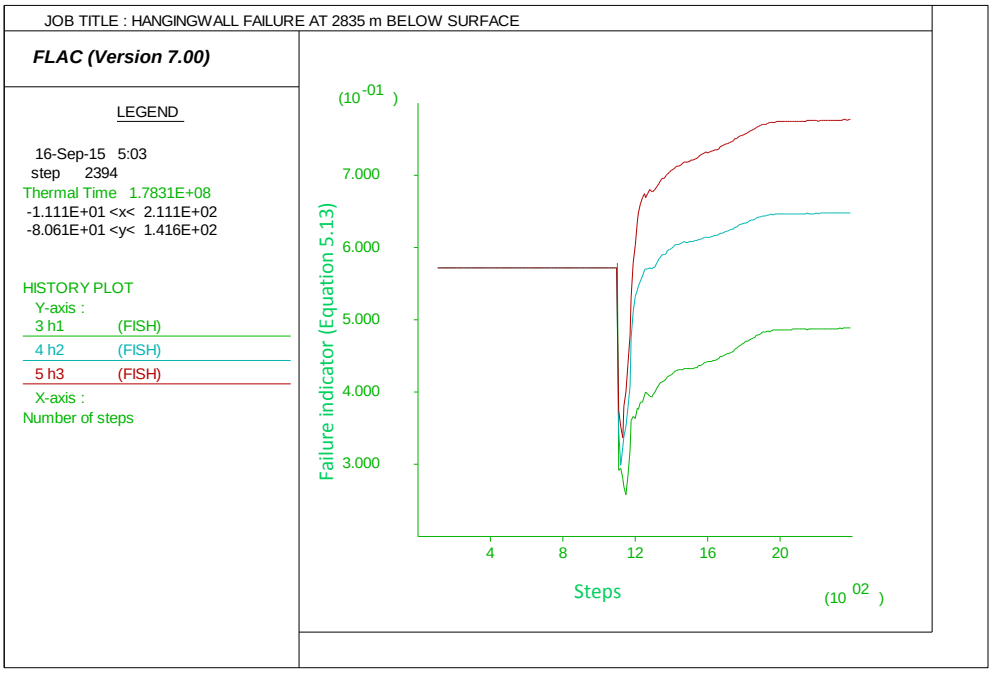


Figure 5.42: Hangingwall failure indicator at 2835 m below surface

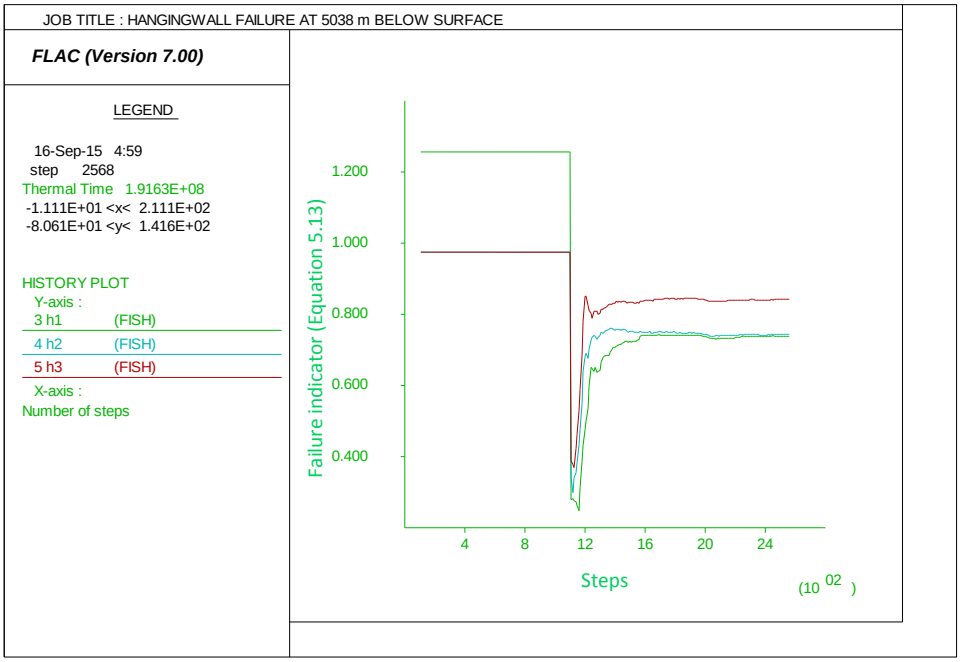


Figure 5.43: Hangingwall failure indicator at 5038 m below surface

5.4 Discussion

Underground workings are constructed in stressed rock and any excavation causes changes in the state of virgin stresses. In order to determine the stability in competent rocks, the knowledge of stress concentration around the opening is important. Stresses around openings may reach the limit according to the failure criterion used that would result in further closure. Evaluation of stresses and displacements around such openings will then be a useful basis for engineering design and support (Malan and Basson, 1998; Pérez and Nordlund, 2012).

Nyungu and Stacey (2014) observed that, at shallow depth in the BIC, rock failure might be unexpected in underground openings because of the competence of rocks and relatively lower in-situ stress levels in comparison to the UCS of the rocks. Nyungu and Stacey (2014), however, stated that fractures have been observed in the

walls of excavations where the stress levels are well below the UCS. They further asserted that stress-induced failure can occur when the post-excavation stresses are as low as one quarter to one half of the rock strength.

Figure 5.45 shows the induced stresses at 1073 m, 2835 m and 5038 m below surface. As can be seen from the state plots (Figures 5.28 to 5.30) and failure indicator plots (Figures 5.38 to 5.43), increases in the in-situ stress and temperature with increasing depth lead to higher magnitude of failure except that there are more tensile failure than shear failure at 5038 m below surface. At 1073 m below surface, using equation 5.12, the criterion proposed by Martin et al (1999), the hangingwall failure indicator values at h1, h2 and h3 are less than 0.33, which implies that there is no failure on the hangingwalls. However, for the sidewall points at s1, s2 and s3, the failure indicators from equation 5.6 are greater than 0.33.

At the depth of 2835 m, there is more failure as shown in the state plot (Figure 5.29) and failure indicator plots (Figures 5.39, 5.42 and 5.44). As observed in Figure 5.44, hangingwall and sidewall failure indicators are higher at depth of 2835 m than 1037 m. The state plot shows that, in addition to shear failure, tensile failure will also be experienced at 2835 m below surface. It is possible that the tensile failure is not only the result of increased in-situ stresses but also temperature. Volumetric expansion of the rocks takes place when the rock temperature increases. This expansion is a function of the thermal cracks induced by the heat energy (thermal stress). These thermal cracks were also observed in the microscopic analyses of the heated rocks that are cooled and viewed under the microscope. The generation of thermal cracks are also possible before the immediate walls of excavation are cooled through ventilation. The values of the failure indicators are well above 0.33 for both the hangingwall and the sidewall as shown in Figures 5.40 and 5.43. Unlike the case with the excavation at 1073 m, the ones at 2835 m would require more conservative support.

The observations from the previous two cases, at 1073 m and 2835 m render the analysis at depth of 5038 m to be more critical. Although, there is reduction in the observed shear failure from the state plot (Figure 5.30) as compared to that of 2835, however, the extent of the horizontal, vertical displacement and tensile failures are higher due to the increase in temperature and in-situ stresses. Kaiser and Kim (2008) affirmed that brittle, tensile rather than shear, failure modes play a role at intermediate to high stress levels and in massive to moderately jointed rock mass. Apart from the contribution of high in-situ stresses to tensile failure at 5038 m, increased temperature also plays an important role as will be shown in the sensitivity analyses.

The horizontal and vertical convergences are 35.8 mm and 62.9 mm respectively at 5038 m below surface. In comparison with the previous depths, stoping at 5038 m below surface has highest vertical convergence has higher values, which implies that roof sagging and floor heave will be more experienced than the relative movement of the sidewall. Based on the magnitude of convergence that will be experienced at ultra-deep mining levels (3500 m to 5000 m), it is recommended that access development be located in the more competent strata, such as in mottled anorthosite with an average UCS of 82 MPa. In addition, the use of yielding rock bolts, which allow significant deformation without failure, would be necessary. Furthermore, longitudinal compression slots can be included in shotcrete to prevent a build-up of load in the lining that would lead to failure. Malan and Basson (1998) also suggested the use of flexible membrane support such as Everbond. They explained that a flexible membrane provides broken rocks with an increased residual strength, even when subjected to large deformations.

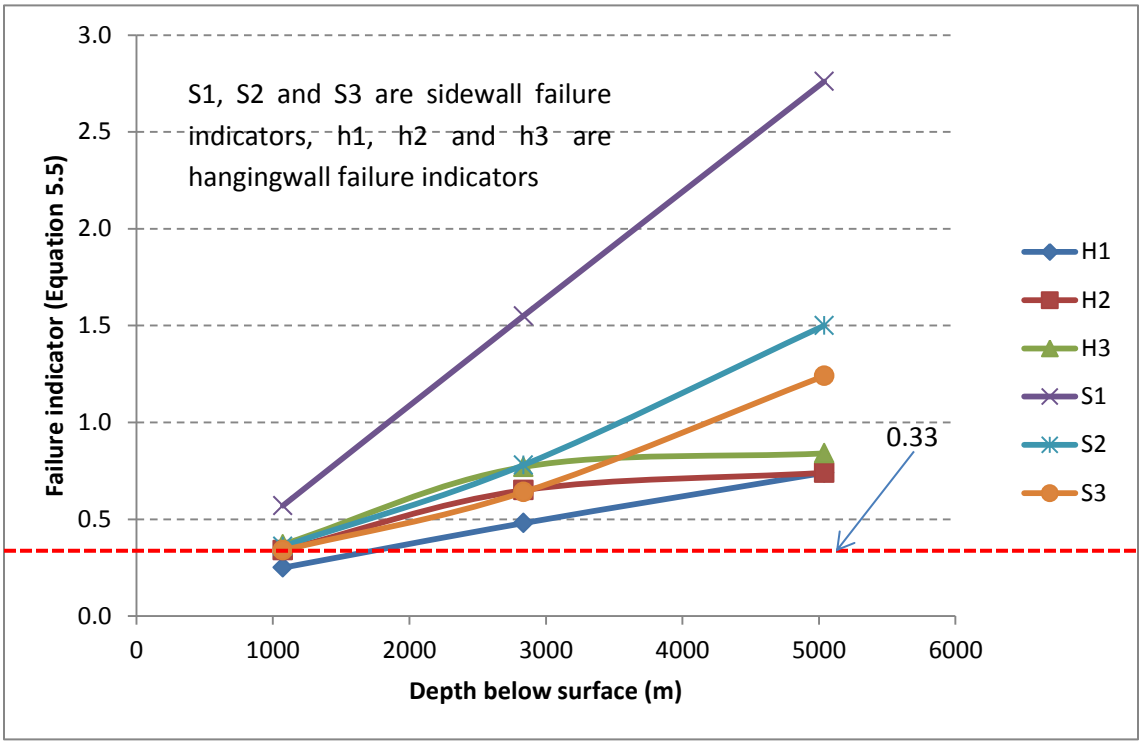


Figure 5.44: Comparison of sidewall and hangingwall failure indicators at different depths

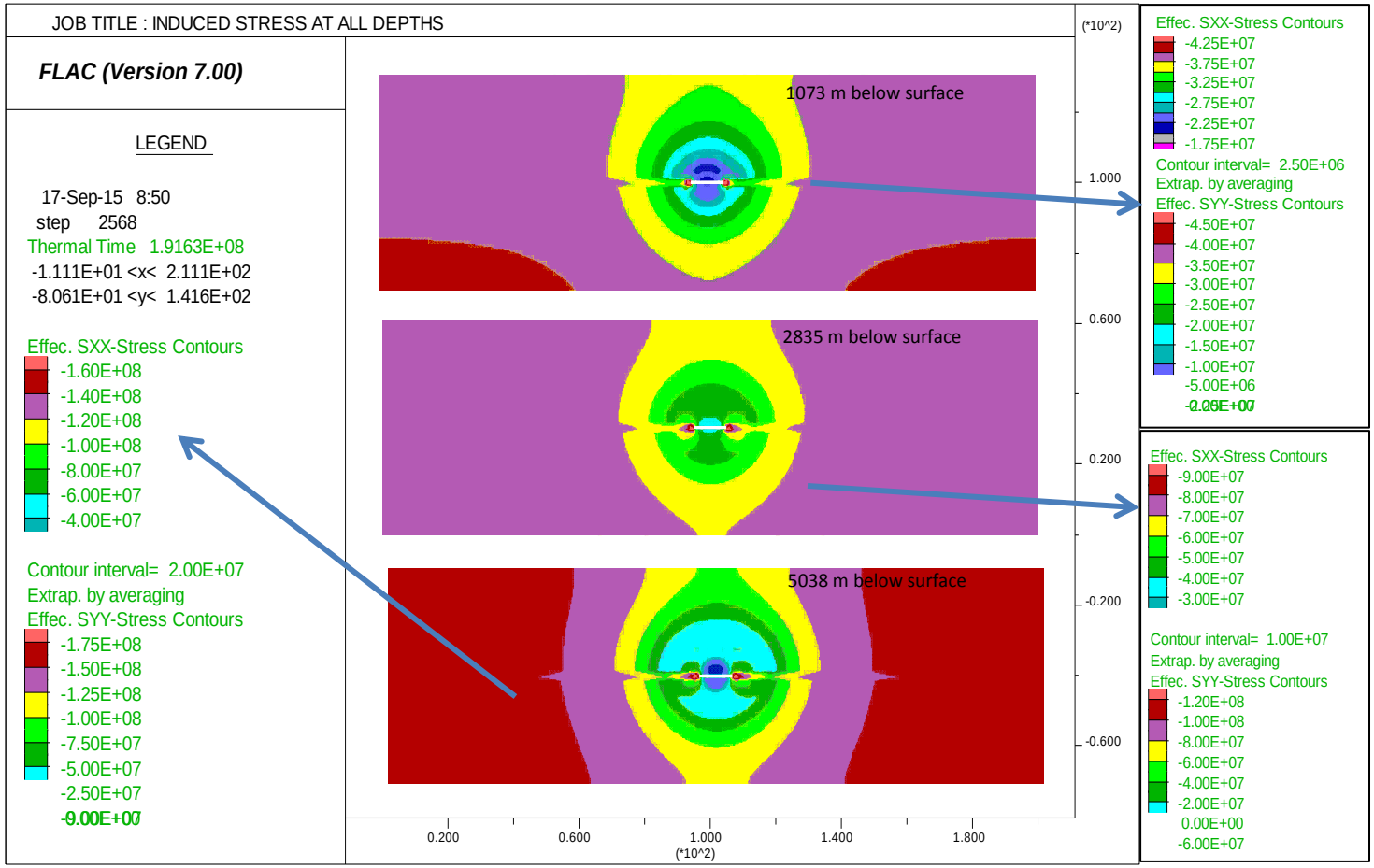


Figure 5.45: Plots of induced stresses at all depths

5.5 Sensitivity analysis

Sensitivity analyses were done to evaluate the influence of temperature increase on the failure. This was achieved by assigning the temperature and thermal properties (coefficient of expansion, thermal conductivity and heat capacity) at depth of 1073 m to that of 5038 m and vice versa. The modelling geometry and the remaining parameters were kept the same. The temperature is increased from 50ºC to 140ºC at 1073 m and reduced from 140ºC to 50ºC at 5038 m. Depth of 1073 m and 5038 m were chosen for comparison since they are at the far ends on the depth scale. Figures 5.46 to 5.49 show the state plots, while Table 5.14 presents the horizontal and vertical displacements for comparison.

Figure 5.47 shows reduction in both the extent of shear and tensile failure in comparison with Figure 5.46 for 5038 m below surface. In reality, this reduction is due to decreasing temperature. However, as observed in Table 5.14, reduction of temperature increased the horizontal and vertical convergence from 36 mm and 63 mm to 43 mm and 90.4 mm respectively. In the case of 1073 m below surface, increasing the temperature from 50ºC to 140ºC increased the extent of shear and tensile failure and convergence as shown in Figures 5.48 and 5.49, and Table 5.14.

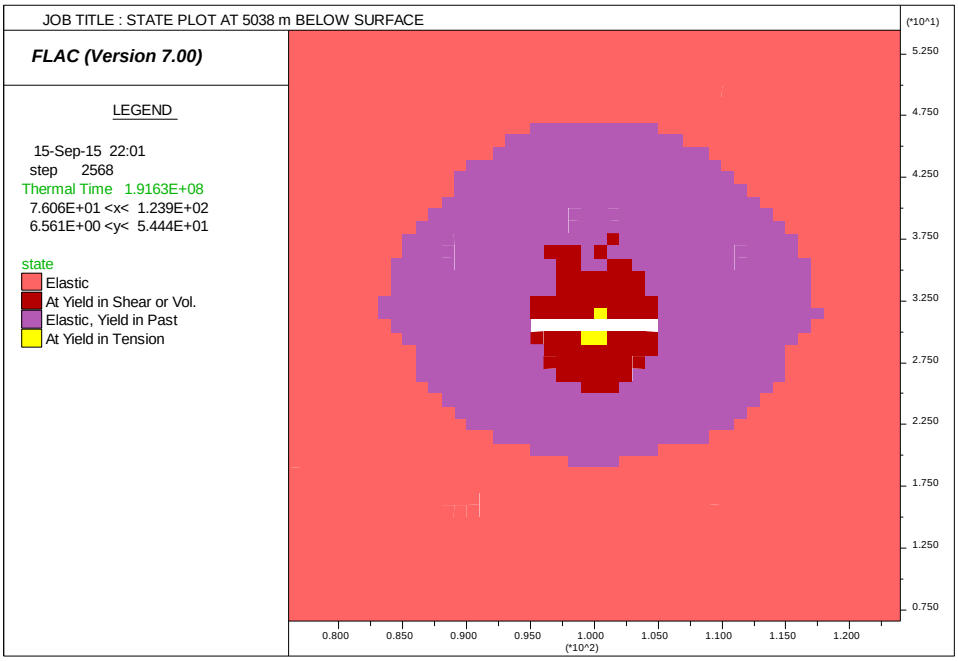


Figure 5.46: State plot for temperature 140ºC at 5038 m below surface

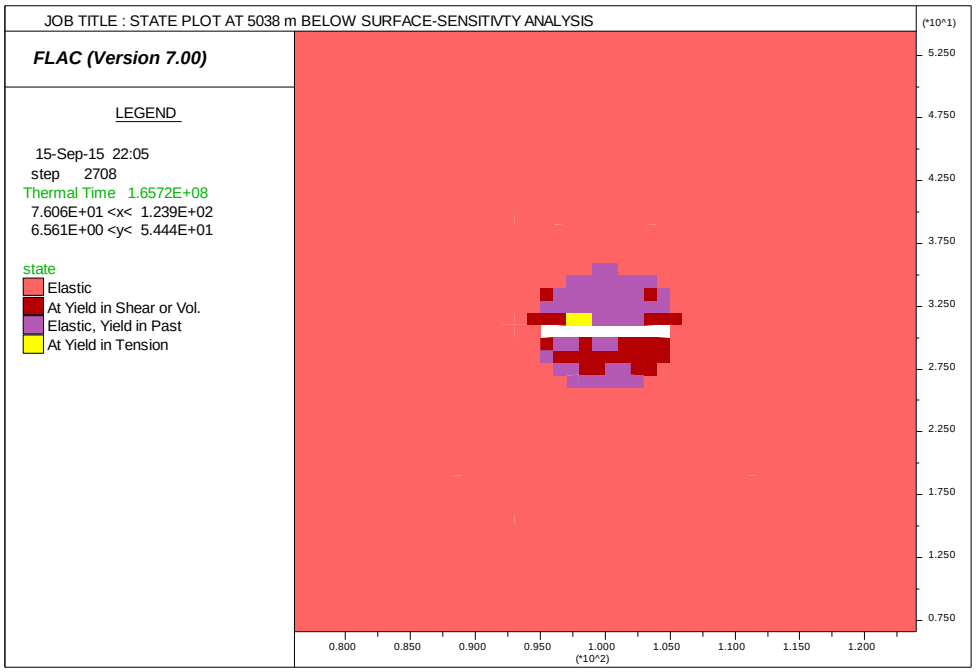


Figure 5.47: State plot for temperature 50ºC at 5038 m below surface

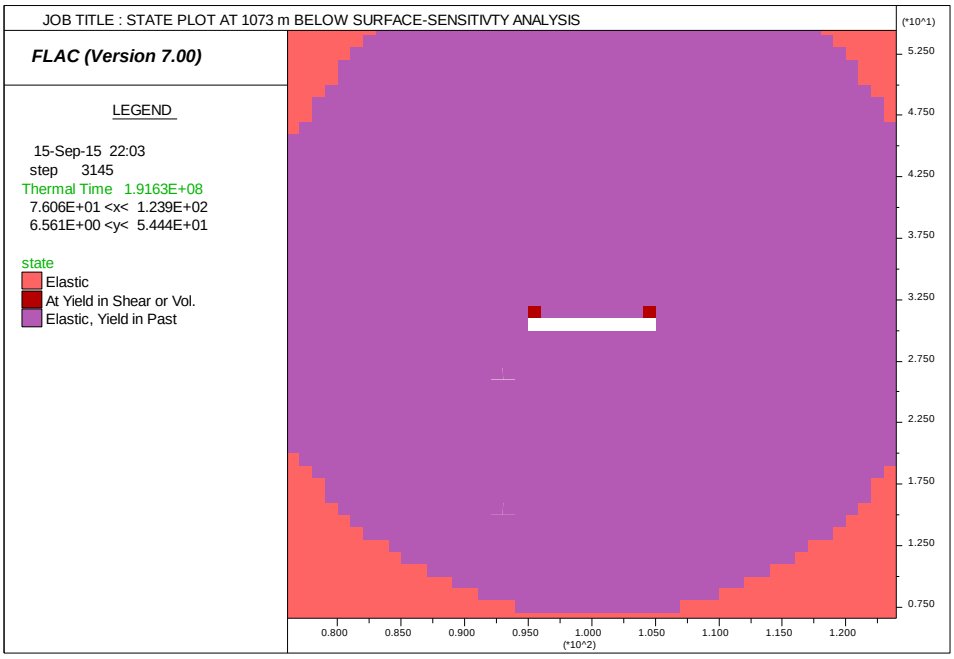


Figure 5.48: State plot for temperature 140ºC at 1073 m below surface

Table 5.14: horizontal and vertical displacements-sensitivity analyses

	50ºC	**140ºC**	**50ºC**	**140ºC**
	Horizontal convergence (mm)		**Vertical convergence (mm)**	
1073 m	2.0	2.5	1.5	2.3
5038 m	43.0	36.0	90.4	63.0

5.6 Modelling of Circular Excavation

The essence of modelling circular opening is to observe the effect of stress and temperature distribution around it. This will be useful in situations where circular excavation are made for thermal or waste repository or other underground storage facilities and transportation routes. Figure 5.49 shows the model set up. A block of 100 m by 100 m was generated, with a mark of a circular tunnel of diameter 10 m to be excavated at its centre (Figure 5.49).



Figure 5.49: Model set up for circular opening

It should be noted that all the modelling parameters used are the same with that of the stope, earlier presented in Tables 5.9, 5.11 and 5.12.

As observed in the temperature plot (Figure 5.50), immediately after excavation, the cool air from ventilation is well distributed around the wall of the opening at 1073 m below surface, even up to 5038 m below surface (Figure 5.57), which caused evenness of the cooling effect. The effective stresses after excavation at depths 1073 m, 2835 m and 5038 m below surface are given in Figures 5.51, 5.52 and 5.53 respectively. In comparison with Figure 5.45, which shows plots of induced stresses for rectangular (stope) excavation, the induced stresses for the circular (tunnel) excavation are evenly distributed. The circular excavation has no edges that allow for stress concentration.

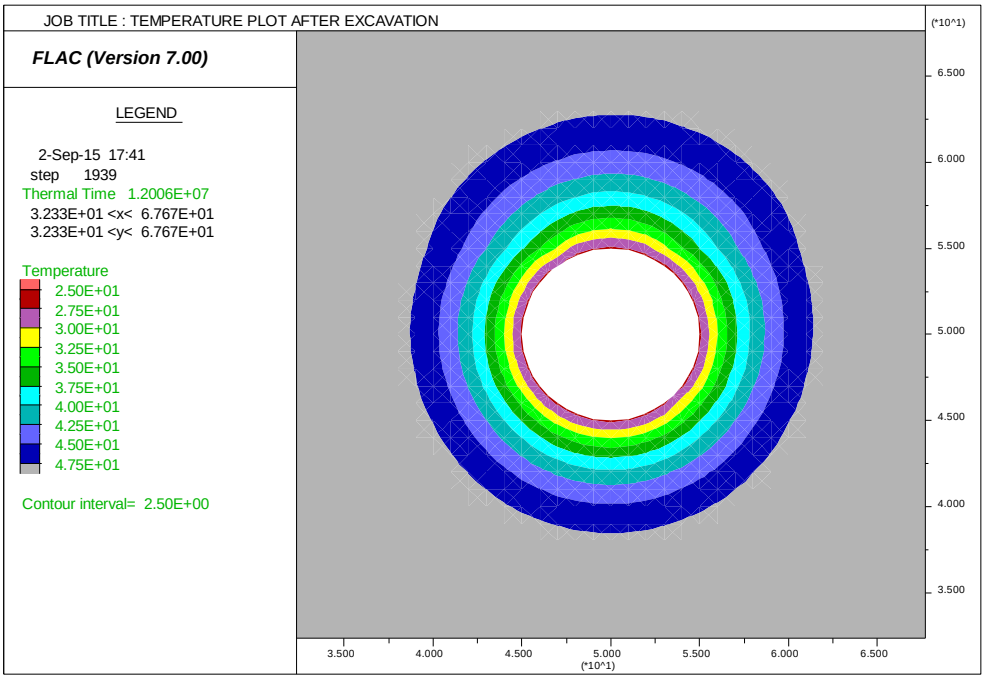


Figure 5.50: Temperature plot for the stope at 1073 m below surface.

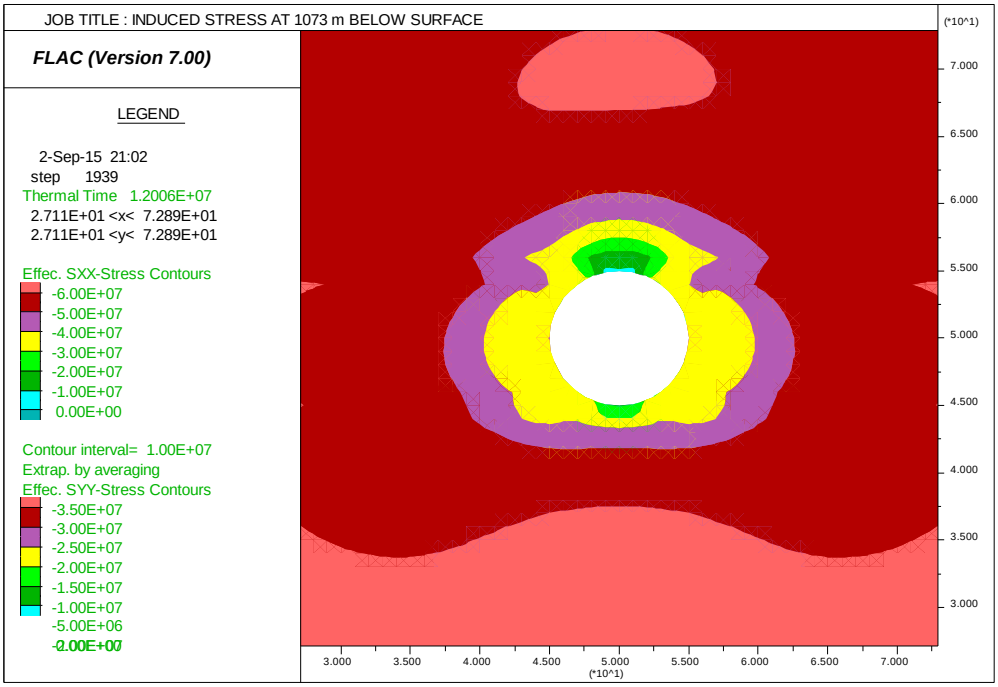


Figure 5.51: Plot of induced stresses at 1073 m below surface

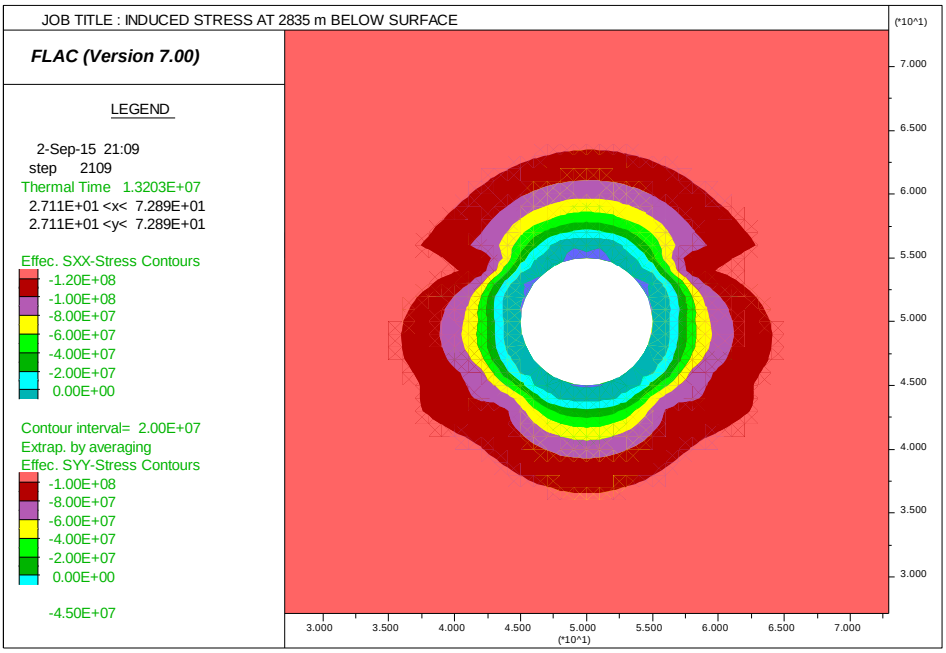


Figure 5.52: Plot of induced stresses at 2835 m below surface

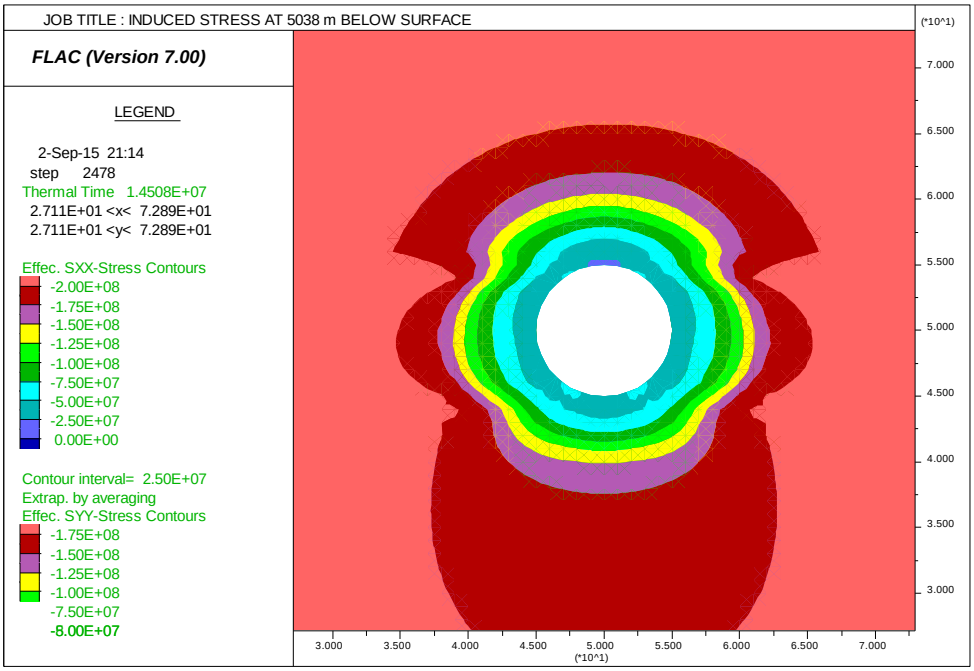


Figure 5.53: Plot of induced stresses at 5038 m below surface

The state plots of the model for excavations at 1073, 2835 and 5038 m below surface are given in Figures 5.54 to 5.56. In comparison with the rectangular excavation, stress relaxation around the circular opening is evenly distributed, that is why tensile failure is not witnessed from shallow-depth to ultra-depth levels, although there is shear failure. In addition, squeezing is also not observed with circular excavation.

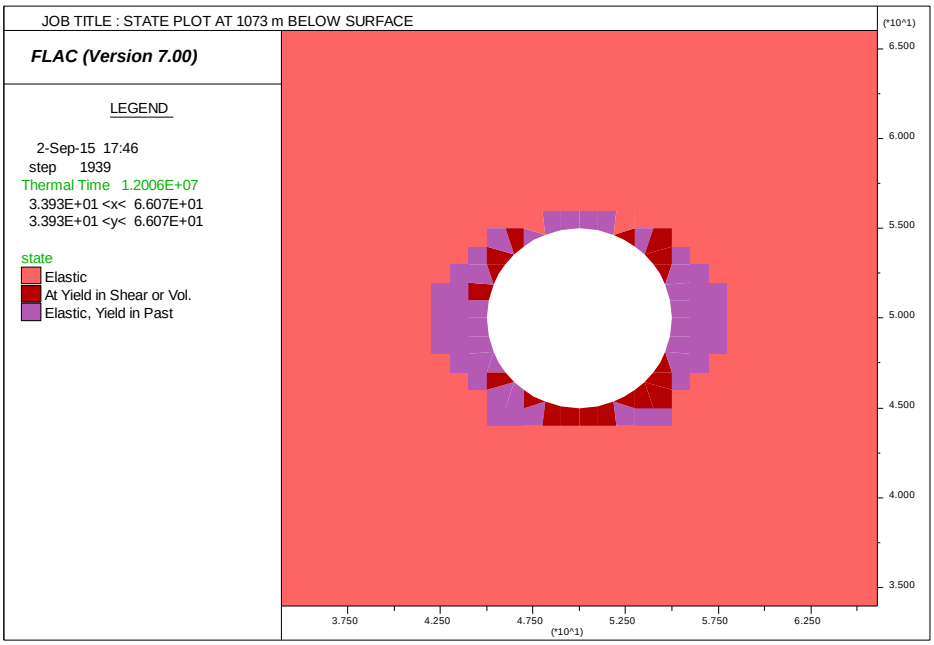


Figure 5.54: State plot at 1073 m below surface

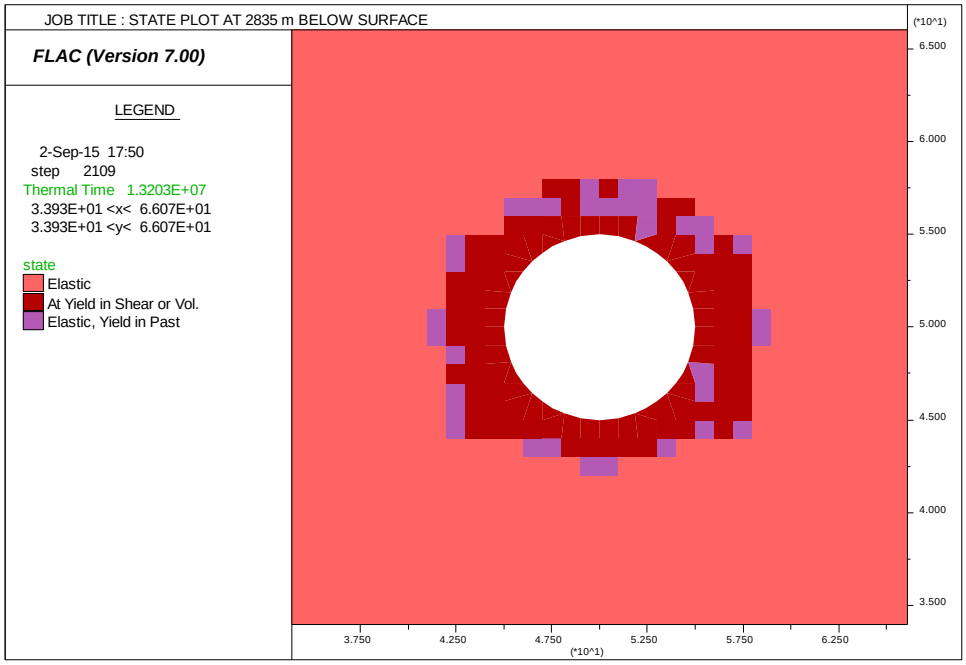


Figure 5.55: State plot at 2835 m below surface

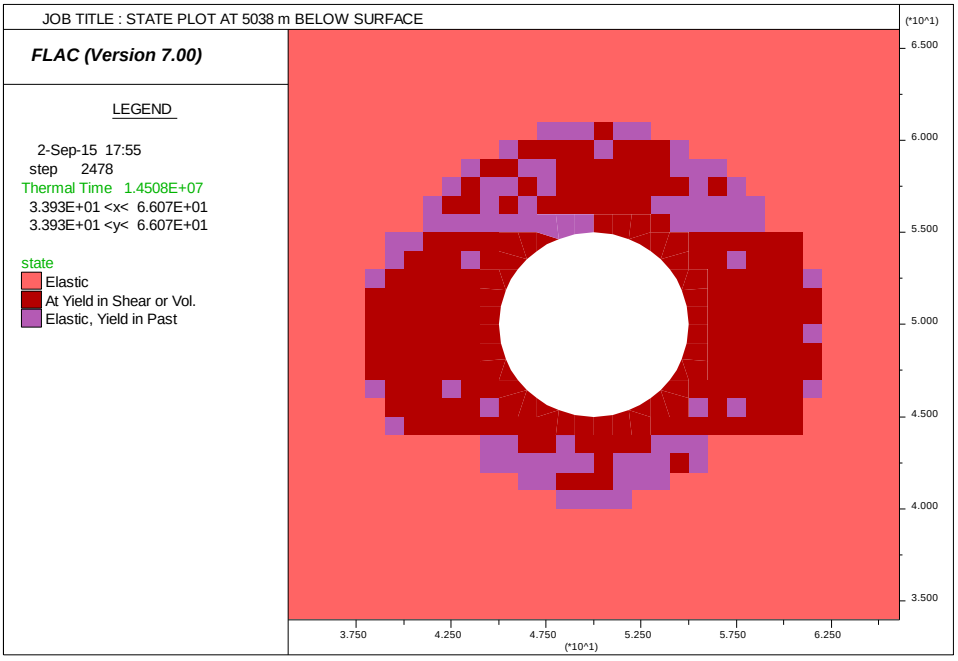


Figure 5.56: State plot at 5038 m below surface

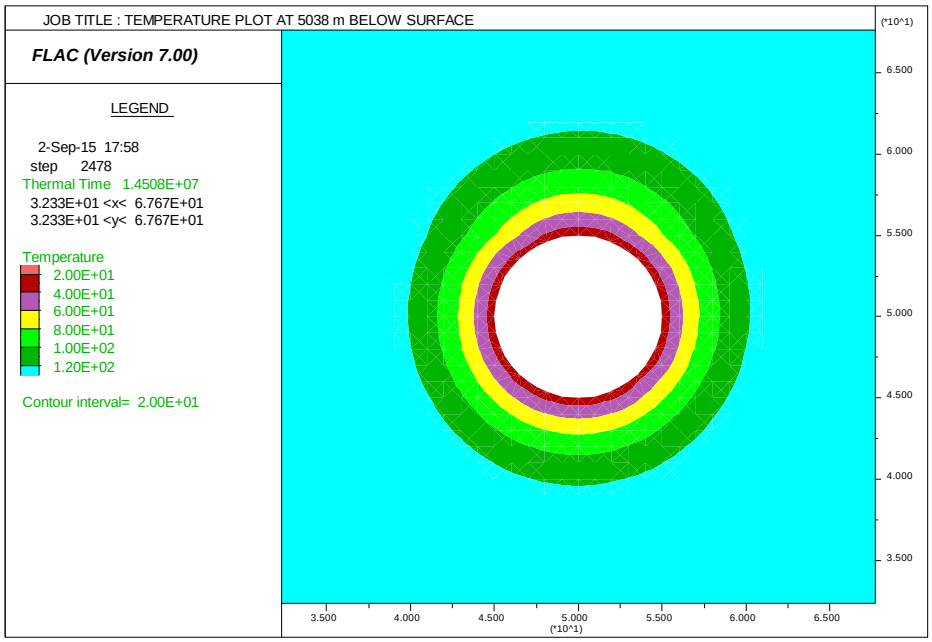


Figure 5.57: Post-excavation temperature at 5038 m below surface

5.7 Sensitivity analysis

Sensitivity analyses were done to evaluate the contributions of temperature and in-situ stresses on failure around the circular excavation. As described in section 5.5, other parameters were kept constant, only temperature and stress were varied. When the temperature (50ºC) and thermal properties of 1073 m below surface was assigned to 5038 m, there was remarkable reduction in the failure extent as shown in Figures 5.58 and 5.59. This implies that temperature has significant contribution to failure with increasing mining depth. However, when the temperature (140ºC) and thermal properties of 5038 m was assigned to 1073 m below surface, the observation from the model is increased elastic, yield in past. There is no increase in shear failure. The explanation that can be advanced for this observation is that temperature range considered in this research cannot initiate failure. However, once in-situ stress increases, the contribution of thermal stress to failure also increases. Therefore, it can be concluded that temperature may not have significant contribution to failure at shallow depth. The effect increases with increasing depth of mining.

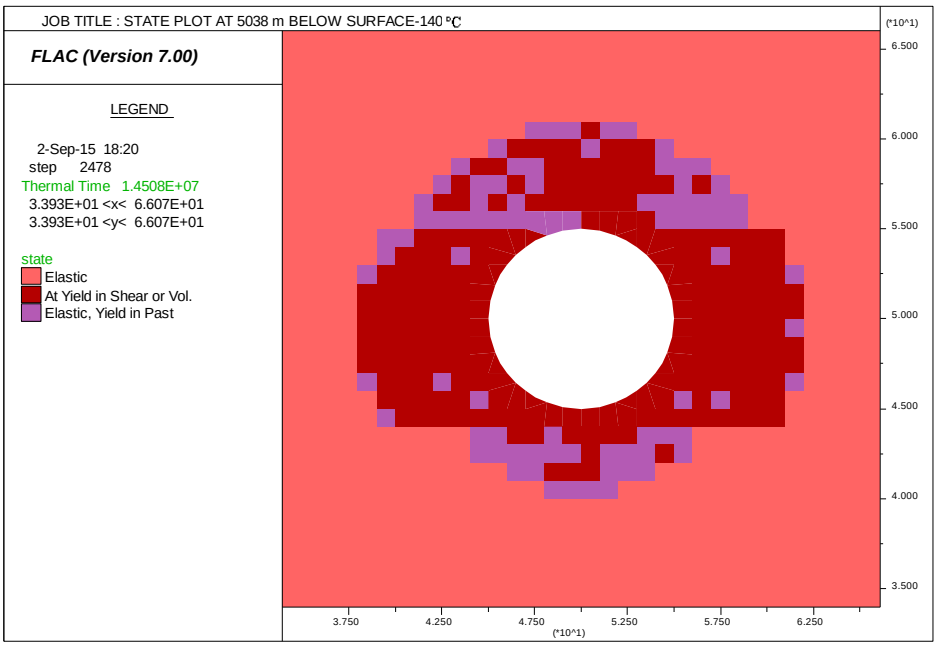


Figure 5.58: State plot for temperature 140ºC at 5038 m below surface

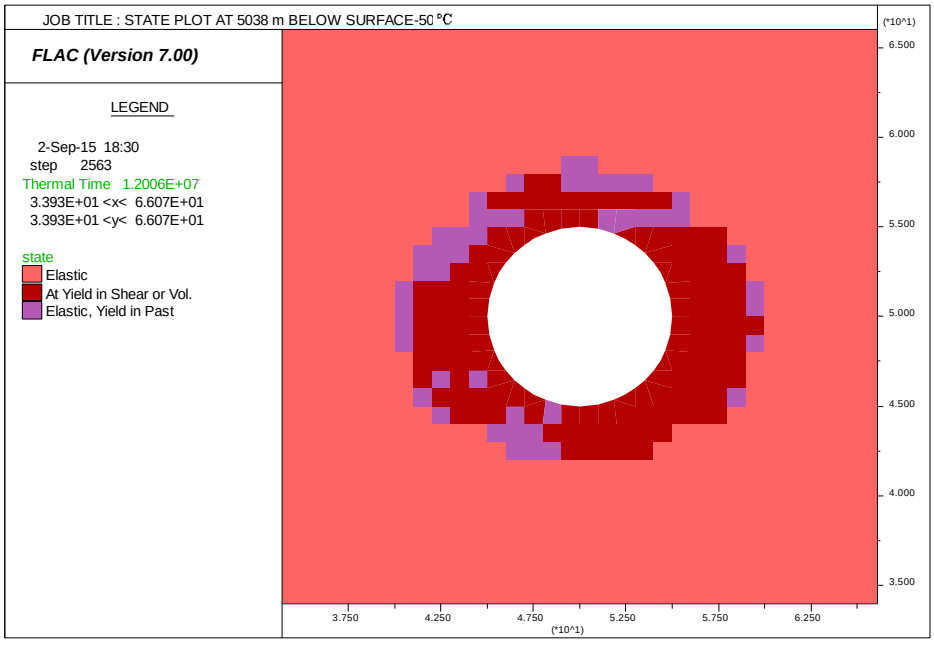


Figure 5.59: State plot for temperature 50ºC at 5038 m below surface

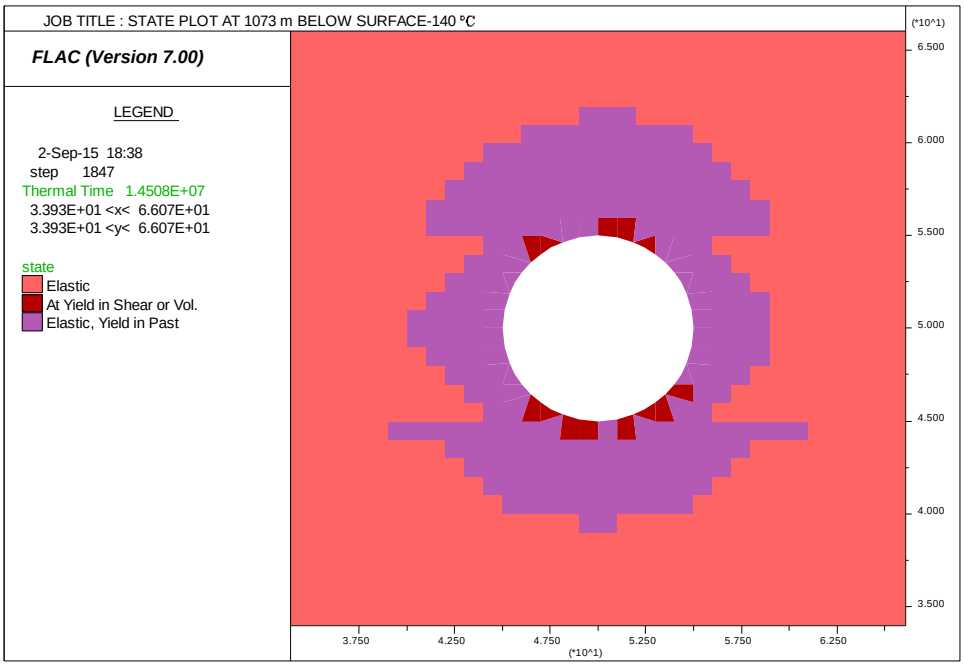


Figure 5.60: State plot for temperature 140ºC at 1073 m below surface

5.8 Chapter summary

This chapter presents the numerical modelling of laboratory rock testing under the influence of confining pressure and temperature. It is observed that higher temperature increased tensile failure in the modelled specimens due to generation and coalescence of microcracks, while higher confining pressure retards crack growth. In the case of underground excavation modelling, tensile failure was observed to increase with increasing mining depth. The sensitivity analyses show that failure of rocks, especially in the BIC, with increasing depth is a function of both increasing in-situ stresses and higher temperatures. With modelling of circular excavation, in comparison with the rectangular excavation, stress relaxation around the circular opening is evenly distributed, that is why tensile failure is not witnessed from shallow-depth to ultra-depth levels, although there is shear failure.

CHAPTER SIX

6.0 CONCLUSIONS AND RECOMMENDATIONS

6.1 Conclusions

The research reported in this thesis contributes to the future of mining, especially in the South African platinum mines and other mines located in high geothermal gradients. The major finding of the research is that it has identified the potential rock engineering challenges that platinum mines in the BIC will face with increasing depth of mining. The various laboratory tests carried out on the BIC rocks provide additional database to the previously available data, particularly on the post-peak behaviour of brittle hard rocks. Recommendations of the required support systems for safe mining were also given.

- From the literature reviewed, there is no report of any research, which looked into the effect of increasing temperature on the behavior of rocks with respect to depth of mining in South African deep mines.

- In laboratory testing, the general trend observed was the reduction in strength and Young's modulus of BIC rocks with increasing temperature. This could be attributed to the breaking of the bonds within the rock minerals, which results from increasing thermal energy.

- Temperature does not have influence on the Poisson's ratio of the BIC rocks due to the increase of the dimensions of the rocks in all directions on a similar ratio. Similar observations have been reported from literature in Chapter 2.

- Based on the regression analyses done on the strength-reduction and Young's modulus, with increasing temperature, two equations were developed. These equations will be useful means in determining strength and Young's modulus reduction as a function of temperature, which

contributes as input data for numerical modelling and better underground rock engineering design.

- Another important observation is the increase in the volumetric expansion (dilatancy) of the rocks with increasing temperature under triaxial testing. Rock dilatancy angle is an important parameter for numerical modelling in that it provides the knowledge of mine collapse and mining-induced rock bursts. As stated in the literature review, spalling and slabbing are the prevalent failure mode around underground excavations in hard brittle rocks where there are high in-situ stresses. Rock mass dilation will have its highest value close to the boundary and relaxes away from the excavation due to higher confining stress. This study provides the values of dilation angles for the BIC rocks and its variation with temperature was also indicated.

- Increasing temperature gives rise to increase in dilatancy at pre-peak, post peak and residual stage of rock deformation. As reported in the literature, the values of the pre-peak dilation angles are relatively smaller when compared with that of post-peak and residual ones. This is because at pre-peak stage, there are fewer cracks and not all the cracks are interlinked, while at peak and post-peak stage, there are more cracks as a result of the applied load and heat energy. These load and heat energy resulted in the weakening of the bonds within the grains of the rock samples which caused higher volumetric expansion.

- All the samples tested show reduction in friction angles and cohesion with increasing temperature. There is approximately 13 to 16 % increase in the magnitude of the friction angle between pyroxenite and mottled anorthosite, however, the increase seems to be rock type dependent.

- The coefficient of thermal expansion of the rocks was measured under unconfined and confined conditions. In both cases, the coefficient of thermal expansion increased with temperature increase.

- Ultrasonic testing was carried out on the BIC samples, at different temperatures and applied forces. Expansion caused by heating generates microcracks which serve as obstacles for the travelling waves, thereby increasing the wave travel time. The results of ultrasonic testing strengthen the fact that heat energy contributes to tensile failure of rocks. The ultrasonic velocities were measured while the rocks were loaded under a compression-testing machine at ambient temperature. The results showed increasing P and S wave velocities with increasing load.

- The result of the optical microscope analyses showed that there are some physical changes observed on the rocks subjected to heat treatment but the observed changes are negligible. The scanning electron microscope images revealed that the crack initiation starts at lower temperature and extends with increasing temperature. The chemical analyses of the samples subjected to different temperatures showed that the temperature range considered for this research is not high enough to induce significant chemical changes in the samples. Although there may not be substantial changes in the physical and chemical properties of the rocks in the wall of underground excavations, however, crack formation, which results from combination of stress-temperature effects, will contribute to failure, particularly at ultra-deep mining level.

- The FLAC 2D modelling results showed that the extent of tensile failure increases with increasing temperature. In addition to this general observation, tensile failure is observed more with norite than chromitite. The possible reason for this is that norite is more brittle and has higher coefficient of thermal expansion than chromitite. Increases in the in-situ stress and temperature cause higher magnitude of shear and tensile failures around the excavation as depth increases. Few tensile and shear failures were observed at depth of 1073m, while at 2835m, failure increases tremendously. Depth of 5038m is characterised mainly with tensile failure and not with few shear failure due to high temperature and in-situ stresses.

Vertical and horizontal stope displacements increased as mining depth increased.

- The result of the sensitivity analyses showed reduction in shear, tensile failures and convergence at the walls of the excavation with reduction in temperature while keeping the in-situ stress constant. Although, temperature variation has a role in micro-scale rock fracturing, in-situ stresses is the major contributor to deformation as mining depth increases.

6.2 Recommendations for future research

The following recommendations are made for future research:

- Since not all the rocks from the BIC were available for testing in this research, it is recommended that the remaining lithology, such as, Merensky reef, harzburgite, granofel, magnetite are also included in the testing programme. This will ensure having a complete database on the thermo-mechanical behaviour of the BIC rocks. In addition, the diameter of most of the tested rocks were 36 mm, it is suggested that further tests are done with larger diameter specimens to assess any size influence.

- The laboratory testing of the BIC rocks under varied temperatures did not fully represent the actual conditions rocks are subjected to underground. In reality, the skin of the excavation is cooled by ventilation, while the inner part remains warmer causing temperature variation within a short distance. A full laboratory simulation of the effect of this temperature variation on rock behaviour could be attempted in future research.

- The loading of rocks were done under static condition, the response of rocks to dynamic loading and creep test, with respect to temperature variation is another area for further research.

- The numerical modelling aspect of the research covered two dimensions. It is recommended that three-dimensional modelling is done in order to observe the

extent of failure in three dimensions. The numerical modelling only considered the UG2 reef, since there is no adequate information on the material properties of the Merensky reef, with respect to temperature variation. Modelling of the Merensky reef is necessary, to have a holistic view of the behaviour of the underground working across the BIC. In addition, modelling of the Class II behaviour of rocks observed in the laboratory, was not possible with FLAC 2D. The FLAC 2D programmers are advised to add features that will enable modelling Class II behaviour.

- In order to understand the extent of rock surface cooling by ventilation, it is suggested that direct temperature measurements are done from excavation skin to the interior of the rock through drill holes.

- Extension of this research to mines located in other high geothermal zones, worldwide is recommended.

REFERENCES

Alejano L.R.and Alonso E. (2005): Considerations of the dilatancy angle in rocks and rock masses, *Int. J. Rock Mech. Min. Sci.*, Vol. 42 pp. 481–507.

Al-Harthi A.A, Al-Amri R.M and Shehata W.M. (1999): The Porosity and Engineering Properties of Vesicular Basalt in Saudi Arabia. *Eng. Geol*. Vol. 54, issue 3 -4, pp. 313 – 320.

Altindag R. (2012): Correlation between P-wave velocity and some mechanical properties for sedimentary rocks. Industry. *The Journal of the South African Institute of Mining and Metallurgy*. Vol. 112, pp. 229-237.

Araujo R. G. S., Sousa J. L. A. O. and Bloch M. (1997): Experimental Investigation on the Influence of Temperature on the Mechanical Properties of Reservoir. *Int. J. Rock Mech. Min. Sci. & Geomech. Abstr*. Vol. 34, No. 2. pp. 1-16.

Aydin A. (2014): Upgraded ISRM Suggested Method for Determining Sound Velocity by Ultrasonic Pulse Transmission Technique, *Rock Mech Rock Eng.* Vol. 47, pp. 255–259.

Azzoni A., Bailo F., Rondena E., and Zaninetti A (1996): Assessment of Texture Coefficient for Different Rock Types and Correlation with Uniaxial Compressive Strength and Rock Weathering. *Technical Notes Rock. Mech. Rock Engng*. Vol. 29 issue 1 pp. 39 – 46.

Battaglia S. Franzini M. and Mango F. (1993): High-Sensitivity Apparatus for Measuring Linear Thermal Expansion: Preliminary Results on the Response of Marbles to Thermal Cycles. *Il Nuovo Cimento* Vol. 16 C, No. 4, pp 453-461.

Bery A. A., and Saad R. (2012): Correlation of Seismic P-Wave Velocities with Engineering Parameters (N Value and Rock Quality) for Tropical Environmental Study. *International Journal of Geosciences*, Vol. 3, pp. 749-757.

Bian, Y. Jia, Armand G., Duveau G. and Shao J.F. (2012): 3D numerical modeling thermo-hydromechanical behaviour of underground storages in clay rock. *Tunnelling and Underground Space Technology*, Vol. 30, pp. 93–109.

Biffi M., Stanton D., Rose H. and Pienaar D. (2007): Ventilation Strategies to Meet Future Needs of the South African Platinum Industry. *The Journal of the South African Institute of Mining and Metallurgy*. Vol. 107 pp. 59-66.

Brady B.H.G. and Brown E.T. (2004): Rock Mechanics for underground mining, 3rd edition, 628 p. Dordrecht: Kluwer.

Brake D.J. and Bates G.P. (2000): An interventional study. In: *Proceedings of the International Conference on Physiological and Cognitive Performance in Extreme Environments*, pp. 170-172. W.M.Lau, (Ed.) Defence Scientific and Technology Organisation, Australian Department of Defence, Canberra.

Brotón V., Tomás R., Ivorra S. and Alarcón J. C. (2013): Temperature influence on the mechanical properties of a porous rock: San Julian's calcarenite. *Engineering Geology* Vol 167 pp. 117-127.

Budavari S. (1983): Response of the rock mass to excavations underground, Rock Mech. in Mining Practice, *S. Afr. Inst. Min. Metall., Monograph Series*, vol. 5, pp. 55–76.

Cai M. (2008): Influence of intermediate principal stress on rock fracturing and strength near excavation boundaries-insight from numerical modeling *International Journal of Rock Mechanics & Mining Science.* 45(5), 763–72.

Cai M. and Zhao X.G. (2010): A confinement and deformation dependent dilation angle model for rocks. *44th U.S. Rock Mechanics Symposium and 5th U.S.-Canada Rock Mechanics Symposium*, held in Salt Lake City, UT, June 27-30, 2010.

Cai M., Kaiser P.K., and Martin C.D. (2001). Quantification of rock mass damage in underground excavations from microseismic event monitoring. *International Journal of Rock Mechanics & Mining Science.* 38(8), 1135–45.

Castro L.A.M., Bewick R.P. and Carter T.G. (2012): An overview of numerical modelling applied to deep mining. In: *Innovative Numerical Modelling in Geomechanics*, Rebeiro e Sousa et al (eds) pp. 393-414.

Cawthorn R. G. (1999): The Platinum and Palladium Resources of the Bushveld Complex. *South African Journal of Science* Vol. 95 pp. 481-489.

Cawthorn R. G. (2010): The Platinum Group Element Deposits of the Bushveld Complex in South Africa. *Platinum Metal Rev*. Vol. 54 No. 4 pp. 205-215.

Charalampidou. E. M., Hall S. A., Stanchits S., Lewis H. and Viggiani G. (2011): Characterization of shear and compaction bands in a porous sandstone deformed under triaxial compression, *Tectonophysics*. Vol. 503, pp. 8–17.

Clauser C. (2011a): Thermal Storage and Transport Properties of Rocks, I: Heat Capacity and Latent Heat. In: Harsh Gupta (Ed.), *Encyclopedia of Solid Earth Geophysics*, 2nd ed., Springer.

Clauser C. (2011b): Thermal Storage and Transport Properties of Rocks, II: Thermal Conductivity and Diffusivity. In: Harsh Gupta (Ed.), *Encyclopedia of Solid Earth Geophysics*, 2nd ed., Springer.

Clauser C., and Huenges E. (1995): Thermal Conductivity of Rocks and Minerals, in Rock Physics and Phase Relations: *A Handbook of Physical Constants*, AGU Ref. Shelf, Vol.3. Ahrens T. J. (Ed.), pp. 105-126, AGU, Washington D. C.

Cooper H.W. Simmons G. (1977): The effect of cracks on the thermal expansion of rocks. *Earth and Planetary Science Letters* Vol. 36 pp. 404-412.

Donoghue A. M. (2004): Occupational Health Hazards in Mining: An Overview. *Occupational Medicine* (London). Vol. 54 pp. 283-289.

Dunlap M. and Adaskaveg J.E. (1997): Introduction to the Scanning Electron Microscope. Theory, practice, & procedures. *Facility for Advance Instrumentation*. U. C. Davis, p 52

Dwivedi R. D., Goel R. K. Prasad V. V. R. and Sinha A. (2008): Thermo-Mechanical Properties of Indian and other Granites. *Int. Journal of Rock Mech. & Min. Sci*. Vol. 45 pp. 303-315.

Eberhardt E., Stead D., Stimpson B., and Read R.S. (1998): Identifying crack initiation and propagation thresholds in brittle rock. *Can. Geotech. J*. Vol. 35, pp. 222 - 233.

Egerton F.M.G. (2004): Presidential Address: The mechanisation of UG2 mining in the Bushveld Complex, *The Journal of The South African Institute of Mining and Metallurgy*, Vol. 104, No. 8, pp. 439–455.

Finzi Y., Muhlhaus H., Gross L. and Amirbekyan A. (2013): Shear Band Formation in Numerical Simulations Applying a Continuum Damage Rheology Model, *Pure Appl. Geophys*., pp. 13-25.

Fonseka GM, Murrell SAF, Barnes P. (1985): Scanning electron microscope and acoustic emission studies of crack development in rocks. *Int. J. Rock Mech. Min. Sci. Geomech Abstr*. Vol. 22 Issue 5 pp. 273-289.

Fortin J., Stanchits S., Vinciguerra S. and Guéguen Y. (2011): Influence of thermal and mechanical cracks on permeability and elastic wave velocities in a basalt from Mt. Etna volcano subjected to elevated pressure, *Tectonophysics*, Vol. 503 pp. 60–74.

Fuenkajorn K and Kenkhunthod N. (2010): Influence of Loading Rate on Deformability and Compressive Strength of Three Thai Sandstones. *Geotech. Geol. Eng*. Vol 28 pp. 707 – 715.

Fukui K., Okubo S, and Ogawa A. (2004); Some Aspects of Loading-rate dependency of Sanjome Andesite strengths. *Int. J. Rock Mech. And Min Sci*. Vol. 41 pp. 1215 – 1219.

Gomez-Heras, M., Smith, B.J. and Fort, R. (2006): Surface temperature differences between minerals in crystalline rocks: implications for granular

disaggregation of granites through thermal fatigue. *Geomorphology* Vol. 78, pp. 236–249.

Haile, A.T. and Jager, A.J. (1995): Rock mass condition, behaviour and seismicity in mines of the Bushveld igneous complex, SIMRAC Report GAP 027, Department of Mineral and Energy Affairs, South Africa.

Hakami E. and Olofsson S. O. (1999): Thermo-mechanical Effects around a radioactive waste repository. In: *FLAC and Numerical Modelling in Geomechanics*. Detournay C and Hart R (eds). pp 311-316.

Hall K (1999): The Role of Thermal Stress Fatigue in the Breakdown of Rock in Cold Regions. *Geomorphology*, Vol. 31, Issues 1-4. Pp 47-63

Hall K. and Hall A. (1991): Thermal Gradients and Rock Weathering at Low Temperatures: Some Simulation Data. *Permafrost and Periglacial Processes*, Vol. 2, pp. 103-112.

Handley, M.F. (2013): Pre-mining stress model for subsurface excavations in southern Africa. *Journal of the Southern African Institute of Mining and Metallurgy*, vol. 113, no.6. pp. 449-471.

Hartman H. L. Mutmansky J. M. Ramani R. V. and Wang Y. J. (2012): Mine Ventilation and Air Conditioning (3rd Edition). Somerset, NJ, USA: John Wiley & Sons, 752 pp.

He C., Okubo S., and Nishimatsu Y. (1990): A Study on the Class II Behaviour of Rock. *Rock Mechanics and Engineering*. Vol. 23 pp. 261-273.

He, T. and Schmitt D. (2006): P- and S-wave velocity measurements and pressure sensitivity analysis of AVA response, *CSPG-CSEG-CWLS Convention*, Expanded Abstracts, pp. 398–404.

Heuze F. E. (1983): High-temperature Mechanical, Physical and Thermal Properties of Granite Rocks – A Review. *Int. J. Rock Mech. Min. Sci. and Geomech. Abstr*. Vol. 20, No. 1 pp. 3-10.

Hirono T. and Hamada Y. (2010): Specific Heat Capacity and Thermal Diffusivity and their Temperature Dependencies in Rock Sample from Adjacent to the Taiwan Chelungpu Fault, *J. Geophys. Res*., Vol. 115, B05313, 13pp., doi: 10.1029/2009JB006816.

Hoek E. and Brown E.T. (1997): Practical estimates of rock mass strength. *Int. J. Rock Mech. Min. Sci.* 34 8 pp. 1165-86.

Hoek E., Carranza-Torres C. and Corkum B. (2002): Hoek-Brown criterion – 2002 edition. *Proc. NARMS-TAC Conference*, Toronto, pp. 267-273.
Hoek E. and Martin C.D. (2014): Fracture initiation and propagation in intact rock – A review, *Journal of Rock Mechanics and Geotechnical Engineering*, Vol. 6, Issue 4, Pages 287–300.

Holwell D. A. and Mc Donald I (2007): Distribution of Platinum-Group Elements in the Platreef at Overysel, Northern Bushveld Complex: A Combined PGM and LA-ICP-MS Study. *Contrib. Mineral Petrol*. Vol. 154 pp. 171-190.

Homand-Etienne H., and Houpert R. (1989): Thermally Induced Micro-Cracking in Granites: Characterization and Analysis. *Int. J. Rock Mech. Min. Sci. & Geomech. Abstr*. Vol. 26, No. 2 pp125-134.

Horai K. and Baldridge S. (1972): Thermal Conductivity of Nineteen Igneous Rocks, Application of the Needle Probe Method to the Measurement of the Thermal Conductivity of Rocks. *Phys. Earth Planet, Interior*. Vol.5, pp. 151 – 156.

Howarth D.F. and Rowlands, J.C. (1986) Development of an index to Quantity Rock Texture for Qualitative Assessment of Intact Rock Properties. *Geotechnical Testing Journal*. Vol. 9, pp. 169 – 179.

Hudson, J.A., Brown E.T. and Fairhurst C. (1971): Shape of the complete stress-strain curve for rock, Proc. 13th Symposium Rock Mechanics, University of Illinois, Urbana, Illinois.

Huotari T. and Kokkonen I. (2004): Thermal expansion properties of rocks: Literature survey and estimation of thermal expansion coefficient for Olkiluoto mica gneiss. *Working report 2004-04.* Posiva Oy. Olkiluoto, Finland. 68 pp.

ISRM (1978): Suggested methods for determining tensile strength of rock materials. Committee on laboratory tests. *Int. J. Rock. Mech. Min. Sci. & Geomech. Abstr*, Vol. 15, pp. 99–103.

ISRM (1979): Suggested methods for determining the uniaxial compressive strength and deformability of rock materials. Committee on laboratory tests. *Int. J. Rock. Mech. Min. Sci. & Geomech. Abstr*, Vol. 16, pp. 135–140.

ISRM (1983): Suggested method for determining the strength of rock material in triaxial compression: Revised version, *Int. J. Rock. Mech. Min. Sci. & Geomech. Abstr*. Vol. 20, No. 6, pp. 283–290.

ISRM (1999): Draft ISRM suggested method for the complete stress-strain curve for intact rock in uniaxial compression. *Int J Rock Mech Min Sci* Vol. 36, No. 3, pp. 279-289.

Itasca Consulting Group, Inc. (2012): "FLAC (Fast Lagrangian Analysis of Continua) User's Guide (Version 7.0)." Minneapolis, Minnesota: Itasca Consulting Group, Inc.

Jones M.Q.W. (2003): Thermal properties of stratified rocks from Witwatersrand gold- mining areas. *The Journal of the South African Institute of Mining and Metallurgy* (April) 173–185.

Kahraman S., Ulker U., and Delibalta M. S. (2007): A quality classification of building stones from P-wave velocity and its application to stone cutting with gang saws, *The Journal of the South African Institute of Mining and Metallurgy*, Vol. 107, pp. 427 - 430.

Kaiser P.K. and Kim B-H.(2008): Rock Mechanics Challenges in Underground Construction and Mining, Keynote lecture - SHIRMS 2008, Perth, Australia, In Potvin, Carter, Dyskin & Jeffery (eds.): 1th Sou. Hem. Int. Rock Mech. pp. 23–38, 2008.

Kaiser P.K., Diederichs M.S., Martin C.D., Sharp J., & Steiner W. (2000). Underground works in hard rock tunnelling and mining. *In: Proceedings of the GeoEng2000, Melbourne, Technomic Pub*., 1, 841–926.

Kim B. and Yang H. (2001): Behaviours of Underground Caverns in the Storage of Low Temperature Materials. In: *Frontiers of Rock Mechanics and Sustainable Development in the 21st Century*. Wang S., Bingjun F and Kui Li Z. (eds). pp 417 – 418.

Kirsch G. (1898): Die theorie der elastizitat und die bedürfnisse der festigkeitslehre. Veit. Ver. Deut. Ing., Vol 42, pp. 797–807.

Kitamura K., Masuda K., Takahashi M., and Nishizawa O. (2006): The influence of pore fluids on seismic wave velocities under high temperature and high pressure conditions: Development of a new technique with gas apparatus at AIST, Japan, *Earth Planets Space*, Vol. 58, pp. 1515–1518.

Kjørholt H. (1992): Thermal properties of rock. *Work report 92-56*. Helsinki, Finland: Teollisuuden Voima Oy. 15 p. + 4 appendices. Site investigation.

Klose C.D., Loew S.,Giese R.,Borm G. (2007): Spatial predictions of geological rock mass properties based on in-situ interpretations of multi-dimensional seismic data, *Engineering Geology* Vol. 93 pp. 99–116.

Koca M. Y., Ozden G. Yavuz A. B., Kincal C. Onargan T. and Kucuk K. (2006): Changes in the Engineering Properties of Marble in Fire Exposed Columns. *Int. J. Rock Mech. Min. Sci.* Vol. 43 pp. 520-530.

Kodama N., Fujii Y. and Ishijima Y. (2003): The Effect of Temperature on the Mechanical Properties of Inada Granite and Shirahama Sandstone. *Environmental Rock Engineering*. Saito T and Murata S. (eds). pp. 185.

Kruger A.C. and Shongwe S. (2004): Temperature trends in South Africa: 1960-2003, *Int. J. Climatol.* Vol. 24, pp. 1929-1945.

Kwaśniewski M. and Rodríguez-Oitabén P. (2012): Study on the dilatancy angle of rocks in the pre-failure domain. Harmonising Rock Engineering and the Environment. Qian and Zhou (eds). Tailor & Francis Group, London. pp 681-686.

Li Y. and Xia C (2000); Time- dependent Tests on Intact Rocks in Uniaxial Compression. *Int. J. Rock Mech. and Min. Sci.* Volume 37 pp. 467 -475.

Li Y. Wang J. Jung W. and Ghassemi A. (2012): Mechanical Properties of Intact Rock and Fractures in Welded Tuff from Newberry Volcano. *Proceedings of Thirty-Seventh Workshop on Geothermal Reservoir Engineering Stanford University*, Stanford, California, January 30 - February 1, 2012.

Liu Z. and Jin D. (2014): Experimental Research of Rock Strength and Permeability Characteristics under Different Confining and Hydraulic Pressure. In: *An Interdisciplinary Response to Mine Water Challenges,* China University of Mining and Technology Press, Xuzhou, - Sui, Sun & Wang (eds) pp. 183-186.

Lumb P. (1983): Engineering Properties of Fresh and Decomposed Igneous Rocks from Hong Kong. *Eng. Geol*. Vol. 19, pp. 81 – 94.

Luque A, Ruiz-Agudo E, Cultrone G, Sebastia´n E, Siegesmund S (2011) Direct observation of microcrack development in marble caused by thermal weathering. *Environ Earth Sci* Vol. 62 Issue 7 pp. 1375–1386

Madonia, P. Cusano, P. Diliberto, I.S. Cangemi M. (2013): Thermal anomalies at Vulcano island (Italy) and their relationship with seismic activity, *Phys. Chem. Earth*. Vol. 63, pp. 160–169

Malan D. F. and Basson F. R. P. (1998): Ultra-Deep Mining: The increased Potential for Squeezing Conditions. *The Journal of the Southern African Institute of Mining and Metallurgy*. pp 353-364.

Malan D. F. (2015): Ultra-Deep Mining: The increased Potential for Squeezing Conditions. *The Journal of the Southern African Institute of Mining and Metallurgy*. pp 353-364.

Malan D.F. and Napier J.A.L. (2011): The design of stable pillars in the Bushveld Complex mines: a problem solved? *The Journal of the Southern African Institute of Mining and Metallurgy,* Vol. 111, pp. 821-836.

Mares S. and Tvrdy M. (Editors) (2011): Introduction to Applied Geophysics, *Springer Publisher*, Holland. pp 581.

Martin, C.D., Kaiser, P.K., & McCreath, D.R. (1999). Hoek-Brown parameters for predicting the depth of brittle failure around tunnels. *Canadian Geotechnics Journal 36*, 136-151.

Masri M., Sibai M., Shao J.F., Mainguy M. (2014): Experimental investigation of the effect of temperature on the mechanical behavior of Tournemire shale. *Int. J. Rock Mech. Min. Sci.* Vol. 70, pp. 185–191.

MTS (2001): MTS rock and concrete mechanics testing systems, *MTS Systems Corporation, 14000*. Technology Drive Eden Prairie, MN USA 55344, pp. 265.

Mukhapadhyay S. M. (2003): Sample preparation for microscopic and spectroscopic characterization of solid surfaces and films. In: Mitra S, editor. *Sample preparation techniques in analytical chemistry*. New Jersey: John Wiley & Sons, Inc; p.377–411.

Naldrett A. J., Wilson A. Kinnaird J. and Chunnett G. (2009): PGE Tenor and Metal Ratios within and below the Merensky Reef, Bushveld Complex: Implication of its Genesis. *Journal of Petrology,* Vol. 50 No. 4 pp. 625-659.

Nara Y., Hiroyoshi N., Yoneda T. and Kaneko K. (2010): Effects of relative humidity and temperature on subcritical growth in igneous rock. *Int. J. Rock Mech. Min. Sci.* Vol. 47 pp. 640-646.

Nyungu D. and Stacey T.R. (2014): Time-dependent tensile strengths of Bushveld Complex rocks and implications for rock failure around mining excavations, 6th Southern African Rock Engineering Symposium, Johannesburg.

Okamoto T., Larsen J.O., Matsuura S., Abano S., Takeuchi Y. and Grande L. (2004); Displacement Properties of Landslide Masses at the Initiation of Failure in Quick Clay Deposit and the Effects of Meteorological and hydrological factors. *Eng. Geol. Vol*. 72 pp. 233 – 251.

Okubo S. and Nishimatsu Y. (1985): Uniaxial Testing Using a Linear Combination of Stress and Strain as the Control Variable. *Int. J. Rock Mech. Min. Sci. & Geomech. Abstr*. Vol. 22 No. 5, pp. 323-330.

Ord A. (1991). Deformation of rock: a pressure-sensitive, dilatant material. *Pure Appl Geophys*.137(4), 337–66.

Ortlepp, W.D., O'Ferral, R.C., and Wilson, J.W. (1972): Support methods in tunnels. *Association of Mine Managers of South Africa, Papers and Discussion*, pp. 167–195.

Palchik V. (1999): Influence of porosity and Elastic Modulus on Uniaxial Compressive Strength in Soft Brittle Porous Sandstones. *Rock Mech. Rock Eng*. Vol 32, issue 4 pp 303 – 309.

Palchik V. (2006): Application of Mohr-Coulomb Failure Theory to very Porous Sandy Shale. *Int. J. Rock Mech. and Min. Sci*. Vol. 43 pp. 1153 – 1162.

Paoletti V. (2012): Review article "Remarks on factors influencing shear wave velocities and their role in evaluating susceptibilities to earthquake-triggered slope instability: case study for the Campania area (Italy)", *Nat. Hazards Earth Syst. Sci.*, Vol. 12, pp. 2147–2158.

Payne, T. and Mitra, R. (2008): A review of heat issues in underground metalliferous mines. *Proceedings 12th U.S./ North American Mine Ventilation Symposium* June, Reno Nevada, Wallace, K.G. Jr (ed.), pp. 197–201.

Peng, S.S., and Podnieks, E.R., (1972): Relaxation and the behaviour of failed rock. *Int. J. Rock Mech. Min. Sci.* Pergamon Press Vol. 9, pp. 699–712 paper No. 067

Pérez, K. and Nordlund, E. (2012): Failure process analysis of spalling failure: comparison of laboratory test and numerical modelling data, *Tunnelling and Underground Space Technology*. Vol. 32, pp. 66–77.

Ramana Y.V., Sarma L.P. (1980): Thermal expansion of a few indian granitic rocks. In: *Physics of the Earth and Planetary Interiors* Vol. 22, pp. 36-41.

Rao Q.-h., Wang Z., Xie H.-f., Xie Q. (2007): Experimental study of the mechanical properties of sandstone at high temperature. *Journal of Central South University of Technology*. pp 478-483.

Richter D. and Simmons G. (1974): Thermal Expansion Behaviour of Igneous Rocks. *Int. J. Rock Mech. Min. Sci. and Geomech. Abstr*. Vol. 11, pp. 403-411.

Robertson E. C. (1988): Thermal properties of rocks. *U.S. Geological Survey Open-File Report* 88-441, 106 p.

Röchter L. König D. Schanz T. Niemunis A. Triantafyllidis T. (2011): Shear band systems in plane strain extension: analytical solution and comparison with experimental results, *Granular Matter* vol. 13 pp. 553–563.

Saiang C. and Miskovsky (2011): Effect of Heat on the Mechanical Properties of Selected Rock Types – A Laboratory Study. In: Qian Q. and Zhou Y. (eds) Proc. *12th ISRM International Congress on Rock Mechanics*, Beijing, China. 18 – 21 October.

Schouwstra, R.P., Kinloch, E.D., Lee, C.A. (2000). A short geological review of the Bushveld Complex. *Platinum Metals Review*, 44(1), 33–39.

Scoon R. and Mitchell A. A. (2002): The Merensky Reef at Winnaarshoek, Eastern Bushveld Complex: insights from a wide reef facies. In: Boudreau A (ed) *9th International Platinum Symposium*, Billings, Montana, pp 401–404.

Sellers E.J. (2011): Controlled blasting for enhanced safety in the underground environment. *The Journal of the Southern African Institute of Mining and Metallurgy*, Vol. 111, pp. 11-17.

Setyowiyoto J. and Samsuri A. (2009): Characterization, Pressure, and Temperature Influence On The Compressional and Shear Wave Velocity in Carbonate Rock, *International Journal of Engineering & Technology*, Vol. 9 No. 10, pp. 67-71.

Shao J. F., Chau K. T and Feng X.T (2006): Modeling of Amisotropic Damage and Creep Deformation in Brittle Rocks. *Int. J. Rock. Mech. and Min. Sci*. Vol. 43 pp. 582 -592.

Siegesmund S. Ullemeyer K. Weiss T. Tschegg E. K. (2000): Physical weathering of marbles caused by anisotropic thermal expansion. *International Journal of Earth Sciences*, Vol. 89 pp. 170-182.

Simpson B. (2011): Reliability in geotechnical design – some fundamentals. In: Vogt, Schuppener, Straub & Bräu (eds), *Proceedings of the 3rd International Symposium on Geotechnical Safety and Risk (ISGSR 2011)*, Munich, Germany, pp. 393-399.

Smith, A., Pells, P., (2008): Impact of fire on Tunnels in Hawkesbury Sandstone. *Tunnelling and Underground Space Technol.* Vol. 23, pp. 65–74.

Smith, A., Pells, P., (2009): Discussion of the paper "Impact of fire on Tunnels in Hawkesbury Sandstone" by Smith and Pells [Tunnelling and Underground Space Technology 23 (2008) 65–74] *Tunnelling and Underground Space Technol.* Vol. 24, pp. 112–114.

Soroush H. and Qutob H. (2011): Evaluation of rock properties using ultrasonic pulse technique and correlating static to dynamic elastic constants, *The 2nd South Asain Geoscience Conference and Exhibition, GEOIndia2011*, 12-14th Jan, 2011, Gearter, Noida, New Delhi, India.

Stacey T. R., Van Heerden W. L., Vogler U. W. (1987): Properties of intact rock. *Ground Engineers' Reference Book*. Butterworth and Co., London, pp.21.

Stacey, T.R. (1981): A simple extension strain criterion for fracture of brittle rock. *International Journal Rock Mechanics Mining Science & Geomechanics Abstracts*, 18: 469–474.

Stacey, T.R. and Wesseloo, J. (1998): In situ stresses in mining areas in South Africa. *Journal of the South African Institute of Mining and Metallurgy*, vol. 98. pp. 365–368.

Tandon, R.S., Gupta, V., (2013): The control of mineral constituents and textural characteristics on the petrophysical and mechanical (PM) properties of different rocks of the Himalaya. *Eng. Geol.* Vol. 153, pp 125–143.

Tarasov B.G. (2014): Hitherto unknown shear rupture mechanism as a source of instability in intact hard rocks at highly confined compression *Technophysics*, Vol. 621, pp. 69-84.

Tarasov B.G. and Potvin Y. (2013): Universal criteria for rock brittleness estimation under triaxial compression *Int. J. Rock Mech. Min. Sci*., Vol. 59, pp. 57–69.

Tassell A. (2010): Modern Mining article - Village Main Reef. Available at: http://www.villagemainreef.co.za/news/media-2010/Modern-Mining-June-2010.pdf Accessed on 15th September, 2014.

Tsoutrelis C.E and Exadaktylos G.E (1993): Effect of Rock Discontinuities on Certain Rock Strength and Fracture Energy Parameters under Uniaxial Compression. *Geotechnical and Geological Engineering*, Vol. 11 pp. 81 – 105.

Tsukahara S. Kobayashi R. and Fujiwara T. (2014): *In situ* Microscope Measurements of the Formation of Nanometer-Sized Gold Particles at the Dodecane/Water Interface through the Direct Reduction of Aqueous Tetrachloroaurate (III) by Hydrophobic *dl*-α- Tocopherol in the Presence of 1,10-

Phenanthroline. *Solvent Extraction Research and Development*, Japan, Vol 21 No 2, pp. 119-127.

Vásárhelyi B, and Ván P. (2003): Influence of water content on the strength of rock. *Eng. Geol.* ; Vol.84 pp. 70-74.

Vermeer P.A., de Borst R. (1984). Non-associated plasticity for soils, concrete and rock. *Heron*. 29, (3):1–64.

Vernik L., Bruno M, and Bovberg C. (1993): Empirical Relations between Compressive Strength and Porosity of Siliclastic rocks. *Int. J. Rock. Mech. Min. Sci. Geomech. Abstr*. Vol. 30 pp. 677 – 680.

Voordouw R., Gutzmer J. and Beukes N. J. (2009): Intrusive origin for Upper Group (UG1, UG2) stratiform chromitite seams in the Dwars River area, Bushveld Complex, South Africa, *Mineral Petrol.* Vol. 97 pp.75–94.

Vosteen H. –D. and Schellschmidt R. (2003): Influence of Temperature on Thermal Conductivity, Thermal Capacity and Thermal Diffusivity for Different Types of Rock. *Physics and Chemistry of the Earth*, Vol. 28, pp. 499-509.

Vutukuri V.S. (1974): The effects of liquid on the tensile strength of limestone. *Int. J. Rock Mech. Min. Sci. and Geomech. Abstr.,* Vol. 11, pp. 27-29.

Wai R. S. C. and Tsui K. K. (1983): Near-field Thermo-mechanical Response of a Waste Vault. *Computer and Structures*. Vol. 17, No. 5-6, pp. 677-687.

Watson, B.P. (2010): Rock behaviour of the Bushveld Merensky Reef and the design of crush pillars, *PhD thesis*, School. of Mining Engineering, University of Witwatersrand, Johannesburg, RSA.

Wawersik W. R. and Brace W. F. (1971): Post-Failure Behaviour of a Granite Diabase. *Rock Mechanics* Vol. 2 pp. 61-65.

Wawersik W. R. and Fairhurst C. (1970): A Study of Brittle Rock Fracture in Laboratory Compression Experiments. *Int. J. Rock Mech. Min. Sci.* Vol. 7 No. 5 pp. 561-575.

Wei W., Shouyi X. and Weiya X. (2013): Experimental study and numerical modelling of thermo-mechanical behaviour of Tournemire argillite. *European Journal of Environmental and Civil Engineering*. Vol. 17 pp. 174-186.

Wilson A.H., Jermy C.A., Ridgeway M and Chunnett G. (2005): Rock-Strength and Physical Properties of Norites of the Merensky and Bastard units, Western Bushveld Complex. *South African Journal of Geology*. Vol. 108 pp. 525 -540.

Wiseman, N. (1979): Factors affecting the design and condition of mine tunnels. Research Report No. 45/79. Chamber of Mines of South Africa, Pretoria, South Africa, p. 22.

Wong T and Brace W. F. (1979): Thermal Expansion of Rocks: Some Measurement at High Pressure. *Tectonophysics*, Vol. 57, pp. 95-117.

York, G., Canbulat, I., Kabeya, K.K., Le Bron, K.B., Watson, B.P. and Williams, S.B. (1998): Develop guidelines for the design of pillar systems for shallow and intermediate depth, tabular, hard rock mines and provide a methodology for assessing hangingwall stability and support requirements for the panels between pillars, *SIMRAC GAP 334 final report.* CSIR. Division of Miningtek, Johannesburg. RSA.

Young, R.P., Hill, T.T., Bryan, I.R., and Middleton, R. (1985): Seismic spectroscopy in trauure characterization. *Quarterly Journal of Engineering Geology*, Vol. 18. pp. 459–479.

Yuan S.-C. and Harrison J. P. (2004): An empirical index for the dilatant deformation of rock. *Int. J. Rock Mech. Min. Sci.*, Vol. 41, pp. 679–686.

Zhao X.G. and Cai M. (2010a): A mobilized dilation angle model for rocks. *Int. J. Rock. Mech. Min. Sci.* Vol. 47 pp. 368 – 384.

Zhao X.G. and Cai M. (2010b): Influence of plastic shear strain and confinement-dependent rock dilation on rock failure and displacement near an excavation boundary. *Int. J. Rock. Mech. Min. Sci.* Vol. 47 pp. 723 – 738.

Zhao X.G., Cai M.F., Cai M.(2010):Considerations of rock dilation on modeling failure and deformation of hard rocks—a case study of the mine-by test tunnel in Canada, *Journal of Rock Mechanics and Geotechnical Engineering*, Vol. 2 , pp. 338–349.